

DEVELOPMENT AND OPTIMIZATION OF OPEN-SOURCE PUMPS
AND DROP-BASED SPLIT-AND-MERGE
MICROFLUIDIC DEVICES

by

Humberto Scott Sanchez

A dissertation submitted in partial fulfillment
of the requirements for the degree

of

Doctor of Philosophy

in

Chemical Engineering

MONTANA STATE UNIVERSITY
Bozeman, Montana

July 2023

©COPYRIGHT

by

Humberto Scott Sanchez

2023

All Rights Reserved

DEDICATION

I dedicate this dissertation to my parents, Teri Lee Sanchez and Humberto Sanchez, without your love I would never have made it this far.

I would also like to dedicate this dissertation to all my family and friends who lent their hearts in support of my triumphs and tribulations during this journey.

Finally, this dissertation is dedicated to all those in academia struggling with their mental health, it is a dynamic process that can get better with the proper input and control.

ACKNOWLEDGEMENTS

I would like to acknowledge my advisor Dr. Connie Chang for her support and guidance throughout my thesis. I am would not be here without the help and support of my past and present lab mates as well. Thank you, Drs. Joshua Heinemann and Andrew Lingley for helping with all matters related to microfabrication. I would like to thank all members of my committee, Drs. Stephanie McCalla, Stephan Warnat, and Ross Carlson for you support. The Montana Microfabrication Facility allowed us to create reliable and level microfluidic devices with photolithography.

This work was all made possible by funding provided by the Montana State University Norm Asbjornson College of Engineering, the Defense Advanced Research Projects Agency, the National Science Foundation, and the National Institutes of Health.

TABLE OF CONTENTS

1. INTRODUCTION	1
Background.....	1
Funding and Collaborations.....	2
Dissertation Overview	2
2. LITERATURE REVIEW	5
Literature Review Overview.....	5
Driving Fluid Flow in Microfluidic devices	5
Syringe Pumps	6
Hydrostatic Pumps	7
Pneumatic Pressure Pumps	8
Conclusion	10
Microfluidic Drops.....	10
Microfluidic Drop Production.....	11
T-Junction Geometry	11
Flow-Focusing Geometry	13
Conclusion	14
Microfluidic Device Modelling	15
Governing Equations	15
Dimensionless Numbers	17
Hydraulic Circuit Analogy.....	18
Drop Resistance	19
Conclusion	20
Splitting Microfluidic Drops.....	21
T-Junctions.....	21
λ -Junctions	22
Conclusion	23
Merging Microfluidic Drops.....	24
Electro-Coalescence.....	24
Conclusion	25
3. OPEN-SOURCE PNEUMATIC PRESSURE PUMP FOR DROPLET-BASED MICROFLUIDIC FLOW CONTROL	26
Manuscript Contributions of Authors	26
Manuscript Information Page	27
Abstract.....	28
Introduction.....	28

TABLE OF CONTENTS CONTINUED

Method	31
Pneumatic Design of the Pressure Pump	31
Pneumatic Interface between the Pressure Pump and a Microfluidic Device	33
Electrical Design of the Pressure Pump.....	35
Control Scheme of the Pressure Pump.....	35
Guided User Interface of the Pressure Pump	36
Pressure Regulation Variables	37
Validation with Microfluidic Drop Production.....	37
Results.....	39
Pressure Regulation Without Flow	39
Pressure Regulation During Microfluidic Drop Production	40
Drop Production.....	41
Discussion.....	42
Conclusion	47
Acknowledgements.....	48
Conflict of Interest	48
Data Availability Statement.....	48
Funding Statement	49
 4. MASS CONSERVATION OF DROPLET-BASED MICROFLUIDIC SPLITTING AND MERGING (SAM) DEVICES.....	 50
Manuscript Contributions of Authors	50
Manuscript Information Page	51
Abstract.....	52
Introduction.....	52
Methods and Materials.....	54
Device Design.....	54
Device Fabrication	57
Salt Electrode Operation.....	58
Two-Phase Drop Composition.....	58
Video Capture and Analysis	58
Fluid Delivery	59
Input Drop Production	59
Modelling and Analysis Pipeline	60
Modelling.....	61
Device Modelling.....	61
Drop Modelling.....	64
Results.....	66
Drop Merging Optimization	66

TABLE OF CONTENTS CONTINUED

Drop Splitting.....	75
Drop Merging.....	79
Drop Splitting and Merging	82
Empirical Drop Models of SAM Devices.....	84
Conclusion	86
5. CONCLUSIONS AND OUTLOOK.....	88
Conclusions.....	88
Outlook	89
APPENDICES	92
APPENDIX: Microfluidic Gut-on-a-chip.....	93
Motivation.....	94
Laminar Flow Patterning of a Hydrogel Scaffold.....	96
Method	96
Simulations	97
Results.....	99
Conclusions.....	101
Utilizing a Pinned Hydrogel Scaffold.....	102
Method	102
Optimizing the Collagen Formulation	103
Cell Barrier Formation.....	105
Future Directions	107
REFERENCES CITED.....	108

LIST OF TABLES

Table	Page
1. List of Variables Used During Device Modelling	15
2. Comparison of components across published pressure pumps.....	43
3. Comparison of pressure regulation variables across published pressure pumps	45
4. List of Variables.....	54
5. Channel widths and heights of interest for the three SAM devices presented	57
6. Input drop lengths used in the three SAM devices	60
7. Modelled flow rates and split ratios for the three SAM devices.....	64
8. Flow rates needed to achieve optimal merging for each geometry and drop size	74
9. Q_{inlet} and range of Q_{oil} and Q_{aqueos} flow rates used in splitting and merging experiments	78
10. Values for the constant in equation (18).....	81
11. Values for the constant in equation (20).....	84

LIST OF FIGURES

Figure	Page
1. Overview of syringe pumps used to drive fluid flow in microfluidic devices.....	6
2. An example of a hydrostatic pressure pump.....	7
3. A representative schematic of a pneumatic pressure pump.....	9
4. A representative image of a microfluidic drop.....	10
5. A still image of a T-junction producing drops.....	12
6. Images of drop production at a microfluidic flow-focusing junction.....	13
9. An overview of the T-junction geometry used to split drops.....	22
10. An overview of the λ -junction geometry.....	23
11. An example of electro-coalescence to merge drop pairs.....	25
13. Diagram of mechanical and electrical components of the pneumatic pressure pump.....	32
14. Images of different components of the pneumatic pressure pump.....	34
15. GUI used to control the pneumatic pressure pump.....	36
16. Response of the pneumatic pressure pump to step changes in set point without (A, B, and C) and with outlet flow (D, E, and F).....	39
17. Microfluidic drop production using the pneumatic pressure pump.....	41
18. A drawing of a representative SAM device illustrating the layout of the devices of this work.....	56

LIST OF FIGURES CONTINUED

Figure	Page
19. Images of the split junction for the three SAM devices tested in this study	57
20. The network diagram for SAM devices.....	62
21. A representation of the split junction and the merge junction illustrating the two drop processes in a SAM chip	64
22. Image sequences demonstrating different merging regimes.....	68
23. Merging regimes depicted by the distribution of drop areas before, outlined in blue, after, in yellow, merging.....	71
24. The relationship between drop splitting ratio and flow rate splitting ratio	76
25. Drop area increases scale linearly with the aqueous and oil flow rates at the merging junction	80
26. Percent change of drops entering the SAM devices and leaving the merge junction scales linearly with the aqueous and oil flow rates at the merging junction	83
31. The proposed microfluidic gut-immune-system (μ GIS) chip.....	95
32. COMSOL Multiphysics simulations show which flowrates can be used to create patterned collagen paths with different widths	98
33. A 4 mg ml ⁻¹ collagen barrier serves as an adequate diffusional barrier for the μ GIS chip	100
34. A 2 mg ml ⁻¹ collagen barrier serves as an adequate diffusional barrier for the μ GIS chip	100

LIST OF FIGURES CONTINUED

Figure	Page
35. Represent images of epithelial cells live, dead, and DAPI stained in the μ GIS device.....	101
36. Collagen concentration and crosslinking pH affect the ability of dendritic cells (DCs) to cross the collagen barrier	104
37. Caco2 barrier permeability increased after 7 days and appears to remain constant after 15 days	105

ABSTRACT

Drop-based microfluidics is used to encapsulate small volumes of chemical and biological agents into discrete drops. The contents of these pico-liter sized drops can then be used for biochemical assays. Microfluidic devices are used to manipulate these drops through the removal and addition of drop contents and pumps are used to control the fluid flow within the microfluidic devices. Often, the pumps used to drive fluid flow are prohibitively costly and the fluid dynamics of the devices used to control drop contents are not fully described. This research focuses on de-mystifying both the pump systems and microfluidic devices commonly used in drop-based microfluidics. We focused on developing an open-source pneumatic pressure pump to create microfluidic drops. Pneumatic pressure pumps have been found to be flexible and accurate systems to control fluid flow within microfluidic devices. Our pump system was found to be accurate and fast-responding as well as easy to assemble and control via open-source software. In addition, we developed a design process to develop drop-based split-and-merge (SAM) microfluidic devices. These devices have been commonly used to control drop volumes and add reagents for intra-drop assays. Our design and optimization methodology was then used to develop multiple SAM geometries with various splitting capabilities and the ability to create a broad range of drop volumes. The operating conditions for each SAM device was optimized for different input drop volumes. We also developed an empirical drop model to predict drop volume changes within a SAM device. Our open-source pneumatic pressure pump is a fast responding and accurate system that can be adapted for driving flow in any microfluidic device. Our drop-based SAM devices and the development and modelling process we developed serves as a blueprint for future SAM devices and similar drop manipulation microfluidic devices.

CHAPTER ONE

INTRODUCTION

Background

The research presented in this thesis contributes to expanding lab-on-chip technologies. The thesis is focused on the development of an open-source pneumatic pressure pump for driving flow in microfluidic devices and the modelling and design of drop split-and-merge microfluidic devices. Microfluidics translates biological and chemical assays from the lab bench to devices that are only several centimeters in size. More specifically, drop-based microfluidics encapsulates samples into isolated picoliter-sized environments. Part of this thesis is focused on the development of an open-source pneumatic pressure pump to drive flow in microfluidic devices that is both customizable and cost-effective. An open-source pump allows the users to change out components to suit their needs, is controlled with an accessible and open-source microcontroller, and has a user interface programmed in an open-source programming language. A cost-effective pneumatic pressure pump limits the use of commercial components and is constructed with reliable and off-the-shelf components. However, an open-source pressure still needs to be accurate and have rapid response times to control drop-based microfluidic devices reliably. One such microfluidic device that needs to be controlled reliably is a drop split-and-merge device.

Drop split and merge devices enable in-drop assays, as encapsulated targets often need to be combined with other reagents. When the assay targets are encapsulated into drops there can be the need to combine those targets with other reagents. Split-and-merge devices are used to split

the incoming drops into two drops and merge one of those drops with a new aqueous stream that contains assay reagents. The splitting of the drops is controlled by the geometry of the devices, as well as the flow rates used in the device, and the merging of the drops with a new aqueous stream is controlled by the flowrates used to operate the device. These devices have been used in several in-drop biological assays, yet their modelling and operation has yet to be described in detail. Therefore, it is important to model these devices and develop linear scaling equations to predict drop size changes.

Funding and Collaborations

This work was supported by the Defense Sciences Office, DARPA grant W911NF-17-2-0034, 356 National Institutes of Health (NIH) 1R21A1151923, and National Science Foundation (NSF) 357 CAREER DMR-1753352. I gratefully acknowledge support from National Institutes of Health (NIH) 3U01EB029242-02S2. Device fabrication was conducted at the Montana Microfabrication Facility (MMF) at Montana State University (MSU) (Montana, USA).

Dissertation Overview

The remainder of this thesis is organized into three chapters; Chapter 2 is comprised of a literature review detailing various aspects of microfluidics and drop-based microfluidics. First, there is an overview of the various pump systems used to drive fluid flow in microfluidics. Microfluidic drops are introduced, as well as how they are produced in microfluidic devices. Then, modelling microfluidic fluid flow with the electric circuit analogy is covered. Finally, there are two sections covering various techniques to split drops in microfluidic devices and merge drops in microfluidic devices.

Chapter 3 describes the design, construction, and characterization of an open-source pneumatic pressure pump. A description of the pneumatic design, electrical design, the control scheme and the guided user interface is included. The pump's ability to regulate pressure was tested without flow and during drop-making were tested and quantified with respect to the overshoot, rise times, settling times, and accuracy. The pump was also validated with its ability to produce monodisperse drops in a microfluidic device whose normalized drop length were proportional to the applied pressures according a scaling law. The pumps performance and cost were compared to previously published open-source pumps and found to be an improvement on the path toward open-source pneumatic pressure pumps. The journal article is titled "*Open-source pneumatic pressure pump for drop-based microfluidic flow control*" and was accepted by the peer-reviewed journal Engineering Research Express.

Chapter 4 describes the design, modelling, and subsequent scaling laws found for drop split-and-merge (SAM) microfluidic devices. SAM devices were designed with a similar layout and modelled with the electric circuit analogy. Three different SAM device geometries were then fabricated with different splitting capabilities. These SAM devices were tested using three different drop sizes. Drop merging was optimized for each geometry and drop size. After optimizing drop merging, two empirical equations were found that relate the flowrates used to operate the device and the drop volume changes. These empirical models are similar in form to a derived equation from a mass balance of drops in SAM devices. This work will impact future in-drop assays that utilize SAM devices and make it possible for nonexperts to create their own SAM devices. The journal article is titled "*Mass conservation of drop-based microfluidic splitting and merging (SAM) devices*" and is being prepared for submission to the peer-reviewed journal Physical Review Fluids.

The appendix contains additional work completed during this PhD to develop a microfluidic gut-on-a-chip. The motivation of this work is discussed in context of the parent grant from the NIH. Two different hydrogel scaffold techniques are discussed, a flow patterned gel and a pinned gel. Finally, the potential future directions of this work is discussed.

CHAPTER TWO

LITERATURE REVIEW

Literature Review Overview

Drop-based microfluidics is a technology where small volumes of biological and biochemical reagents can be encapsulated in discrete drop volumes. These drops are individual components in an emulsion that are created and processed within microfluidic devices. Manipulating liquids in microfluidic devices relies on an understanding the pump systems used to drive fluid flow on the microfluidic devices as well as the physics of fluid flow inside the microfluidic channels. Therefore, this literature review will discuss pump systems commonly used with microfluidic devices, review the physical and chemical components on drops, and how they are produced in microfluidic devices. Since microfluidic devices are used to both create and process drops, this literature review will discuss devices used to produce, split, and merge drops along with a useful framework to model fluid flow in microfluidic devices.

Driving Fluid Flow in Microfluidic Devices

In this section I will be discussing the various methods of driving fluid flow in microfluidic devices. I have chosen to focus on the following pumps and their strengths and weaknesses; syringe pumps, hydrostatic pumps, and pneumatic pumps. These systems were chosen as they are often used in literature and directly comparable to the pump system described in Chapter 3 of this thesis. I will not be reviewing peristaltic pumps due to their pulsatile flow profiles.

Syringe Pumps

Syringe pumps are the most popular system for driving liquid flow in microfluidic devices. Syringe pumps are often used because of their simplistic design and ease of use (Fig. 1) [1]. Utilizing a syringe pump only requires loading a liquid-filled syringe into a motorized stage that then pushes the syringe plunger at a rate equal to the desired volumetric flow rate (Fig. 1(A)). The stage pushes the syringe plunger by turning a lead screw with an electrical motor that then transfers the rotary motion of the motor into linear motion (Fig. 1(B)).

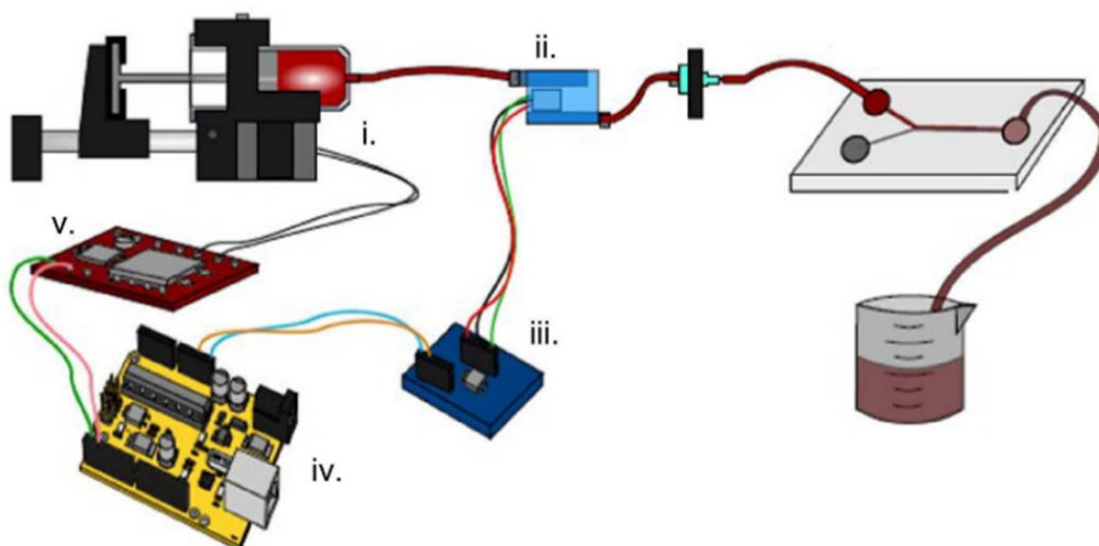


Figure 1. Overview of syringe pumps used to drive fluid flow in microfluidic devices. An illustration of the components used to operate a syringe pump, the stepper motor and microcontroller. Adapted from Lake *et. al.* [2] (CC BY 4.0).

Despite their ubiquitous use in microfluidics, syringe pumps can introduce flow rate fluctuations during operation. If syringe pumps are used to drive fluid flow within elastic microfluidic channels, mechanical oscillations in the electrical motor can lead to flow rate oscillations in the channels [3]. These oscillations are more pronounced at low frequencies, i.e. low flow rates, which can effect on-chip processes like microfluidic drop production [4].

However, these flow rate fluctuations can be dampened with a control mechanism that measures the pressure downstream of the syringe and alters the plunger velocity [2] or using an active flow stabilizer that alters the fluid viscosity with temperature changes [5]. However, these modifications to syringes require levels of expertise that may be uncommon in microfluidics laboratory groups.

Hydrostatic Pumps

Another method for driving fluid flow in microfluidic devices is the hydrostatic pressure pump. Unlike syringe pumps, hydrostatic pumps do not have any active components to drive fluid flow and instead relies on gravity. Hydrostatic pressure pumps rely on the simple principle that an elevated reservoir of liquid will flow into a lower microfluidic channel (Fig. 2) and the fluid velocity in the channel is dependent on the height of the reservoir and the dimensions of the microfluidic channels. These pump systems are ideal for spaces where electronic pumps cannot be placed and are also simple to setup and use and have been found to have less flow rate fluctuations when compared to syringe pumps [6].

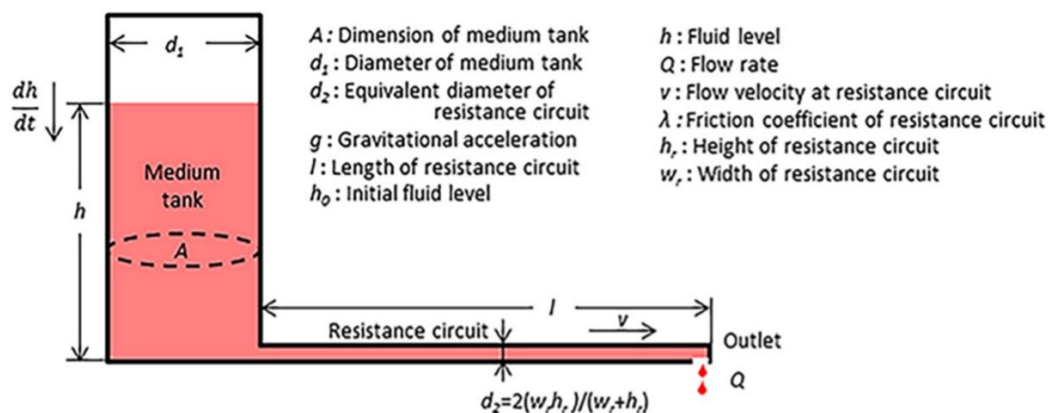


Figure 1. An example of a hydrostatic pressure pump. Adapted from Komeya *et. al.* [7] (CC BY 4.0) (<http://creativecommons.org/licenses/by/4.0/>).

However, hydrostatic pressure pumps are cannot be used for some applications. For example, hydrostatic pumps are not useful for when high-pressures are required as the height of the elevated reservoir is proportional to the inlet pressure of the microfluidic channel [8]. Also, the flow generated using a hydrostatic pressure pump is inherently transient during long term usage [7, 8]. Over the course of several days, the liquid level in the elevated reservoir will decrease as the liquid perfuses into the microfluidic device, this in turn decreases the pressure differential and the flow rate within the microfluidic device. There has been some work to passively fill the elevated reservoir during long term operations [8], however hydrostatic pumps are still inadequate for high-pressure applications.

Pneumatic Pressure Pumps

Finally, I will discuss pneumatic pressure pumps. Pneumatic pumps operate by pressurizing the head space of a fluid reservoir and pushing the liquid, through a down tube, onto a microfluidic device [9]. These pump systems can be thought of as a hybrid between syringe pumps and hydrostatic pumps. Like syringe pumps they use an active control mechanism, a pressure regulator. However, unlike syringe pumps, pneumatic pumps need a pressure sensor to control the pressure of the reservoir whereas syringe pumps often lack a sensor to control the electrical motor. Pneumatic pumps are like hydrostatic pumps in that the users sets the pressure of the fluid input instead of specifying the flow rate, as is done with syringe pumps.

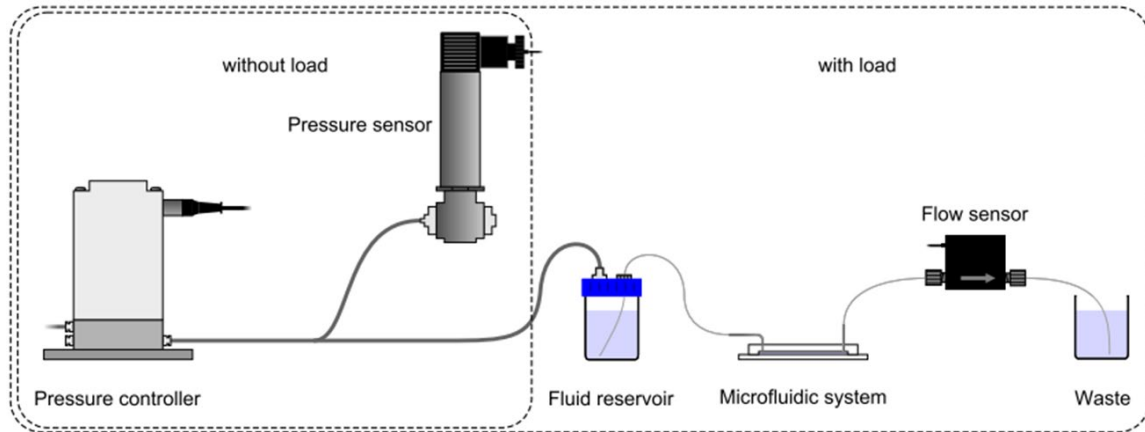


Figure 3. A representative schematic of a pneumatic pressure pump. Adapted from Frank *et. al.* [9] (CC BY 4.0).

Pneumatic pressure pumps have several disadvantages and advantages when compared to syringe pumps and hydrostatic pumps. The advantages will be discussed in detail in Chapter 3 of this thesis so I will mention the disadvantages here. First, pneumatic pumps require a pressurized gas source to function, such as a motorized compressor or a compressed gas tank, that increases their footprint and complexity. Also, commercial pneumatic pumps are more expensive compared to commercial syringe pumps, which is why there is a desire to design open-source pneumatic pressure pumps [10, 11]. Finally, using a pneumatic pressure to achieve specific flow rates, or shear rates, in a microfluidic device requires more in-depth knowledge of fluid dynamics. As I will discuss later in this literature, the flow rate in a microfluidic channel is proportional to the pressure drop in that channel and that channel's hydraulic resistance. Since pneumatic pumps control the upstream pressure in a microfluidic device, the flow rates inside the channels need to be calculated from the device's channel geometries and dimensions.

Conclusion

For this this section of the literature review, I have introduced three different pump systems commonly used to drive fluid flow in microfluidic devices. Syringe pumps, which use an electrical motor to push a syringe plunger and the syringe contents onto a microfluidic device. Hydrostatic pressure pumps, which use gravity to flow liquid onto a microfluidic device from an elevated reservoir. Finally, pneumatic pressure pumps which pressurize a fluid reservoir to force that fluid onto a microfluidic device. In the past, syringe and hydrostatic pumps have been popular options due to their low-cost compared to commercial pneumatic pressure pumps. Later in this work, a low-cost pneumatic pressure pump is presented to allow users access to these pump systems.

Microfluidic Drops

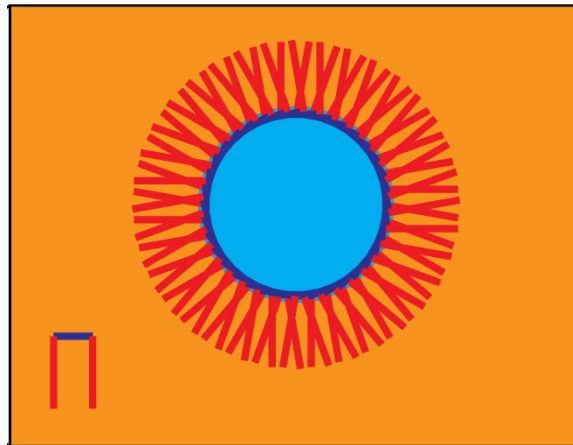


Figure 4. A representative image of a microfluidic drop. A single water drop is shown dispersed in an immiscible oil with a layer of surfactant molecules between the two phases.

In later sections of this literature review and thesis I will discuss microfluidic drops. This section of the literature is dedicated to discussing what these drops are and their applications in biochemistry. Microfluidic drops are an emulsion, a mix of two immiscible liquids, with a dispersed water phase and a continuous oil phase. The aqueous drops are stabilized against coalescence with a surfactant, an amphiphilic polymer that reduces the surface tension between the two immiscible phases (Fig. 4). Surfactants contain a water-soluble head group and an oil-soluble tail group and form an interface between the drop contents and the bulk oil [12, 13]. The aqueous drops are spherical with diameters ranging from 25 μm to 100 μm depending on the application. The aqueous contents can contain biological and biochemical agents ranging from cells, enzymes, viruses, polynucleotides, and the contents associated buffer or medium [14-18]. The continuous oil phase we use in the work presented in this thesis is a fluorocarbon. Fluorocarbons are used as biological agents have low solubility in them and gases have high solubility [12].

Microfluidic Drop Production

We have reviewed several methods to control fluid flow within a microfluidic and the composition of microfluidic drops. In this next section we will discuss several methods of producing drops in a microfluidic device; T-Junctions and Flow-Focusing.

T-Junction Geometry

The first microfluidic geometry I will review is also the first microfluidic geometry to form water-in-oil drops, the T-Junction [19]. In a T-Junction, two rectangular channels intersect at a right angle with the continuous oil phase flowing in the main channel and the dispersed

water phase entering from the smaller secondary channel (Fig. 5(A-B)). As the two immiscible fluids intersect, the dispersed phase forms drops of a specific length in the main channel (Fig. 5(B-C)). The length of these drops, therefore their volume, is dependent on the dimensions of the T-Junctions, the widths of the main and secondary channel, and the flow rates of the water and oil phase, Q_{water} and Q_{oil} respectively. This relationship is shown in equation (1) where the drop length, L , normalized to the width of the channel containing the drop, w , is equal to the linear scaling law in the right-hand side of equation (1). The constant, α , is determined empirically as its value depends on the geometry of the T-junction [20, 21].

$$\frac{L}{w} = 1 + \alpha \left(\frac{Q_{water}}{Q_{oil}} \right) \quad (1)$$

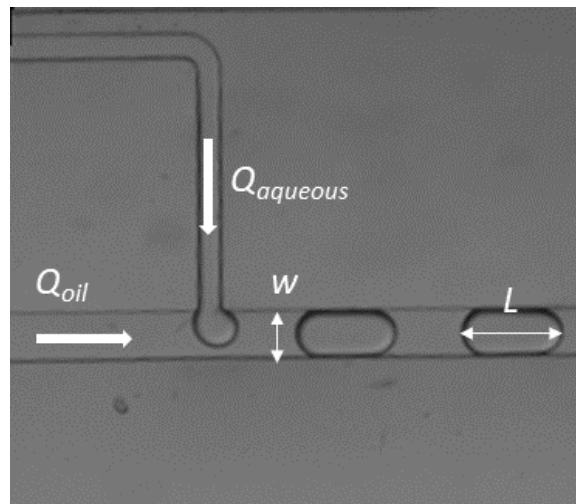


Figure 5. A still image of a T-junction producing drops. The channel width, w , drop length, L , and phase flow rates are shown, $Q_{aqueous}$ and Q_{oil} .

T-Junctions have several advantages and disadvantages when producing drops. First, T-Junctions are simple to design since they only require three channels to function, the aqueous inlet, the oil inlet, and the outlet channel. Also, the drop breakup mechanism and resulting drop

size has been studied extensively and equation (1) has been found to hold true for most values of $Q_{aqueous}$ and Q_{oil} . However, T-Junctions have some limitations. First, T-Junctions have a minimum drop size they can produce, drops whose length is equal to the width of the main channel. This is due to the breakup mechanism, drops need to fill the entire width of the main channel before they break off from the incoming aqueous stream [20]. Secondly, T-Junctions have a limited range of flow rates and Capillary numbers where they produce monodisperse drops. As the water-phase is increased, the drops produced at a T-Junction become more varied and polydisperse [22]. This means that T-Junctions are not ideal for high-speed flow rates and can only produce a limited range of drop sizes.

Flow-Focusing Geometry

The next microfluidic geometry I will review is the flow-focusing geometry [23]. In a flow-focusing junction, the continuous phase is separated into channels and intersects with the dispersed phase from two sides (Fig. 6(A)). The dispersed phase inlet forms a right angle with the two continuous inlets and enters the junction where there is a constriction point followed by an expansion in the outlet channel (Fig. 6(A)). The dispersed phase forms drops at this constriction as the continuous phase forces drop breakup (Fig. 6(B)) [24].

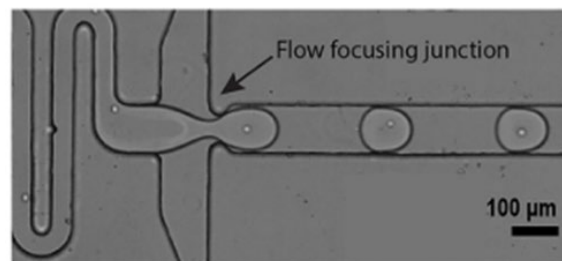


Figure 6. Images of drop production at a microfluidic flow-focusing junction. Adapted from Loveday *et. al.* [25] (CC BY 4.0).

The flow-focusing junction geometry has some advantages and disadvantages when compared to the T-junction. The first advantage is that there is a much lower limit to the drop size that can be produced at a flow-focusing junction, drops can be produced that are smaller than the channel width or the constriction point [23, 26]. Also, unlike the T-junction, the flow-focusing junction can produce much more monodisperse drops at higher flow rates making them suitable for high-throughput applications [22]. However, unlike T-junctions, there is no agreed upon scaling law for drop size at flow-focusing junction [21, 27] and predicting drop size requires phenomenological models [28]. This is due to the large varieties of geometries that can be used in a flow-focusing junction, like constriction size and shape. There are also two main regimes that flow-focusing junctions operate at to produce drops; dripping and jetting [29]. The dripping regime produces larger and more uniform drops that breakup near the constriction whereas the jetting regime produces smaller and less uniform drops that breakup further away from the dispersed phase inlet [30]. The regime present during drop production is dependent on the flow rates and viscosities of the phases [30].

Conclusion

In this section I reviewed the two main microfluidic geometries to produce drops. The T-junction was the first geometry to be studied and has the simplest design. The T-junction is useful to produce drops whose size can easily predicted, however it can only operate at low flow rates and has a lower limit to the drop size when compared to the flow-focusing junction. The flow-focusing junction has a much more varied design and can produce drops at higher flow rates when compared to the T-junction.

Microfluidic Device Modelling

In this section of the literature review, I will be reviewing the main method to model the fluid flow in a microfluidic device; the electric circuit analogy. I will not be reviewing the use of computational fluid dynamics to model fluid flow in microfluidic devices as this technique has limitations concerning multi-phase fluid flow and was not used in this thesis. The electric circuit analogy has been adequate to predict drop motion in microfluidic devices [31-37] and therefore is commonly used in lieu of CFD methods. Variable symbols and definitions for this section of the literature review are listed in Table 1.

Table 1. List of Variables Used During Device Modelling

Variable	Unit	Description
ρ	kg m ⁻³	Fluid density
\mathbf{u}	m s ⁻¹	Fluid Velocity Vector
u	m s ⁻¹	Fluid Velocity
U	m s ⁻¹	Characteristic velocity
t	s	Time
p	Pa	Pressure
μ	Pa s	Fluid Viscosity
r, x	m	Distance
R	m	Outer Radius
Q	m ³ s ⁻¹	Volumetric Flow Rate
Δp	Pa	Pressure Drop
L	m	Channel length
σ	N m ⁻¹	Surface Tension
D_H	m	Hydraulic Diameter
h	m	Channel Height
w	m	Channel Width
R_H	Pa s ³ m ⁻¹	Hydraulic Resistance

Governing Equations

Fluid flow in microfluidic devices can be approximated as incompressible fluids whose velocity fields can be described with the Navier-Stokes equation (Eq. 2), where the rate of

momentum change is equal to the sum of the convective forces, pressure forces, and viscous forces. The Navier-Stokes equation and the conservation of mass (Eq. 3) can be used to solve for the velocity fields of all fluids assuming constant densities and viscosities. Luckily, the Navier-Stokes can be simplified for microfluidic flow velocity profiles. Fluid flow in a microfluidic channel can be assumed to be laminar, steady state, unidirectional, and does not accelerate. This simplifies the Navier-Stokes equation to the linear Stokes equation for fluid flow (Eq. 4). Equations (3) and (4) can be then used to solve for the velocity of a cylindrical channel as a function of the radial distance from the center of the channel and the pressure gradient in the x -direction giving equation (5).

$$\rho \frac{d\mathbf{u}}{dt} = -\rho\mathbf{u}\nabla\mathbf{u} - \nabla p + \mu\nabla^2\mathbf{u} \quad (2)$$

$$\nabla \cdot \mathbf{u} = 0 \quad (3)$$

$$\nabla p = \mu\nabla^2\mathbf{u} \quad (4)$$

$$u = \frac{R^2 - r^2}{4\mu} \left(-\frac{dp}{dx} \right) \quad (5)$$

$$Q = \frac{\pi R^4}{8\mu} \frac{\Delta p}{L} \quad (6)$$

Since we are often concerned with the volumetric flow rate in a channel, not the velocity shape in that channel, equation (5) needs to be integrated for all points in the r -direction. This integration gives the Hagen-Poiseuille equation for the volumetric flow rate of a long pipe as a function of the pipe's radius and pressure drop (Eq. 6). Equation (6) will hold true for laminar flow in a pipe that is much longer than it is wide.

Dimensionless Numbers

Before we continue with equation (6) to get the final form of the electric circuit analogy, we will review some dimensionless numbers we did not describe in previous sections. The dimensionless numbers used in fluid dynamics are ratios of different forces and are used to determine which force is dominant in a scenario which is then used to determine which equations are useful or which fluid regime is present [27, 29, 38].

In the previous section I mentioned the Capillary number when describing which microfluidic geometry can be used to make drops. The Capillary number (Ca) is a ratio of the viscous forces versus the interfacial tension (Eq. 7). When the phase composition is held constant, higher values of Ca indicate that the characteristic velocity, U , of the dispersed fluid flow is increased. Ca determines the shape of drops in microfluidic channels [39] and is less than one in the work described in this thesis.

$$Ca = \mu U / \sigma \quad (7)$$

$$Re = \rho U D_H / \mu \quad (8)$$

I also mentioned laminar flow in the previous sub-section when deriving the Hagen-Poiseuille equation. Only fluid flow in the laminar regime can be modelled via the Stokes equation (Eq. 4). Reynolds number (Re) is used to determine if a fluid flow scenario is laminar and is the ratio of inertial forces and the viscous forces (Eq. 8). The value of Re ranges from 0.1 to 10 in the work described in this thesis. This value of Re indicates that the Hagen-Poiseuille equation can adequately describe fluid flow in microfluidic channels.

Hydraulic Circuit Analogy

The Hagen-Poiseuille equation provides a relationship between the flow rate within a channel and the pressure drop in that channel. This relationship (Eq. 6) can be further simplified and rearranged in terms of the hydraulic resistance, R_H , of a microfluidic channel (Eq. 8). The value of R_H is defined in equation (9) for a cylindrical pipe. For a rectangular channel, such as those used in all the microfluidic devices described in this thesis, the value of R_H is defined with equation (10), which is acquired by solving the Stokes equation (Eq. 4) for a rectangular channel whose width is larger than its height. Equations (8) and (10) can now be used to describe the laws that describe the electric circuit analogy.

$$\Delta p = QR_H \quad (8)$$

$$R_H = \frac{8\mu L}{\pi R^4} \quad (9)$$

$$R_H = \frac{12\mu L}{wh^3} \left[1 - \frac{192h}{\pi^5 w} \sum_{n=1,3,5}^{\infty} \frac{1}{n^5} \tanh\left(\frac{n\pi w}{2h}\right) \right]^{-1} \quad (10)$$

The electric circuit analogy only has a few rules to follow for microfluidic devices. The first two deal with the channels in a microfluidic device being analogous to electrical resistors. First, if channels are arranged in series, one after another, then the equivalent resistance of those channels in series is equivalent to the sum of the channel resistances (Eq. 11). This rule is useful for two channels in series that have two different widths or heights, as those channels can be grouped together in terms of resistance. Another rule deals with channels in parallel, or when resistors branch out and then connect again. For channels in parallel, the inverse equivalent resistance is equal to the sum of the sum of the inverse of the individual channel resistances (Eq.

12). The final two rules of the electric circuit analogy concern the conservation of mass and energy. First, if two or more channels intersect, there is no accumulation of mass at the intersection, so the sum of the flow rates equal zero (Eq. 13). Finally, if microfluidic channels form a close loop, meaning they start at one point and end at the same point, then the sum of the pressure drops in those channels also equal zero (Eq. 14). Note that if two branches terminate in a device outlet, then they form a closed loop as they both terminate at atmospheric pressure.

$$R_{H,eq} = \sum_{i=1}^N R_{H,i} \quad (11)$$

$$\frac{1}{R_{H,eq}} = \sum_{i=1}^N \frac{1}{R_{H,i}} \quad (12)$$

$$\sum_{n=1}^N Q_n = 0 \quad (13)$$

$$\sum_{n=1}^N \Delta p_n = 0 \quad (14)$$

Drop Resistance. The electric circuit analogy can be used to predict the fluid flow in microfluidic devices when there is only fluid phase in the channels. However, if there are drops in the channels, that also fill the entire width of the channel, then these drops increase the pressure drop in the channels with added resistance. These drops that fill the channel width, slugs, create gutters in rectangular channels that decrease the cross-sectional area of the channel that the continuous phase can travel in. These gutters sometimes cause slug drops to travel at a different velocity than the continuous phase [40]. The drop bodies and drop caps contribute to the pressure drop in a channel (Eq. 15) [40]. Each term in equation (15) has been written in terms of known variables and semiempirical coefficients (Eq. 16) [40]. The semiempirical coefficients,

B_1 , B_2 , and B_3 , depend on the channel aspect ratio and the continuous phase and surfactant used and need to be determined empirically [40]. The added resistance of drops in microfluidic channels can affect the predicted flows in those channels [31, 32].

$$\Delta p_{channel} = \Delta p_{no-drops} + \Delta p_{drop-body} + \Delta p_{drop-caps} \quad (15)$$

$$\Delta p_{channel} = \frac{B_1 U_{drop} \mu}{h^2} \left[A_0 (L_{channel} - L_{drop-body}) + B_2 L_{drop-body} + B_3 n h (\mu U_{drop} / \sigma)^{-1/3} \right] \quad (16)$$

Conclusion

In this section of the literature I reviewed using the electric circuit analogy to model fluid flow in microfluidic devices. First, the Navier-Stokes equation and the conservation of mass equation can be simplified, due to the laminar flow nature of fluid flow in microfluidic devices, to give the Stokes equation. The Stokes equation can then model the velocity profile of liquid in a long circular pipe giving the Hagen-Poiseuille equation. The Hagen-Poiseuille equation applies to pipes whose radii are much smaller than their length, like channels in microfluidic devices. The Hagen-Poiseuille equation can be re-arranged to give a simple relationship between the volumetric flow rate in a pipe and the pressure drop in a pipe and its hydraulic resistance. This same solution can be performed for a rectangular channel. The pressure drop of a microfluidic channel being proportional to the flow rate of the channel and its hydraulic resistance forms the basis of the electric circuit analogy and is followed by several other rules. Finally, I discussed the contribution of slug drops to a channel's resistance.

Splitting Microfluidic Drops

This next section of the literature is concerned with splitting drops in microfluidic devices. Splitting drops is performed to control drop size during production [41], after adding reagents to drops [42], or before adding reagents to drops [43, 44]. I will briefly discuss two channel geometries used to split incoming drops into two different channels. I will use the term “mother” drop for the incoming drop and “daughter” drops to describe the drops being produced after the splitting junction.

T-Junctions

Just as T-junctions were the first geometry described to produce drops, T-junctions were the first to be described to split drops [45]. The T-junction geometry consists of a straight channel flowing toward two outlet channels that form a right angle with the inlet channel (Fig. 9). As the mother drop collides with the dead-end wall it elongates and then forms two daughter drops (Fig. 9). The T-junction geometry can be used to form symmetric and asymmetric daughter drops depending on the resistance of the outlet channels [45, 46]. There are three different breakup regimes present in T-junctions; no breakup, breakup with tunnels, and breakup with permanent obstructions. The regime that the mother drop will experience depends on the Capillary number of the mother drop and the length of the mother drop [47]. Shorter mother drops with low Capillary numbers will not break in a T-junction since the geometry requires the drop to elongate to the point of instability before breaking [45, 47, 48]. If shorter mother drops are sped up, thereby increasing their Capillary number, then they breakup with tunnels, or gaps between the daughter drops and the channel walls [47]. At the regime of breakup with tunnels, the shear stresses elongating the mother drop are the main cause of breakup [47]. Finally, drop

breakup with permanent obstruction occurs with longer mother drops with higher Capillary numbers, i.e. velocities [48]. This regime occurs when the daughter drops fill the widths of the outlet channels and the thin fluid bridge connecting the two daughter drops eventually breaks [47]. The dependence of the mother drop velocity, i.e. Capillary number, and mother drop length are the one of the disadvantages to using T-junctions in microfluidic devices.

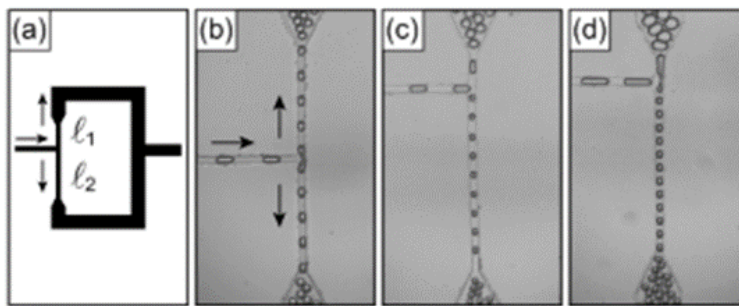


Figure 9. An overview of the T-junction geometry used to split drops. Adapted from Link *et. al.* [45] with permission from the American Physical Society.

λ -Junctions

Another channel geometry, the λ -junction can be used to split drops in microfluidic devices [49]. The λ -junction was first studied to determine if drop breakup can occur at lower Capillary numbers than the T-junction [49]. In a λ -junction, the mother drop travels along a main channel with a secondary channel that intersects with the main channel (Fig. 10(A-B)). When the two channels intersect, a portion of the mother drop enters the secondary channel and one of three breakup regimes occur; direct breakup (Fig. 10(B)), no breakup, or indirect breakup [49]. No breakup occurs only when the daughter drop does not extend into the secondary far enough and fast enough. Indirect breakup occurs when the daughter drop penetrates below a critical length, but is going fast enough the breakup. Direct breakup occurs when the daughter drop penetrates the secondary channel far enough, regardless of its velocity [49]. The authors who

initially studied the λ -junction found that degree of breakup in a λ -junction could be predicted based on the geometry of the channels and was not dependent on the mother drops velocity or length [49]. The breakup mechanism at a λ -junction is similar to the T-junction geometry used to produce drops [50]. As the daughter drop enters the secondary channel, the continuous phase is blocked and if the shear stress of the continuous phase overcomes the surface tension of the drop then the drop breaks. The only disadvantage of using a λ -junction, is that they have not been studied as extensively as T-junctions. Otherwise, λ -junctions being able to operate at lower Capillary numbers compared to T-junctions is advantageous as there is a wider range of drop velocities available for splitting.

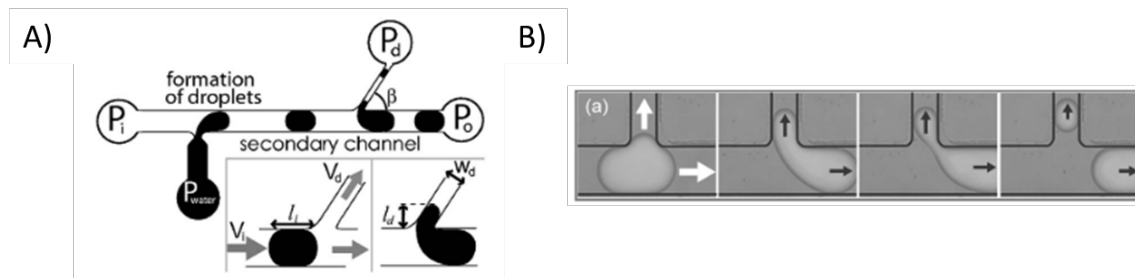


Figure 10. An overview of the λ -junction geometry. A) A schematic of the λ -junction showing the main and secondary channel. B) An example of complete drop breakup at a λ -junction. Adapted from Menetrier-Deremble and Tabeling [49] with permission from the American Physical Society.

Conclusion

In this section, I discussed two main geometries used to split incoming drops into two different channels. The T-junction relies on shear stress to elongate the mother drop and split it into the daughter drops. The λ -junction relies on the daughter drop entering a secondary channel far enough that the shear stress of the continuous phase overcomes the surface tension of the drop. The breakup regimes of the T-junction was found to be dependent on the mother drop

velocity and length while the breakup regimes in the λ -junction was found to be dependent on the geometry of the device. The λ -junction geometry was used in Chapter 4 of this thesis to split drops since drop splitting volumes can be predicted from the geometry of the device.

Merging Microfluidic Drops

In this section, I will be discussing merging drops with another aqueous stream, or another drop. Merging drops is performed in microfluidic devices to add reagents to existing drops [42-44, 51, 52]. This discussion will be limited to using an electrical field to merge drops and will not cover chemical coalescence.

Electro-Coalescence

I mentioned before that a surfactant is used to prevent drop coalescence. An electrical field can be used to destabilize the water-oil interface and cause drop coalescence [53, 54] and is the basis for merging drops in a microfluidic device. An electrical field can be created on a microfluidic device by inserting metal electrodes [55] or filling channels with a polar liquid [56] and connecting the conductors to an function generator (Fig. 11(A)). The electrical field generated by on-chip electrodes can be used to merge drops [55, 57] or merge drops with another aqueous stream that is perpendicular to the channel containing the drops [58] (Fig. 11(B)). When two drops are merged, it is common that one of the drops is significantly larger than the other drop to allow the drops to synchronize their locations before merging [43, 55, 57]. Additional device features such as rail-road channels and anchors are needed to merge individual drops of the same size [59, 60]. However, these additional features require more complex microfabrication techniques which lower device production throughput.

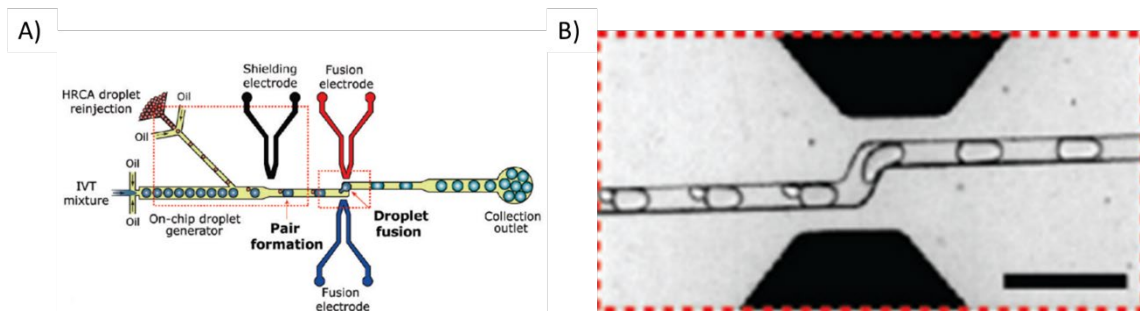


Figure 11. An example of electro-coalescence to merge incoming drops with an additional aqueous stream. A) A device layout used to merge two incoming drops with a field generated by on-chip electrodes. B) An image of two drops being merged at the site of the electrical field. Adapted with permission from Mazutis *et. al.* [57]. Copyright 2009 American Chemical Society.

Conclusion

In this subsection I briefly discussed the method to merge drops with other drops or another aqueous stream in a microfluidic device with an electrical field. This technique relies on the electrical field destabilizing the water/oil interface and allows for the addition of reagents into the drops. Electro-coalescence has been used to merge individual drops or merge drops with an additional aqueous stream. Electro-coalescence is used in Chapter 4 of this thesis to also merge drops with an additional aqueous stream. However, the devices used in Chapter 4 also generate drops during the merging process enabling the generation of drops of various sizes at the merging junction.

CHAPTER THREE

OPEN-SOURCE PNEUMATIC PRESSURE PUMP
FOR DROP-BASED MICROFLUIDIC
FLOW CONTROL

Contribution of Authors and Co-Authors

Manuscript in Chapter 3

Author: Humberto S. Sanchez

Contributions: H.S.S. designed research, performed research, analyzed data, and wrote the manuscript

Co-Author: Connie B. Chang

Contributions: C.B.C designed research and wrote the manuscript

Manuscript Information

Humberto S. Sanchez and Connie B. Chang

Engineering Research Express

Status of Manuscript:

Prepared for submission to a peer-reviewed journal

Officially submitted to a peer-reviewed journal

Accepted by a peer-reviewed journal

Published in a peer-reviewed journal

Issue 3

10.1088/2631-8695/ace299

Abstract

An open-source pneumatic pressure pump is engineered for driving fluid flow in a microfluidic device. It is designed to be a cost-effective and customizable alternative to commercial systems. The pneumatic pressure pump utilizes a single open-source microcontroller to control four dual-valve pressure regulators. The control scheme is written in the Arduino development environment and the user interface is written in Python. The pump was used to pressurize water and a fluorinated oil that have similar viscosities. The pump can accurately control pressures to a resolution of less than 0.02 psig with rapid response times of less than one second, overshoot of desired pressures by less than 30%, and settling response times of less than two seconds. The pump was also validated in its ability to produce water-in-oil drops using a drop-making microfluidic device. The resultant drop size scaled as expected with the pressures applied to the emulsion phases. The pump is the first custom-made dual-valve regulator that is used to precisely control fluid flow in a microfluidic device. The presented design is an advancement towards making more fully open-source pneumatic pressure pumps for controlling flow in microfluidic devices.

Introduction

Microfluidics can translate biological and chemical assays from the lab bench to a device that is only several square centimeters in size [61]. These devices, commonly called microfluidic chips, are useful tools in many fields of biotechnology, particularly for single cell analyses [62]. Fluids are typically delivered into micron-sized channels on the chip from milliliter-sized vessels using mechanical syringe pumps [2], hydrostatic pressure pumps [8, 63, 64], or pneumatic pressure

pumps [9-11, 65]. Syringe pumps operate by converting the rotary actuation of a stepper motor into linear motion that drives the displacement of a syringe plunger [2]. Hydrostatic pressure pumps flow fluid from an elevated reservoir into the microfluidic channels, in which the pressure applied to the fluid is proportional to the height of the reservoir relative to the device [6]. Pneumatic pressure pumps utilize a pressure regulator to control the pressure of a compressed gas that drives fluid from a reservoir into the device [4, 66].

Pneumatic pressure pumps have several advantages over syringe and hydrostatic pumps. Syringe pumps have larger flow-rate fluctuations and slower response times to setpoint changes when compared to pressure pumps [4, 6]. Hydrostatic pumps have a narrower range of usable pressures and cannot be used for high-pressure applications as easily as pneumatic pumps [8]. Pneumatic pumps can also be used with a wider range of vessel volumes compared to syringe pumps.

Given the benefits of pneumatic pressure pumps for microfluidic research, engineering open-source versions of commercial pumps can be advantageous from a cost perspective, as commercial pumps can cost tens of thousands of dollars. An ideal open-source pump would consist of an open-source microcontroller and a customizable pressure regulator. The control scheme and its variables would be adjustable and uploaded to the microcontroller. The pump would be controlled using a guided user interface (GUI) written in an accessible programming language, such as Python [67]. Finally, the pump system would ideally not require custom machining or assembly.

Prior work creating open-source pneumatic pressure pumps utilized a blend of commercial and open-source components. Pressure pumps consist of four main components: the pressure

regulator, the pressure transducer or sensor, the controller, and the GUI. Frank *et al.* used commercially available parts for all of these components, except for the interface [9]. Gao *et al.* developed a pump that used a commercial pressure regulator; the other components were open-source with a GUI written in C++ [11]. Finally, Watson and Senyo created a fully open-source pump with custom pressure regulators and a GUI written in C++. However, the pump created by Watson and Senyo was used to control valves on a microfluidic chip, not to drive flow [10].

In this work, we present a fully open-source pneumatic pressure pump designed to drive flow on a microfluidic device. Our pump utilizes a single open-source controller to control four dual-valve pressure regulators. The control scheme was written in the Arduino development environment and the GUI was written in Python. The ability of the pump to accurately change and regulate pressure was evaluated with step changes in pressure both without flow and when driving flow in a drop-making microfluidic device. The fluids used in these experiments were water and a fluorinated oil which have similar viscosities. When driving flow, the pump overshot the target pressures by less than 30%, settled within 5% of the desired pressure in less than two seconds, and was accurate down to less than 1% of the target pressure. The performance of the pump was comparable to previously reported open-source pneumatic pumps and other pumps. The pump performance was also validated in its ability to produce water-in-oil drops using a drop-making microfluidic device. The resultant drop size, measured by normalized drop length, scaled as expected to the applied pressures. This work demonstrates the utility of this custom built open-source pneumatic pressure pump for rapidly creating drops with stable fluid flow.

Method

Pneumatic Design of the Pressure Pump

This pneumatic pressure pump utilizes a dual proportional solenoid design (Figures 1 and 2). A compressed air tank is used as a positive pressure source for the pump design. A tank mounted regulator valve RV1 (McMaster-Carr, 7897A59) is used to set the pressure to ≈ 14 psig. A push-to-connect fitting (McMaster-Carr, 51235K107) is coupled to the downstream side of RV1 with a brass fitting (McMaster-Carr, 4429K111). Nylon tubing (McMaster-Carr, 5548K84) connects RV1 to an additional regulator valve, RV2, (McMaster-Carr, 9892K11) via an additional push-to-connect fitting. RV2 gives a more precise measurement of the pressure upstream of the pump. RV2 uses a barbed connector (McMaster-Carr, 5463K438) to couple 0.125-inch inner diameter silicone tubing (McMaster-Carr, 51845K53) to the remaining downstream connections. The silicone tubing is connected to a 25 mm 0.2- μm filter (Fisher Scientific, GVS ABLUO™) with a luer taper to barb fitting (McMaster-Carr, 51525K273) to prevent particulates from entering the pump. The filter outlet connects to all the inlet solenoids S_I with more 0.125-inch silicone tubing and three wye connectors (McMaster-Carr, 53415K143). After these wye connectors, the tubing enters the enclosure that houses the solenoid valves. The solenoids use compression fittings upstream and downstream of the valve, Figure 2(C). Nylon tubing (McMaster-Carr, 5548K81) is coupled to the 0.125-inch silicone tubing with a reducing adapter (McMaster-Carr, 5463K48). The S_I is coupled to the S_O with a wye connector, Figure 2(C), (McMaster-Carr, 53415K143). The S_O uses the nylon and silicone tubing to vent outside of the enclosure. The pressure transducer (PT) (Honeywell, HSCDANN005PGAA5) couples downstream of the wye connector with a tee connector (McMaster-Carr, 5116K183), Figure

2(C). The PT is connected to the upward facing barb and the downstream side of the tee is connected to a luer taper to barb fitting (McMaster-Carr, 51525K273) that exits the enclosure, Figure 2(C).

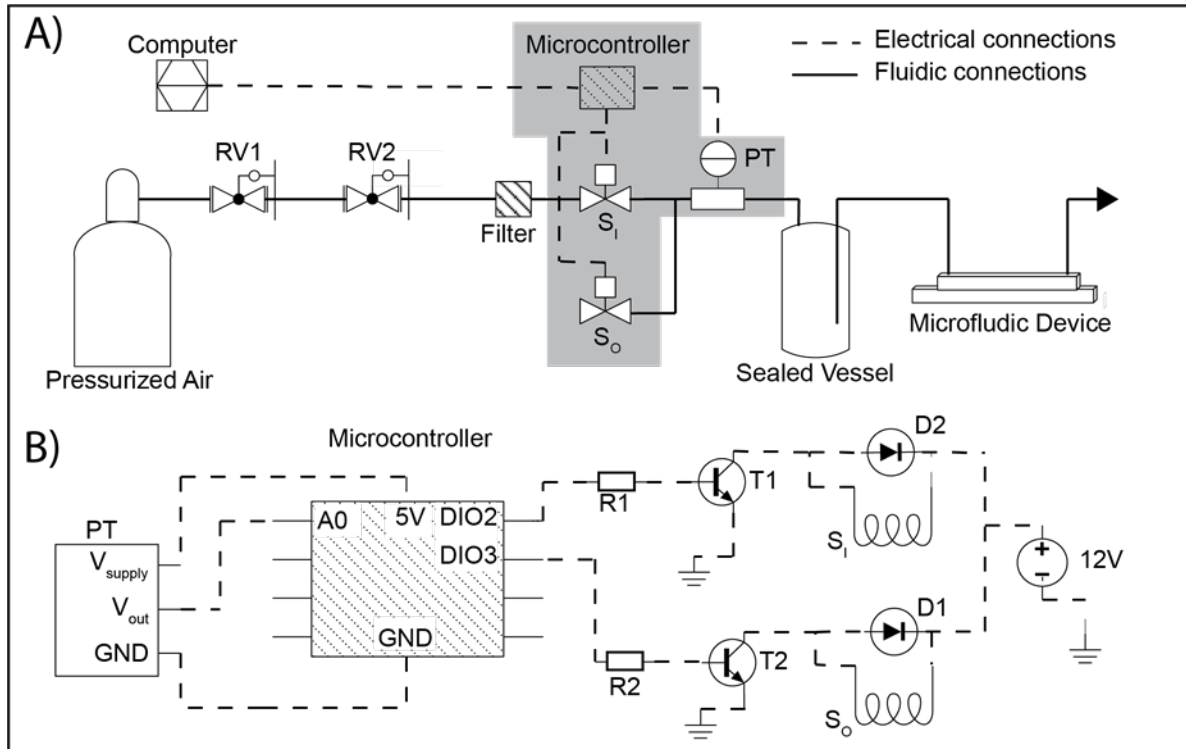


Figure 1. Diagram of mechanical and electrical components of the pneumatic pressure pump. A) Mechanical component diagram of a dual-valve regulator. A compressed air tank supplies a high-pressure source which is adjusted using two regulator valves, RV1 and RV2. Two proportional solenoid valves, S_I and S_O, regulate the pressure of a sealed vessel. One valve regulates air flow between a compressed air tank and the vessel, S_I, and another regulates air flow from the vessel to atmospheric pressure, S_O. The microcontroller controls each solenoid valve while monitoring the sealed vessels with a pressure transducer, PT. Liquid from the sealed vessel can then flow through a microfluidic device. Dashed and solid lines represent electrical and fluidic (gas or liquid) connections, respectively. B) Circuit diagram, expansion of the grey region in A). The PT sends an analog value proportional to the pressure to the pin A0. Pins DIO2 and DIO3 send PWM signals to the transistors T1 and T2 via base resistors R1 and R2. The PWM signals turn the solenoid valves, S_I and S_O, on and off. The diodes, D1 and D2, protect the transistors during operation. Dashed lines represent electrical connections.

Pneumatic Interface between the Pressure Pump and a Microfluidic Device

The pump can be used to pressurize fluid in a sealed vessel (Figure 1(A)). As a proof of concept, a 25 mL media bottle (PyrexTM, 139525) with an open cap (Corning, 1395-25HTSC) and a silicone septum (Corning, 1395-25SS) is used as the vessel, Figure 2(B). The septum is pre-punctured with a 20-gauge needle (BD, 305176) in two locations for the pressurized inlet and the liquid outlet. The pressurized inlet is coupled to the pump with polyethylene tubing (Scientific Commodities, BB31695-PE/5) where one end is connected to a 20-gauge dispensing needle (McMaster-Carr, 75165A677), which is attached to the luer taper of the pump, Figure 2(B). The other end of the polyethylene tubing is connected to an angled 20-gauge dispensing needle (McMaster-Carr, 75165A688) with the yellow hub removed and the shaft inserted into the polyethylene tubing. The liquid outlet uses a 6-inch-long stainless-steel dispensing needle (McMaster-Carr, 6710A85) with a quick-turn to barb adapter (McMaster-Carr, 51525K141), Figure 2(B). The barb adapter is coupled to a short length of 0.79 mm inner diameter medical grade silicone tubing (Scientific Commodities Inc., BB519-13) followed by more polyethylene (Scientific Commodities Inc., BB31695-PE/2) tubing, Figure 2(B). The polyethylene tubing is then coupled to another angled 20-gauge dispensing needle with the hub component removed. The end of the angled dispensing needle can then be inserted into the punched inlet of a PDMS microfluidic device.

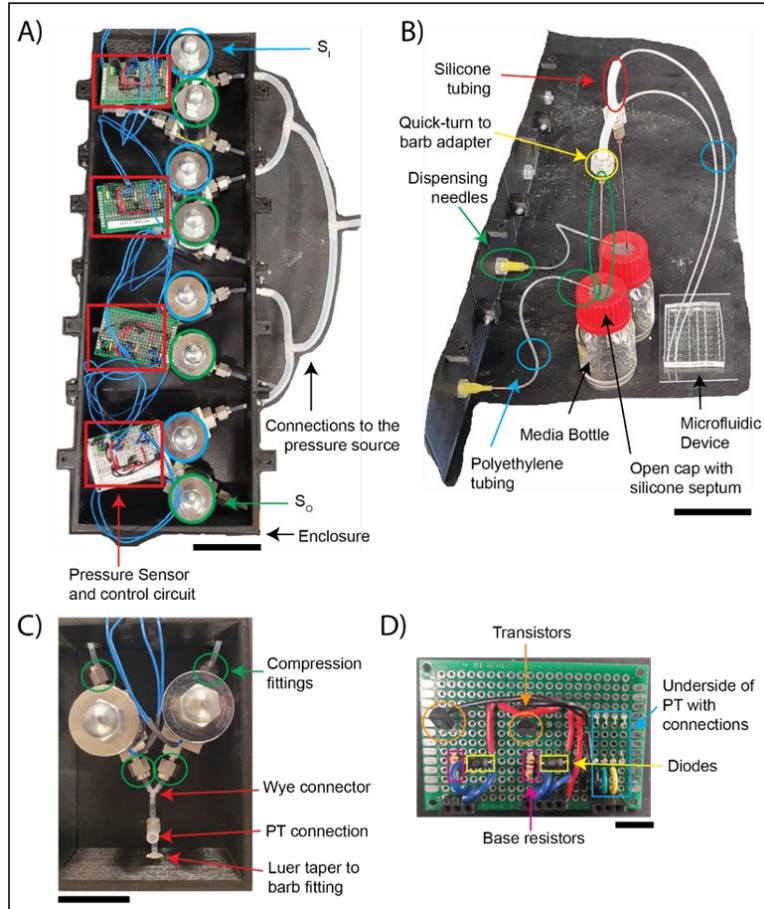


Figure 2. Images of different components of the pneumatic pressure pump. A) A top-down view of the pneumatic pressure pump in the enclosure with the upper portion removed. The pressure sensors and control circuits (red), inlet solenoids (blue), outlet solenoids (green), the enclosure, and the tubing between the pump and the pressure source are highlighted. Scale bar = 5 cm. B) A representative image of the connections between the pump, sealed vessels, and the microfluidic device. The various dispensing needles used to connect components are circled in green. The polyethylene tubing that connects the pump to the sealed vessel and the sealed vessel to the device are circled in blue. The quick-turn barb adapter and short length of silicone tubing that connect the sealed vessel to the microfluidic device are circled in yellow and red respectively. The media bottle, open cap with a silicone septum, and a microfluidic device are also indicated. Scale bar = 5 cm. C) A representative image of the pneumatic connections inside the enclosure. The compression fittings of the inlets and outlets of the solenoid valves are circled in green. The wye connector that couples the solenoids, the connection for the pressure transducer, PT, and the luer taper to barb fitting that exits the enclosure are indicated with red arrows. The scale bar is 3 cm. D) A representative image of the control circuit soldered onto the perboard. The Transistors (orange), base resistors (magenta), the underside of the PT (blue), and the diodes (yellow) are outlined. Scale bar = 1 cm.

Electrical Design of the Pressure Pump

All four dual-valve pressure regulators are controlled from a single microcontroller using transistor switches. The circuit diagram used for all the pressure regulators is shown in Figure 1(B). The PT transmits the measured pressure downstream of the solenoids to the microcontroller (Arduino, Mega 2560 Rev 3) via an analog signal. The microcontroller supplies the PT with 5 V and the PT transmits a voltage signal between 0 and 5 V which is proportional to a pressure between 0 and 15 psig. Alternative pressure sensors with varying ranges can be used in this setup depending upon the application. The microcontroller opens and closes the solenoids valves (Aalborg, PSV1S-BB) using pulse width modulation (PWM) enabled digital pins. The PWM pins send a power cycle (PC) that opens or closes the valves. The PC is sent to NPN transistors (ON Semiconductor, 2N4124) via base resistors (Digikey, 13-CFR-25JR-52-1KTR-ND, $1\text{ k}\Omega \pm 5\%$), Figure 2(D). The transistors act as digital switches to power the solenoids with a 12V power supply (Mean Well, LRS-100-12). Diodes (ON Semiconductor, 1N4005G) are wired in parallel to the solenoids to provide the current stored in the inductive load a path to ground without shorting the transistor when the circuit is opened [68], Figure 2(C). The electrical circuit was assembled and soldered onto a perfboard, Figure 2(D).

Control Scheme of the Pressure Pump

The feedback loop for the pressure regulators uses proportional control over the solenoid valves power cycles. If the measured point is lower than the set point, the inlet solenoid PC is increased by 0.004% and the outlet solenoid PC is decreased by the same amount. Conversely, if the measured point is higher than the set point, the inlet solenoid PC is decreased by 0.004% and the outlet solenoid PC is increased by the same amount. The increment and decrement values are

the lowest gain available for the microcontroller based on the PWM resolution limit. This feedback loop operates continuously with a delay time of 1 ms between each iteration. The control scheme and serial communication software for the Arduino microcontroller is available on GitHub (<https://github.com/thechangelab>).

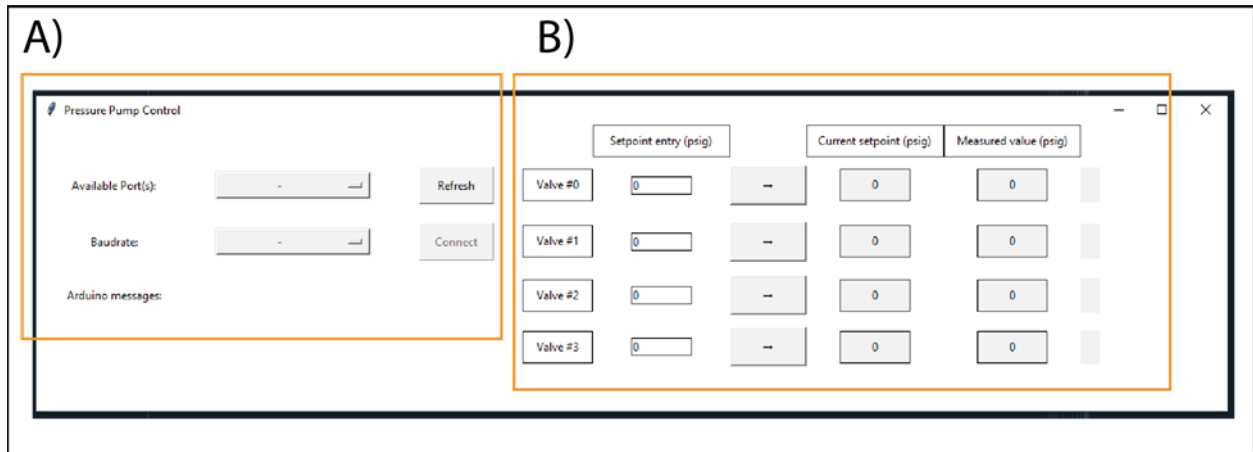


Figure 3. GUI used to control the pneumatic pressure pump. A) This section detects peripherals connected to computer, selects the baud rate for serial communication, and connects to the microcontroller. B) This section allows the user to change the set points of the four regulators, displays the measured points, and confirms that the change has been accepted by the microcontroller. The window size is 1250 by 300 pixels.

Guided User Interface of the Pressure Pump

The pump interface is written in Python and allows users to control the system via a local computer and is shown in Figure 2. The GUI was written in Python using the Tkinter and PySerial libraries [67]. The GUI is broken down into two main sections, one for establishing serial communication (Figure 3(A)) and one for controlling the pressure regulators (Figure 3(B)). Serial communication is established after selecting the serial port to which the pump is connected and selecting the baud rate that is used in the microcontroller. The *Refresh* button is used to detect all used serial ports. The *Connect/Disconnect* button establishes serial communication and the “*Arduino is ready to start*” message is displayed if the correct parameters are selected. The

set points of the individual regulators are changed after entering a new value in the “*Set point entry*” column and then pressing the arrow button to the right of that column. The new set point is displayed in the “*Current set point*” column and the indicator to the far right of the GUI changes to green if that change has been accepted by the microcontroller. The current measured point is also displayed for each regulator. The GUI software is also available on GitHub (<https://github.com/thechangelab>).

Pressure Regulation Variables

The performance of the pressure pump was evaluated by applying changes in the set point and recording the measured pressures, or measured points. The pump performance was initially tested in the sealed vessel without liquid flow. The ability of the pump to regulate pressure is based off of four values: the overshoot (OS), the rise time (t_R), the settling time (t_S), and the accuracy [69]. The OS is determined graphically and is the percentage of how much the measured point goes over or under the new set point. Values of t_R and t_S are also determined graphically and are values of how much time is required for the measured point to reach the new set point and how long it takes for the measured point to be within 5% of the new set point. Accuracy is the average difference between the measured point and set point for all data points between the t_R and the time of another set point change.

Validation with Microfluidic Drop Production

The pump performance was validated during microfluidic drop production. Drops are formed in a microfluidic device that uses a flow-focusing geometry to produce an emulsion comprised of an immiscible dispersed phase in a continuous phases stabilized by a surfactant [23]. The dispersed phase consisted of deionized water and the continuous phase consisted of 3% (w/w)

ammonium carboxylate perfluoropolyether surfactant [70] dissolved in fluorinated oil HFE-7500 (3M). The drop-maker had a channel height of 40 μm with an exit channel width of 100 μm and was fabricated using soft lithography [71]. The channels were rendered fluorophilic with an injection of a solution of (tridecafluoro-1,1,2,2-tetrahydrooctyl) trichlorosilane (1 v/v%) in HFE-7500 (3M).

Pump performance can be assessed from its ability to form drops of different lengths proportional to the applied pressures. The major axis length of a drop in a microfluidic device (ℓ_d) can be normalized to the width of the microfluidic channel (w_{ch}) to give a dimensionless drop size. Ward *et al.* has shown that this drop size is proportional to the squared ratio of dispersed and continuous phases pressures, P_D and P_C respectively, multiplied by a scalar value [72]. This relationship is shown in equation (1), where α is the scalar multiplier that can be determined using linear regression.

$$\frac{\ell_d}{w_{ch}} = \alpha \left(\frac{P_D}{P_C} \right)^2 \quad (1)$$

Drop sizes were determined during drop production using brightfield microscopy. During the drop production process, the microfluidic device was mounted on an inverted microscope (Nikon, TE2000, 10X objective lens). Footage of the drop-making process was captured using a high-speed camera (Edgertronic, SC2) at 5,000 frames per second. The footage was analyzed using drop morphometry and velocimetry (DMV) software [73]. The DMV software is specifically designed to analyze drops in microfluidic devices and allows the user to determine the time-history of drop lengths, widths, areas, positions, velocities, and pixel intensities.

Pump performance was also evaluated with step changes during microfluidic drop production. The OS , t_R , t_S , and accuracy were determined during step changes to the pressures applied to the continuous phase, P_C .

Results

Pressure Regulation without Flow

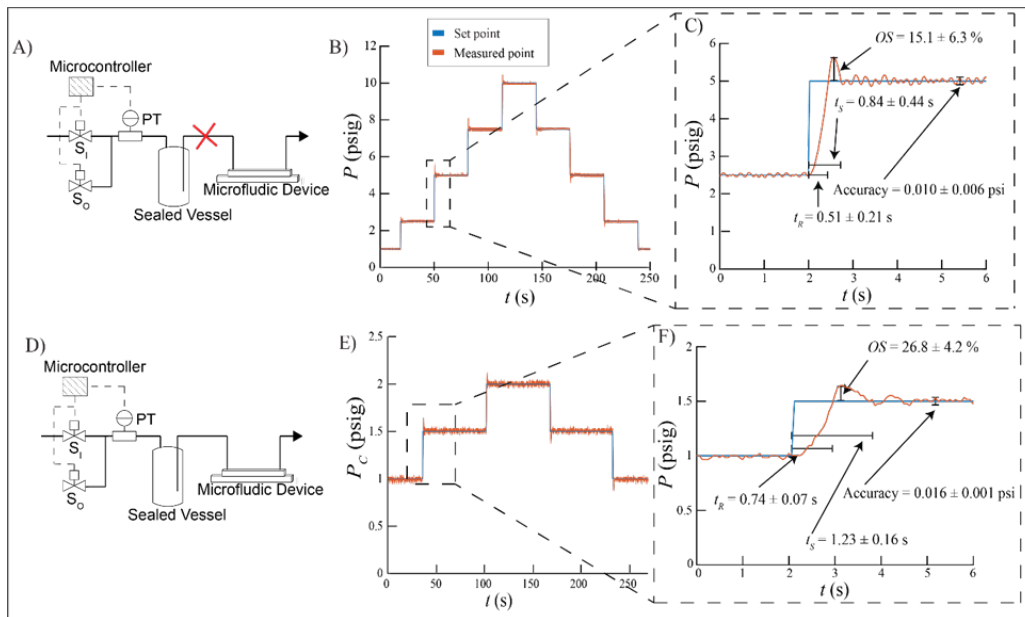


Figure 4. Response of the pneumatic pressure pump to step changes in set point without (A, B, and C) and with outlet flow (D, E, and F). A) The pump schematic without outlet flow. B) The set points (blue) and measured points (orange) of one pressure regulator in response to step changes. C) A detailed zoom of the boxed region in B) with the average rise time t_R , settling time t_S , overshoot OS , and accuracy shown. D) The pump schematic connected to a microfluidic device. E) The set points (blue) and measured points (orange) of the pressure regulator in response to step changes in the continuous phase pressure, P_C , during microfluidic drop-making. The dispersed phase pressure, P_D , was held constant at 1.0 psig. F) A detailed zoom of the boxed region in E) with the average rise time t_R , settling time t_S , overshoot OS , and accuracy shown.

The ability of the pump to change the pressure of the sealed vessel without outlet flow was evaluated (Figure 4(A)). The pressure was both increased and decreased from 1 to 10 psig

with step changes ranging from 1.5 to 2.5 psig. These step changes were performed three times during three different operational cycles, in which the entire system was turned off between replicates. Figure 4(B) displays one of these replicates. The set point is increased and decreased from 2.5 psig to 5.0 psig. A detailed zoom of one of the step changes is displayed in Figure 4(C) which also displays average t_R , t_S , OS , and accuracy values across all step changes and all replicates. The average OS for all the step changes was $15.1 \pm 6.3\%$, the average t_R was 0.51 ± 0.21 seconds, the average t_S was 0.84 ± 0.44 seconds, and the average accuracy was 0.010 ± 0.006 psi or 0.1% of the full span of pressures.

Pressure Regulation During Microfluidic Drop Production

The ability of the pump to change the pressure of a vessel during microfluidic drop production was evaluated (Figure 4(D)). One pressure regulator varied P_D from 1.0 to 4.0 psig and another regulator varied P_C from 1.0 to 5.5 psig. This range of pressures was chosen as it yielded drop production in the dripping regime of the microfluidic device [29]. Drops were generated with lengths ranging from 100 μm to 250 μm . To evaluate the performance of the pump, P_D was held constant at 1.0 psig and P_C was increased and decreased by 0.5 psig. The step changes shown in Figure 4(E) were performed in triplicate for the three different P_D values used. Each P_D value was set during a different operational cycle. Figure 4(E) shows one of the replicates for step changes of P_C . Figure 4(F) shows a detailed section of Figure 4(E) where the set point is changed from 2.5 psig to 5.0 psig as well as the average t_R , t_S , OS , and accuracy values across all step changes and all replicates. The average OS for the changes in P_C was $26.8 \pm 4.2\%$, the average t_R and t_S was 0.74 ± 0.07 seconds and 1.23 ± 0.16 seconds respectively, and the average accuracy was 0.016 ± 0.001 psi or 0.3% of the full span of pressures.

There was no significant difference between pressure regulation of the continuous oil phase and dispersed water phase. The fluid being pressurized mainly affects the damping of the pressure regulation, or how much the pressure oscillates [69]. The amount of damping is proportional to the viscosity of the fluids. Since the water and oil phases have similar viscosities, 1 mPa·s and 1.24 mPa·s respectively, both phases have similar dampening effects.

Drop Production

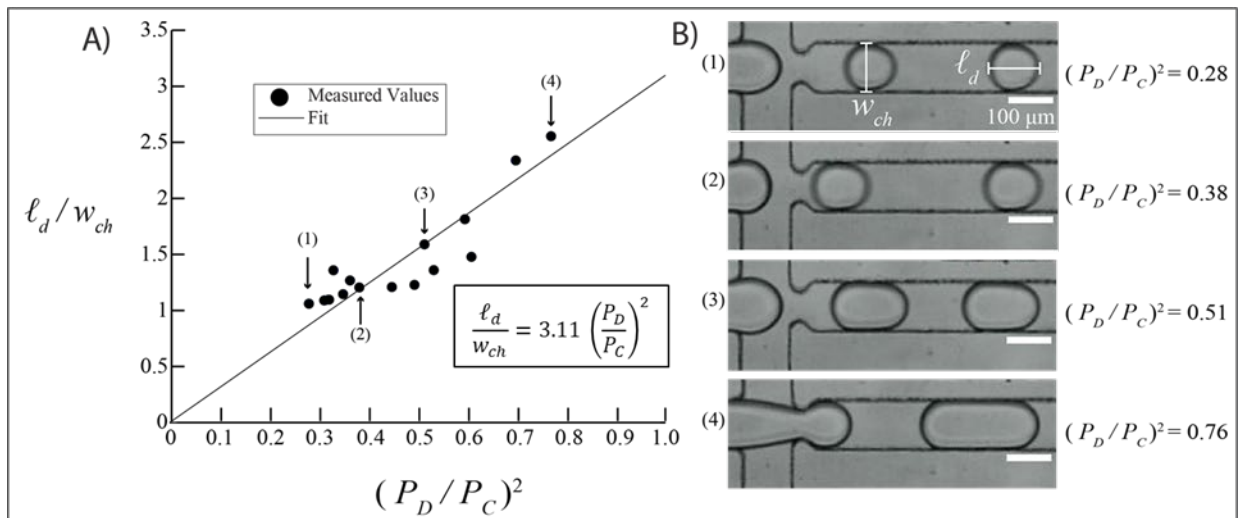


Figure 5. Microfluidic drop production using the pneumatic pressure pump. A) Drop length ℓ_d normalized by w_{ch} as a function of applied pressures $(P_D/P_C)^2$ using the in-house pressure pump. A fit (solid line) was made using equation 1 with an α value of 3.11 ($R^2 = 0.799$). Error bars are displayed but are not visible. B) Selected images of the drop-making process where the dispersed phase extends into the exit channel past the constriction and is pinched off into drops. Scale bars indicate 100 μm .

Finally, we evaluated if the pressure pump can create microfluidic drops of different sizes based on the pressures used to drive microfluidic flow. A plot of ℓ_d/w_{ch} as a function of $(P_D/P_C)^2$, shown in Figure 5(A), demonstrates that there is a power-law relationship between the normalized drop length and the pressure ratio that matches the relationship described in past literature [72]. Linear regression was used to determine the value of the scalar constant, α in

equation (1). α was found to have a value of 3.11 with the fit having a R^2 value of 0.799, Figure 5(A). This R^2 value was found to be a reasonable fit for several reasons. Firstly, we tested values of P_D / P_C that are larger than those tested by Ward *et. al.*, and equation (1) appears to have a poorer fit at those values [72]. Additionally, there is no universal scaling law for drop lengths and applied pressures in flow-focusing microfluidic devices [27]. Therefore, we chose an scaling law that captures only the essential parameters during these experiments [21]. These phenomenological models are effective for designing and testing flow-focusing microfluidic devices without relying on more recent machine-learning based models [28]. As expected, drops increase in size as P_D is increased relative to P_C . An average of 200 drops were analyzed per condition. Selected still images using brightfield microscopy depict drop production under varying pressure ratios (Figure 5(B)).

Discussion

The pneumatic pressure pump presented here is an advancement towards more open-source versions of these pumps. The pump in this work uses a single Arduino microcontroller to control four purpose-built regulators to provide accurate pressure regulation that can drive flow in microfluidic devices. Frank *et. al.* is the only comparable pump that did not use an Arduino controller and only Gao *et. al.* also used a single controller to control four regulators. The only specialty components of the pump are the proportional solenoid valves and the pressure sensors, components which end users can exchange for other versions depending on their specific downstream application. Only Watson and Senyo also used custom dual-valve regulators, all other comparable systems use commercial regulators. We create a GUI in Python, a popular and open-source programming language, while Watson and Senyo and Gao *et. al.* chose C++.

Watson and Senyo's pump are the most like our pump, with respect to the components used; however, we use our pump to drive flow, while Watson and Senyo actuated microfluidic valves. The components used in comparable pressure pumps is listed in Table 1.

Table 1. Comparison of components across published pressure pumps

Pump	Controller	Regulators	Number of regulators per controller	GUI Language	Application
Presented here	Arduino	Custom	4	Python	Driving flow
Frank <i>et. al.</i> 2016	Commercial Fieldbus	Commercial	1	Python	Driving flow
Watson and Senyo 2016	Arduino	Custom	1	C++	Actuating valves
Gao <i>et. al.</i> 2020	Arduino	Commercial	4	C++	Driving flow

Pneumatic pressure pumps have several advantages over syringe pumps and hydrostatic pumps when driving flow in microfluidic devices. Compared to syringe pumps, pneumatic pumps have smaller flow rate fluctuations and faster response times [6], a wider range of usable pressures compared to hydrostatic pumps [8], and more flexibility in the sizes of vessels available. Syringe capacities are limited to smaller volumes, ranging between 1 mL to 50 mL. Additionally, elevating large vessels above small microfluidic devices in the case of hydrostatic pressure pumps may not be practical for all applications. By contrast, silicone septa are available for 15 mL and 50 mL conical tubes and 100 mL to 10 L glass bottles (Figure 2(B)). Even smaller vessels such as 1.5 mL to 2 mL microcentrifuge tubes can be sealed with epoxy. All these sealed vessels can be used with pneumatic pressure pumps.

The pressure pump presented here utilizes customizable and easily assembled pressure regulators. The dual proportional valve design is similar to Watson and Senyo's pump [10], yet is

easier to assemble because it does not require a custom manifold and all four regulators are controlled from a single microcontroller. In our system, the solenoid valves use compression fittings upstream and downstream of the valve (Figure 2(C)). This allows for the use of hard plastic tubing at these connections followed or preceded by soft tubing to connect the valves to the other pneumatic components. These connections allow users to avoid using custom-machined housings and only requires typical barbed tubing connectors. Additionally, having all the pressure regulators controlled from a single microcontroller eliminates the need to use a bootloader, or an external Arduino programmer, when uploading the control scheme. Each solenoid valve is controlled from a transistor switch with a relatively simple circuit design (Figure 1(B)). The circuitry fabrication relies on through-hole soldering which is more accessible for users without a strong background in circuit assembly (Figure 2(D)). A simple proportional scheme is used to control the pressure regulators; however, future users could implement another control scheme if desired. The tubing connections and the use of one microcontroller for multiple pressure regulators makes the pressure regulator presented here the most customizable and accessible to-date.

Our pneumatic pressure pump has a higher settling time, t_s , when compared to Watson and Senyo's regulator [10], and the same t_s when compared to Gao *et al.*'s commercial pressure regulator [11]. The pump presented here has a t_s of less than two seconds, the t_s of Watson and Senyo's regulator was approximately 29 milliseconds [10], and Gao *et al.*'s pressure pump had a t_s of less than two seconds [11]. However, t_s less than two seconds are adequate for changing the pressures during drop production and other long-term microfluidic processes since frequent pressure changes during microfluidic processes are uncommon once the target drop size is

reached. A comparison of the t_S values for previously published pneumatic pressure pumps is presented in Table 2.

Table 2. Comparison of pressure regulation variables across published pressure pumps

Pump	Tested Pressure Range (psig)	t_R (s)	t_S (s)	OS (%)	Accuracy (psig)	Cost per channel (USD)	Overall Cost (USD)	Number of channels
Presented here	[1, 10]	0.74 ± 0.07	1.23 ± 0.16	26.8 ± 4.2	0.016 ± 0.001	602	2,400	4
Frank <i>et al.</i> 2016	[0, 14.5]	N/A	N/A	N/A	0.14 ± 0.04	792	N/A	1
Watson and Senyo 2016	[3, 29.5]	0.01 ± 0.01	0.03 ± 0.01	39.9 ± 25.2	0.12 ± 0.06	201	1,730	2
Gao <i>et al.</i> 2020	[0, 14.5]	N/A	< 2	N/A	0.03	500	3,000	4

The pneumatic pressure pump presented here has an improved overshoot and accuracy compared to the pressure regulator from Watson and Senyo [10]. The average overshoot of our pump is 15.1% without flow and 26.8% during drop-making, while Watson and Senyo reported an average of 39.9% with the same range of pressures. The overshoot for our pump could be improved with an inlet pressure less than 14 psig and closer to the maximum pressure used during the drop-making process. The average accuracy of our pump is 0.01 psig without flow and 0.016 psig during drop-making, while Watson and Senyo's pump reported an accuracy of 0.12 psig with the same range of pressures. The improved accuracy of our experiments could be due to the solenoid valves used or the proportional gain used in the control scheme. Gao *et al.* [11], did not report an overshoot percentage. The commercial regulators that Gao *et al.* used had an accuracy of 0.03 psig. However, an accuracy of less than 1% of the target pressure is adequate for driving flow in microfluidic devices. A comparison of the OS percentage and accuracy values for previously published pneumatic pressure pumps is presented in Table 2.

At this time of writing, our pneumatic pressure pump is costlier than the pump published by Watson and Senyo, but is slightly less costly than the pump published by Gao *et al.* The costliest components for each of the pumps are the pressure regulators. Our pump uses two proportional solenoid valves that cost \$544 for a pair, Watson and Senyo used valves that cost \$140 for a pair, and Gao *et al.* used commercial regulators that cost \$435. Gao *et al.* had other components that increased the costs to \$750 per regulator, the Watson and Senyo's pump had a cost of \$200 per regulator, and our pump had a cost of \$600 per regulator. Comparing the total cost of the pneumatic pressure pumps is only applicable between the pump presented in this work and the pump presented by Gao *et al.* since both pumps were both designed to drive flow, while the total cost of the pump presented by Watson and Senyo incorporates the solenoid valves used to actuate the microfluidic valves. Our pump system is slightly cheaper despite using more costly pressure regulators. This cost difference is due to Gao *et al.* using different pneumatic connections, an acrylic housing, and different pressure sensors and actuators. Though slightly more expensive, our proportional solenoid valves improved performance with respect to overshoot and accuracy, and the solenoid valves we used are also more easily assembled. The costs of previously published pneumatic pressure pumps is presented in Table 2.

The pneumatic pressure pump can create microfluidic drops in a consistent and precise manner. Figure 5A shows that a range of drop sizes can be created using the same microfluidic drop maker based upon the ratio of applied pressures $(P_D/P_C)^2$. The scaling equation relates the normalized drop length $\ell_{d/wch}$ to the applied pressure ratio $(P_D/P_C)^2$. A linear regression was performed that yields a scalar multiplier, α , which was 3.11 in this work, comparable to a value of 5.22 in Ward *et al.* [72]. The coefficients are of the same order of magnitude, yet vary due to

slight differences in device geometries [21]. The drops produced were monodisperse with average variances less than 1%.

Conclusion

The pneumatic pressure pump presented in this paper is an accurate and accessible pump for driving flow in microfluidic devices. The pump uses an open-source microcontroller and uses a GUI written in the attainable and open source language Python. The pump relies on pressure regulators that utilize a dual proportional solenoid design. A single microcontroller is used to control four pressure regulators with transistor switches. All pneumatic connections use easy-to-assemble barbed, compression, or luer taper tubing fittings contained in a 3D printed enclosure.

The pump presented here can rapidly and accurately change and maintain changes in pressure. The average rise times (t_r) and settling times (t_s) with or without flow were less than one second and less than two seconds, respectively. The pump had an average overshoot percentage of 27% and was accurate within 0.02 psig, during drop-making. The cost per regulator was approximately \$600, which is three times costlier than Watson and Senyo's regulator, but a quarter of the cost of the commercial regulators used by Gao *et al.* The pump presented in this work is an improvement over open-source pressure regulators; although it had a much slower settling time than Watson and Senyo's open source pressure regulator, it had an improved overshoot percentage and accuracy. This pump also used the first open-source pressure regulators to drive microfluidic flow, specifically to make microfluidic drops.

The pump presented here was evaluated for its ability to produce drop sizes proportional to the pressures used to drive flow during the drop-making process. The pump was able to produce drops in a flow-focusing microfluidic device whose dimensions are proportional to the pressures

used to drive fluid flow, similar to the work published in Ward *et al.* [72]. Future directions include the implementation of the pressure pump for microfluidic process that utilize single-phase flow, such as organs-on-a-chip that require long infusion times [74-76], or more complicated drop-based microfluidic processes, such as drop injection, merging, and splitting [52, 77, 78]. This pressure pump could also easily operate multiple drop-making devices in parallel with the pressurized reservoirs going to several devices at the same time. We envision applying the pressure pump to improve particle encapsulation into drops, as each pressurized vessel can be easily stirred to prevent the particles from settling in the vessel. Finally, this pump can be used for any number of applications that require precision fluid handling for scientists or engineers at a reasonable cost.

Acknowledgements

The authors would like to acknowledge Dr. Stephanie McCalla for the advice to use the open source Arduino and Dr. Stephan Warnat for advising on the pressure regulation experiments.

Conflict of Interest

The authors declare that they have no known competing financial interests or personal relationships that could have appeared to influence the work reported in this paper.

Data Availability Statement

The data that support the findings of this study are available upon reasonable request from the authors.

Funding Statement

This work was supported by the Defense Sciences Office, DARPA grant W911NF-17-2-0034, National Institutes of Health (NIH) 1R21AI151923, and National Science Foundation (NSF) CAREER DMR-1753352. H.S.S. gratefully acknowledges support from National Institutes of Health (NIH) 3U01EB029242-02S2.

CHAPTER FOUR

MASS CONSERVATION OF DROP-BASED MICROFLUIDIC
SPLITTING AND MERGING (SAM)
DEVICES

Contribution of Authors and Co-Authors

Manuscript in Chapter 3

Author: Humberto S. Sanchez

Contributions: H.S.S. designed research, performed research, analyzed data, and wrote the manuscript

Co-Author: Connie B. Chang

Contributions: C.B.C designed research and wrote the manuscript

Manuscript Information

Humberto S. Sanchez and Connie B. Chang

Microfluidics and Nanofluidics

Status of Manuscript:

Prepared for submission to a peer-reviewed journal

Officially submitted to a peer-reviewed journal

Accepted by a peer-reviewed journal

Published in a peer-reviewed journal

Springer

Abstract

Several split-and-merge (SAM) drop-based microfluidic devices have been used to perform biochemical assays inside microfluidic drops. Current studies using these devices have been limited to their applicability and not their design, operation, or optimization. Here we present a planar SAM device layout along with a hydraulic network that is used to split incoming drops into three different volumetric ratios and merge one population of the split drops with an incoming aqueous stream to create drops of various volumes. The merging efficiency was optimized with these three SAM device geometries by altering both the incoming drop volume and the inlet drop spacing. We derived a mass-balance based drop model to predict drop volume changes which is in good agreement with our two other empirical models. This work can be used to design future SAM devices to control both the drop splitting and resulting drop volume after merging.

Introduction

Drop-based microfluidic technology enables the creation of large numbers of water-in-oil drops where biologic samples can be encapsulated and observed [79]. These picoliter-sized drops can contain enzymes, viruses, and cells in an aqueous buffer or medium [14, 15, 17, 18]. These aqueous environments are then dispersed in a continuous oil phase and stabilized with a surfactant to prevent coalescence [12, 13]. Each drop can be considered a discrete bioreactor where the contents can be assayed [51, 80-83]. However, to perform assays within the drops they need to be manipulated on microfluidic devices.

Assays within microfluidic drops often rely on two distinct drop manipulations; splitting drops into smaller drops [45, 49] and merging drops with an additional aqueous phase [58]. Drop merging is performed either to add a controlled volume of reagents into the mother drop, such as fluorescently labelled reagents for enzymes and cells or more cells for viruses [42, 51, 52]. Drop splitting is performed for several reasons that are tied to the addition of the reagents. Firstly, splitting the mother drops after merging with reagents can reduce the amount of background fluorescent signal in the daughter drops [42]. Secondly, splitting drops before merging controls the volume of the daughter drops which determines their thermal stability during assays [44]. Splitting the mother drops also reduces the volume of contaminants in the assayed drops, this is especially important for intracellular assays [43, 44]. Finally, splitting and merging drops can be used to passage the cell or virus population in the drops which enables evolutionary studies of small populations [52]. Drop splitting and merging (SAM) is often performed sequentially on a microfluidic device and has been used to perform biochemical assays, yet little is described in the literature on the required flow rates and device geometries to achieve specific drop splitting ratios or drop volumes after merging.

In this work, we describe the design process for drop-based SAM microfluidic devices and develop a mathematical model to quantify drop volume changes within the devices. Our design process relies on modelling the fluid flow within the microfluidic devices to estimate the drop splitting ratios. This model allows us to create multiple SAM devices with different splitting ratios after altering the channel widths in the devices. We test the effects of input drop volume on device operation and find the flow rates needed to achieve optimal drop merging for each drop size in the SAM devices. Finally, we develop a theoretical model to estimate drop volume

changes based on the mass balance of drops within a SAM device. We find that this theoretical model matches well with two empirical models we develop.

Methods and Materials

Variable symbols and definitions used in this work are listed in Table 1. The subscript i is used to denote channel name for dimensions, flow rates, and the drop area in that channel. The drop area, a_i , was used to quantify drop changes for both splitting and merging. This measurement was chosen because it is directly obtained using the drop image analysis software we used. Moreover, the drops in the SAM devices travel in channels with different widths, making drop length an inadequate metric for their volume.

Table 1. List of Variables

Variable	Unit	Description
h_i	μm	Channel height
w_i	μm	Channel width
l_i	μm	Channel length
$a_{c,i}$	μm^2	Cross sectional area
Q_j	$\mu\text{l hr}^{-1}$	Flow rate
R_i	$\mu\text{g s}^{-1} \mu\text{m}^{-4}$	Fluid resistance
ΔP_i	$\mu\text{g s}^{-2} \mu\text{m}^{-1}$	Pressure Drop
μ	$\mu\text{g} \mu\text{m}^{-1} \text{s}^{-1}$	Dynamic viscosity
L_i	μm	Drop length
A_i	μm^2	Drop area
V_i	μm^3	Drop volume
N_i	--	Number of drops

Device Design

The SAM devices all had the same design layout, as shown in Figure 1. Drops are injected in the device, where they encounter a spacer oil and enter the inlet channel (Fig. 1(B)). The purpose of the spacer oil is to regulate the spacing between the incoming drops.

Subsequently, the drops in the inlet channel proceed to the split junction, where they are divided into two separate drops (Fig. 1(C)). One set of drops enter the split channel and exits the device through the split drops outlet, while the other set of drops enter the shunt channel. Within the shunt channel, the drops converge with the oil stream before entering the pre-merge junction (Fig. 1(C)). At the merge junction, the drops in the pre-merge channel come into contact with the aqueous stream in the presence of an electrical field generated by positive (red) and ground (green) salt electrodes (Fig. 1(D)). The presence of an electrical field destabilizes the water/oil interface, enabling the addition of the new aqueous stream to the surfactant-stabilized incoming drops [54]. Finally, these merge drops exit the device through the split and merged drops outlet.

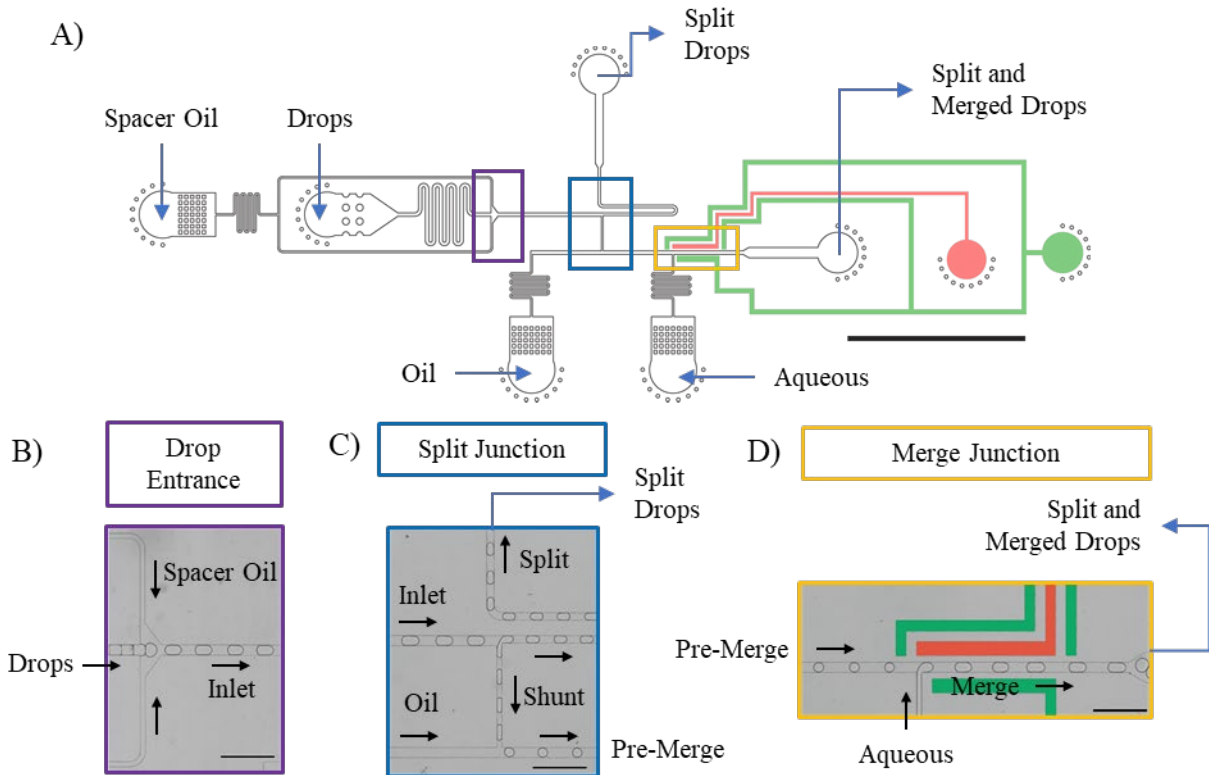


Figure 1. A drawing of a representative SAM device illustrating the layout of the devices of this work. A) An image of the entire device showcasing fluid inputs and outputs indicated by arrows. The drop entrance, split junction, and merge junction are enclosed in boxes, and the electrodes are false colored. Scale bar = 5 mm. B) An enlarged view of the drop entrance displaying channel labels and flow directions. Scale bar = 500 μm . C) An enlarged view of the split junction displaying channel labels and flow directions shown. Scale bar = 500 μm . D) An enlarged view of the merge junction with false-colored salt electrodes, accompanied by channel labels and flow directions shown. Scale bar = 500 μm .

Three SAM devices were tested in this work, each featuring the same channel layout, but varying channel widths in the two channels responsible for drop splitting: the split channel and the shunt channel (Fig. 2). These devices are referred to as *Large Split*, *Medium Split*, and *Small Split*, based on the proportion of the incoming drop that enters the split channel. The differences in channel widths and their corresponding drop splitting capabilities are shown in Figure 2. For example, the *Large Split* device has a shunt channel width (w_{shunt}) of 40 μm and a split channel width (w_{split}) of 100 μm . The inlet channel and pre-merge channel, which are the channels before

and after the split junction, have a consistent width of 100 μm widths across all devices (w_{inlet} and $w_{\text{pre-merge}}$). The channel widths and heights for all three SAM devices are listed in Table 2. The channel heights for each geometry were determined using an optical profilometer and remain the same for all SAM devices.

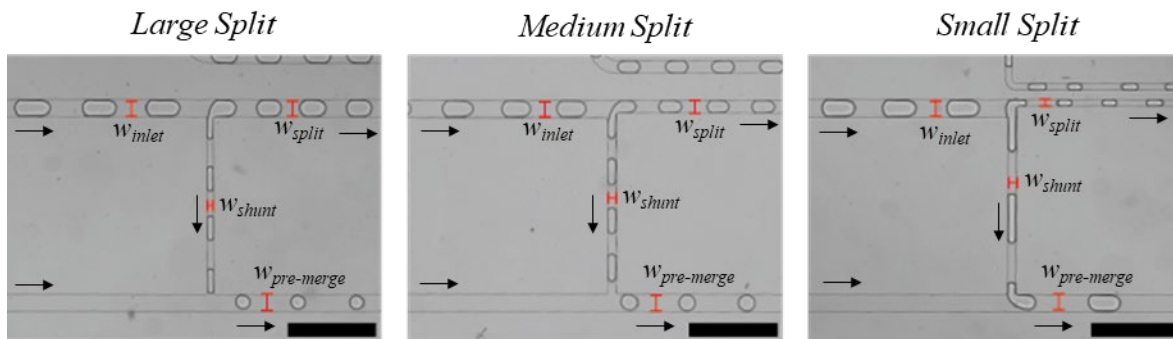


Figure 2. Images of the split junction for the three SAM devices tested in this study. The devices have varying widths at the split and shunt channels, resulting in different splitting ratios for the incoming drops. The channel widths at the pre-merge and inlet channels are held constant at 100 μm . Arrows indicate the fluid flow directions. Scale bars = 500 μm .

TABLE 2. Channel widths and heights of interest for the three SAM devices presented.

	w_{inlet} (μm)	$w_{\text{pre-merge}}$ (μm)	w_{shunt} (μm)	w_{split} (μm)	h_{all} (μm)
<i>Large Split</i>	100	100	40	100	47
<i>Medium Split</i>	100	100	75	50	46
<i>Small Split</i>	100	100	40	50	49

Device Fabrication

Microfluidic devices were fabricated with poly(dimethyl siloxane) (PDMS) (Sylgard 184) channels, using standard soft lithographic techniques [71]. These channels were then oxidized with oxygen plasma (Harrick Plasma; cat. no. PDC-001) for 60 s at high power (30 W) and 700 mTorr oxygen pressure. The oxidized PDMS channels were then bonded to glass. After bonding, the channels were made fluorophilic by injecting of a solution of (tridecafluoro-1,1,2,2-

tetrahydrooctyl) trichlorosilane (1 v/v%) (Gelest) in a fluorinated oil Novec™ 7500 (3M). The devices were left open to air to allow for solvent evaporation.

Salt Electrode Operation

The devices were equipped with dead-end salt electrode channels for drop merging [56]. These salt electrodes consisted of a positive and ground electrode channel, both filled with a 5 M NaCl solution from syringes (1 mL, BD). The salt solutions were injected into the electrode channels and maintained constant pressure using the anti-syphon plate of syringe pumps (NE-500, New Era Pump Systems Inc.). The electric signal was generated using a National Instruments Data Acquisition System (NI-DAQ) with a 20 kHz and 1 V signal, which was subsequently amplified to 200 V using a Trek Model 2220-CE amplifier. The leads from the amplifier were connected to the needle shafts (McMaster-Carr; cat. no. 75165A688) of the syringes containing the salt solutions.

Two-Phase Drop Composition

The water-in-oil drops consisted of an aqueous phase of phosphate-buffered saline (PBS) solution dispersed in a continuous fluorinated oil of NOVEC 7500 (3M). To stabilize the drops, a fluorinated surfactant consisting of a polyethylene glycol head with perfluorinated polyether tails (RAN Biotechnologies) (1.5 w/w%) was added to the oil phase.

Video Capture and Analysis

The microfluidic devices were placed on top of an inverted microscope (Nikon, TE2000, 4X objective lens) equipped with a high-speed camera (VEO-710L, Vision Research) to capture drop motion in the microchannels at a frame rate of 2,500 fps). To analyze drop parameters, such

as area and velocity, 5,000 frames of high-speed footage was recorded and processed using droplet morphometry and velocimetry (DMV) software [73]. The inlet channels, split junction, and merging junction were simultaneously imaged, and then the channels of interest were cropped from the original footage and analyzed separately from one another using the DMV software.

Fluid Delivery

Fluid were injected into the SAM devices using syringe pumps (NE-500, New Era Pump Systems Inc.). The four inputs included drops, spacer oil, oil stream, and aqueous stream, as seen in Figure 1. The pumps were oriented vertically to allow the drops to float towards the syringe (3 mL, BD) outlet. During device operation, the three non-drop inputs were injected into the device with the drop inlet plugged. The drops were first flowed through the needle ((McMaster-Carr; cat. no. 75165A688) and tubing (Scientific Commodities Inc., 136 BB31695-PE/2) and then allowed to flow into the device. The devices were operated for 10 minutes before data collection began and there was a gap of 5 minutes between flow rate change and data collection.

Input Drop Production

For each SAM device, three different drop inputs were used, each with a target length of 200, 160, and 130 μm , respectively. These drops were generated using a separate flow-focusing drop-maker device with a 50 μm constriction and a device height of 51 μm [23]. The drop lengths were verified through DMV analysis prior to collection and stored at 4 °C prior to usage. The targeted drop lengths and corresponding actual drop lengths used in the three SAM devices are listed in Table 3.

TABLE 3. Input drop lengths used in the three SAM devices

Drop Size	L_{inlet} (μm)	Geometry	L_{inlet} (μm)
	Target		Actual
<i>Large drops</i>	200 ± 10	<i>Large split</i>	217 ± 2
		<i>Medium split</i>	191 ± 1
		<i>Small split</i>	215 ± 2
<i>Medium drops</i>	160 ± 10	<i>Large split</i>	157 ± 1
		<i>Medium split</i>	160 ± 1
		<i>Small split</i>	163 ± 3
<i>Small drops</i>	130 ± 10	<i>Large split</i>	126 ± 2
		<i>Medium split</i>	131 ± 2
		<i>Small split</i>	129 ± 1

Modelling and Analysis Pipeline

We used a several Python scripts to both model the device flow rates for each condition tested and to analyze the drop data generated from the DMV software. A spreadsheet was created with the channel lengths, widths, and heights for each SAM geometry. These dimensions were imported into the Python integrated development environment (IDE) to calculate the resistances for each channel. These resistance values are then used in a linear solver to calculate the predicted flow rates in the devices. To make analysis of the drop data easier, the spreadsheet generated from the DMV software was converted into a data frame. Each spreadsheet exported from the DMV software contains two tables, one with the summary statistics for the measurements from each drop and one containing every drops measurement. We first extracted the latter table and converted it into a data frame, then we appended the flow rates used in that experiment to that data frame, and finally concatenated all the channels in that experiment into a single file. This results in a single file that has all the average measurements for each drop in each channel along with the flowrates, device geometry, input drop size, and flow rates used during the drop measurements.

Modelling

Device Modelling

The SAM devices in this study have known input flow rates and unknown flow rates that can be solved using the electric circuit analogy. The electric circuit analogy is commonly employed to model the steady-state flow within microfluidic devices, based on several fundamental principles [38]. Firstly, the pressure drop within a channel, ΔP_i , is equal to flow rate within that channel, Q_i , multiplied by the hydraulic resistance of the channel, R_i , such that $\Delta P_i = Q_i R_i$. Secondly, when two channels intersect, there is no mass accumulation at the intersection, adhering to the principle of conservation of mass. Lastly, when channels branch out to form a closed loop, the pressure drop in the branches are equal, following the principle of conservation of energy.

In the SAM devices, there are five channels with unknown flow rates: Q_{inlet} , Q_{split} , Q_{shunt} , $Q_{pre-merge}$, and Q_{merge} (Figure 4). The four fluid inputs into the device, $Q_{spacer-oil}$, Q_{drops} , Q_{oil} , and $Q_{aqueous}$ can be modeled as constant flow rate sources (Figure 3). The channels downstream of the of split junction (Q_{split} , Q_{shunt} , $Q_{pre-merge}$, and Q_{merge}), which impact the splitting ratios, each have their own flow rate, flow direction, and resistance. In Figure 4, each black circle represents a node, where two or more channels intersect. The two outlets of the devices are represented as grounds, and the outlets of the device lead to the atmospheric sink and form a closed loop with each other. The channel resistances are calculated using equation (1) due to their rectangular geometry [84] while the tubing resistances are calculated using equation (2) due to their circular geometry [85].

$$R_{channel} = \frac{12\mu_d l_i}{w_i h_i^3} \left[1 - \frac{192h_i}{\pi^5 w_i} \sum_{n=1,3,5}^{\infty} \frac{1}{n^5} \tanh\left(\frac{n\pi w_i}{2h_i}\right) \right]^{-1} \quad (1)$$

$$R_{tubing} = \frac{8\pi\mu_c l}{a_c^2}. \quad (2)$$

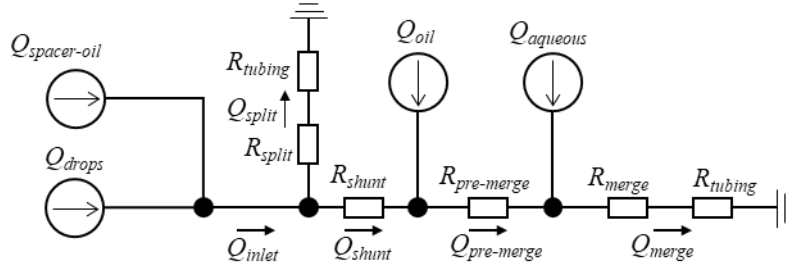


Figure 3. The network diagram for SAM devices with fluid flow sources (Q), flow rates in the channels with their directions (Q), and channel resistances (R). The nodes, represented by filled-in circles, indicate the points where the channels meet.

The network diagram for the SAM devices can be used to formulate a system of linear equations that can easily be solved. Equations (3) through (6) describe the mass conservation at the four nodes in a SAM device, while equation (7) states that the pressure drops from the split junction to both outlets of the device are equal due to the conservation of energy.

$$Q_{drops} + Q_{spacer-oil} = Q_{inlet}, \quad (3)$$

$$Q_{split} + Q_{shunt} = Q_{inlet}, \quad (4)$$

$$Q_{oil} + Q_{shunt} = Q_{pre-merge}, \quad (5)$$

$$Q_{pre-merge} + Q_{aqueous} = Q_{merge}, \quad (6)$$

$$Q_{merge}(R_{merge} + R_{Tubing}) + Q_{pre-merge}R_{pre-merge} + Q_{shunt}R_{shunt} = Q_{split}(R_{split} + R_{Tubing}). \quad (7)$$

The system of equations (3) through (7) was then solved using a Python script. All the flow rates, Q , in the equations can be listed as a column vector on the left-hand side of equation (8) and the relationships between these flow rates can be arranged into matrix A , as shown in equations

(8) and (9). The solution for the flow rates in the column vector is then equal to the dot product between the inverse of matrix A and the known input flow rates, as given in equation (8). Representative input flow rates for the three SAM devices, along with the resulting splitting ratios calculated from the Python script, are shown in Table 4. These split ratios illustrate how the three different SAM geometries generate three distinct splitting ratios based on the electric circuit analogy model.

$$\begin{bmatrix} Q_{drops} \\ Q_{spacer-oil} \\ Q_{oil} \\ Q_{aqueous} \\ Q_{inlet} \\ Q_{split} \\ Q_{shunt} \\ Q_{pre-merge} \\ Q_{post-merge} \end{bmatrix} = \mathbf{A}^{-1} \cdot \begin{bmatrix} Q_{drops} \\ Q_{spacer-oil} \\ Q_{oil} \\ Q_{aqueous} \\ 0 \\ 0 \\ 0 \\ 0 \\ 0 \end{bmatrix} \quad (8)$$

$$\mathbf{A} = \begin{bmatrix} 1 & 0 & 0 & 0 & 0 & 0 & 0 & 0 & 0 \\ 0 & 1 & 0 & 0 & 0 & 0 & 0 & 0 & 0 \\ 0 & 0 & 1 & 0 & 0 & 0 & 0 & 0 & 0 \\ 0 & 0 & 0 & 1 & 0 & 0 & 0 & 0 & 0 \\ 1 & 1 & 0 & 0 & -1 & 0 & 0 & 0 & 0 \\ 0 & 0 & 0 & 0 & -1 & 1 & 1 & 0 & 0 \\ 0 & 0 & 1 & 0 & 0 & 0 & 1 & -1 & 0 \\ 0 & 0 & 0 & 1 & 0 & 0 & 0 & 1 & -1 \\ 0 & 0 & 0 & 0 & 0 & -(R_{split} + R_{tubing}) & R_{shunt} & R_{pre-merge} & (R_{post-merge} + R_{tubing}) \end{bmatrix} \quad (9)$$

TABLE 4. Modelled flow rates and split ratios for the three SAM devices

Flow rates				Splitting Ratios		
Geometry	Q_{drops} ($\mu\text{l hr}^{-1}$)	$Q_{spacer-oil}$ ($\mu\text{l hr}^{-1}$)	Q_{oil} ($\mu\text{l hr}^{-1}$)	$Q_{aqueous}$ ($\mu\text{l hr}^{-1}$)	Q_{split}/Q_{inlet}	Q_{shunt}/Q_{inlet}
<i>Large Split</i>	500	1000	500	125	0.72	0.28
				250	0.73	0.27
				500	0.76	0.24
<i>Medium Split</i>	500	1000	500	125	0.55	0.45
				250	0.57	0.43
				500	0.59	0.41
<i>Small Split</i>	500	1000	500	125	0.25	0.75
				250	0.26	0.74
				500	0.27	0.73

Drop Modelling

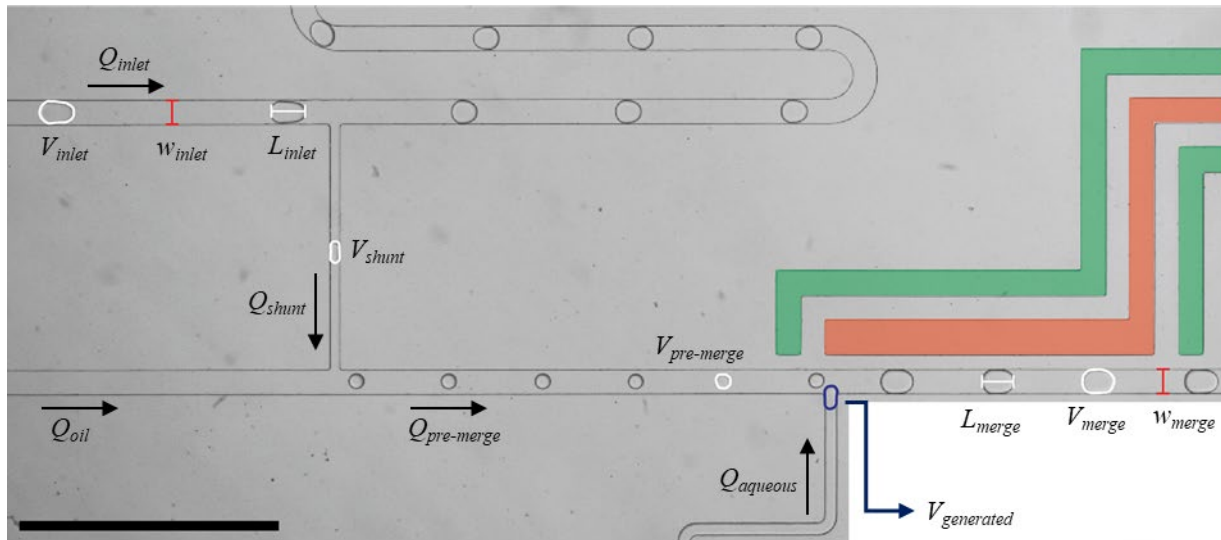


Figure 4. A representation of the split junction and the merge junction illustrating the two drop processes in a SAM chip. Drops from the inlet enter the splitting junction where the shunt drops are directed to be merged. The shunt channel combines with an additional oil stream and proceeds into the pre-merge channel. At the merge junction, the pre-merge drops intersect with an additional aqueous stream, resulting in the generation of merge drops due to the electrical field generated by the electrodes. The positive electrode is false-colored red, and the ground electrode is false-colored green. Scale bar = 1 mm.

The mathematical description of drop volume changes in SAM devices involves several variables, as shown in Figure 4, which represents both the split and merge junctions (Fig. 1(C) and (D)) used to alter drop volumes. By applying a mass balance to the drops (Eq. 10), the final drop volume can be determined as the sum of the drop volume before the merge junction, $V_{pre-merge}$, and the drop volume generated at the merge junction, $V_{generated}$. $V_{pre-merge}$ is equal to V_{shunt} (Eq. 10) and V_{shunt} can be determined based on the surrounding flow rates at the split junction (Eq. 11). The ratio between V_{shunt} and V_{inlet} should be approximately equal to the ratio between Q_{shunt} and Q_{inlet} from (Eq. 11) [45, 49]. Therefore, V_{shunt} can be predicted from V_{inlet} and Q_{inlet} , which are known inputs, and Q_{shunt} , which is a predicted value. $V_{generated}$ represents the additional drop volume added to $V_{pre-merge}$ at the merge junction. The merge junction geometry resembles a microfluidic T-junction, commonly used for drop creation in microfluidic devices [19]. A T-junction produces drops as a continuous oil phase flows perpendicular to an aqueous stream, similar to the merge junction, except that the continuous phase preceding the aqueous stream contains dispersed drops, $V_{pre-merge}$. The drop volume generated at a T-junction, $V_{generated}$, has been studied extensively and follows a simple scaling law [20, 86]. The scaling law (Eq. 12) estimates that the normalized drop length is proportional to the drop volume, $V_{generated} \approx L_{generated} / w_{merge}$, and equal to the ratio between $Q_{aqueous}$ and Q_{oil} . To maintain consistency in units, V_{merge} and V_{inlet} are converted to normalized drop lengths. By substituting the expression to estimate V_{shunt} (Eq. 11) and the scaling law to estimate $V_{generated}$ (Eq. 12) into the mass balance (Eq. 10), Equation (13) is obtained. Equation (13) utilizes the device model to estimate the split drop volume using the normalized drop length, L_{inlet} / w_{inlet} , from Q_{shunt} and Q_{inlet} (Figure 3). Equation (13) also employs the known linear scaling law for drop

generation to estimate the drop volume added to $V_{pre-merge}$ based on $Q_{aqueous}$ and Q_{oil} , which are known inputs, and a scalar multiplier, α , dependent on the device geometry.

$$V_{merge} = V_{pre-merge} + V_{generated} = V_{shunt} + V_{generated} \quad (10)$$

$$V_{shunt} \approx V_{inlet} \left(\frac{Q_{shunt}}{Q_{inlet}} \right) \quad (11)$$

$$V_{generated} \propto \frac{L_{generated}}{w_{merge}} = 1 + \alpha \left(\frac{Q_{aqueous}}{Q_{oil}} \right) \quad (12)$$

$$V_{merge} \propto \frac{L_{merge}}{w_{merge}} \approx 1 + \frac{L_{inlet}}{w_{inlet}} \left(\frac{Q_{shunt}}{Q_{inlet}} \right) + \alpha \left(\frac{Q_{aqueous}}{Q_{oil}} \right) \quad (13)$$

If equation (13) holds true for SAM devices, it can be used along with the device model to predict drop volume changes. Therefore, one of the goals of this work is to test the validity of equation (13). To achieve this, the drop volumes after merging, V_{merge} , will be measured based on the drop volumes added to the device, V_{inlet} , the splitting ratio, Q_{shunt} / Q_{inlet} , and the flow rates used to generate drops at the merging junction, $Q_{aqueous} / Q_{oil}$. Three inlet drop lengths, L_{inlet} , will be tested in three SAM devices (Table 2), where each SAM device has a different splitting ratio as shown in Table 4. Multiple $Q_{aqueous}$ and Q_{oil} flow rates will be experimentally tested to generate different V_{merge} values, which also affect the splitting ratio Q_{shunt}/Q_{inlet} (Table 4).

Results

Drop Merging Optimization

To optimize drop merging, the spacing between drops at the inlet was adjusted by manipulating Q_{drops} and $Q_{spacer-oil}$ (Fig. 1(B)), which in turn impacts the spacing of the drops in the shunt and pre-merge channels, as well $Q_{pre-merge}$ directly upstream of the injected aqueous phase (Fig. 1(D) and 3). Experimental variations in Q_{drops} and $Q_{spacer-oil}$ were carried out to assess their

effects on drop merging. During high-speed imaging of the merging junction (Fig. 1(D) and 5), four distinct drop merging regimes were observed. Figure 5 provides a time-lapse representation of these four different merging regimes.

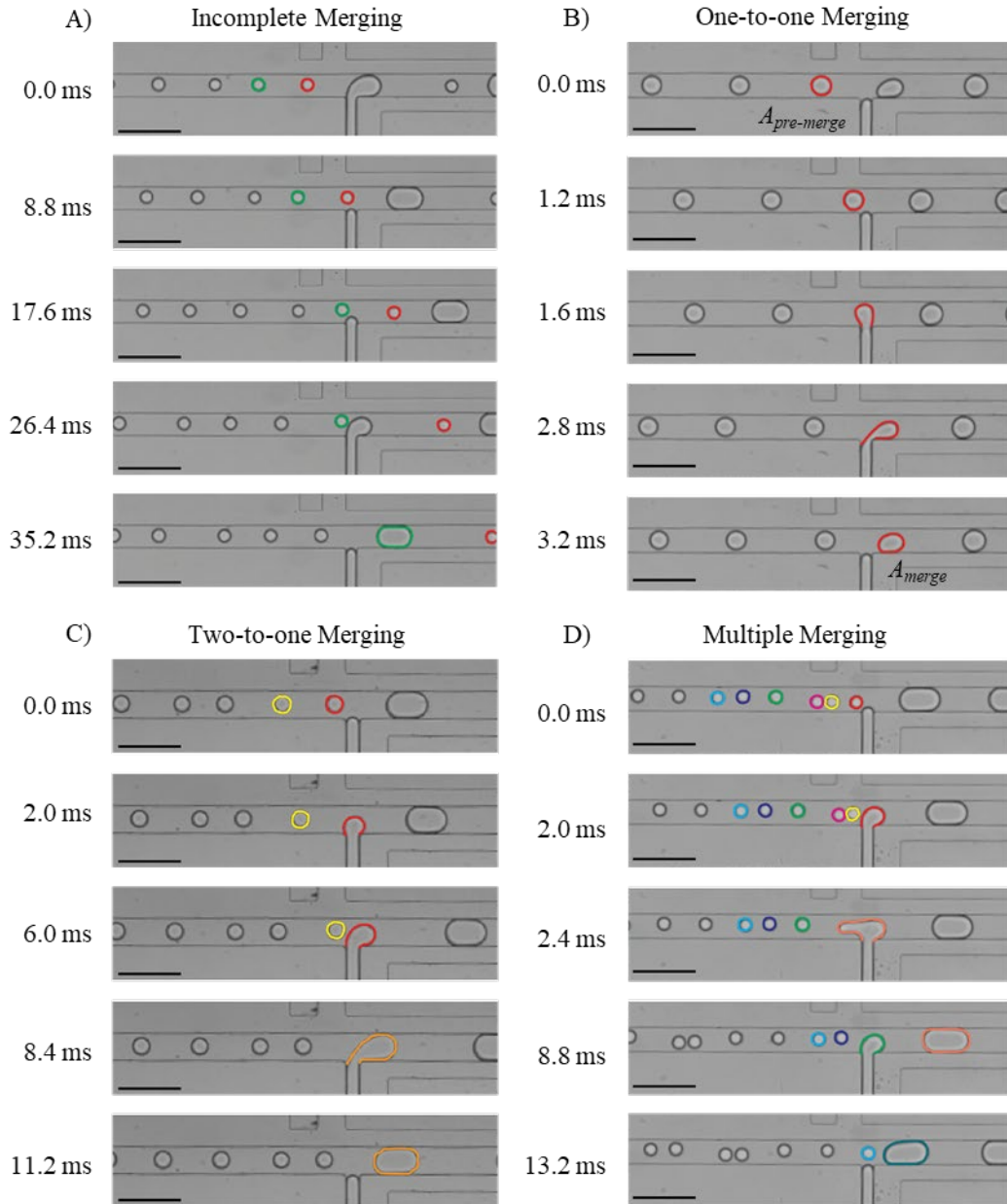


Figure 5. Image sequences demonstrating different merging regimes. A) Sequence of images illustrating incomplete merging, where the red drop is not merged with $Q_{aqueous}$ while the green drop undergoes merging. B) Sequence of images illustrating one-to-one merging after the red drop merges with $Q_{aqueous}$. C) Sequence of images illustrating two-to-one merging, where both the red and yellow drops merge with $Q_{aqueous}$ to form the orange drop. D) Sequencing of images illustrating multiple merging, with the red, yellow, and magenta drops merging to create the salmon drop, the green and blue drops merging to form the teal drop, and the cyan drop failing to merge with $Q_{aqueous}$. Scale bars = 250 μm . $A_{pre-merge}$ is shown in the first image of B) and A_{merge} is shown in the last image of B).

Four merging regimes were observed while varying Q_{drops} and $Q_{spacer-oil}$: incomplete, one-to-one, two-to-one, and multiple (Fig. 5). In the case of incomplete merging (Fig. 5A), only a fraction of the pre-merge drops are merged with the injected aqueous stream, $Q_{aqueous}$, resulting in smaller drops present in the merge channel. This occurs when $Q_{aqueous}$ is low compared to $Q_{pre-merge}$ and the rate of drop production at the merging junction is slower than the incoming drop rate. Incomplete merging can also occur when the incoming drop is too far away from the drop being generated, preventing the electrical field from coalescing the two aqueous phases, as seen in the red drop in Figure 5(A) and the cyan drop in Figure 5(D).

One-to-one merging (Fig. 5B), represents the optimal regime for the purpose of this study. In this regime, every pre-merge drop is merged with the aqueous stream, resulting in a single post-merge drop. Two-to-one merging (Fig. 5C) occurs when the pre-merge drops are spaced close together and the drop formation at the merging junction is slow enough to allow two pre-merge drops to collide with $Q_{aqueous}$. The multiple merging regime (Fig. D) occurs when a range of pre-merge drops, from zero to four, coalesce with $Q_{aqueous}$. Multiple merging can also occur when drops in the pre-merge channel exhibit disordered bubbly flow, with diameters smaller than the channel width and not following the same streamline [27]. The pre-merge drops for incomplete, one-to-one, and two-to-one merging shown in Fig. 5A-C, have diameters smaller than the channel width but travel along the same path. In contrast, the pre-merge drops for multiple merging do not travel along the same path and can bunch up together (Fig. 5(D)).

Each merging regimes results in distinct distributions of drop areas after merging, in yellow, relative to the drop areas before merging, outlined in blue (Fig. 6). Incomplete merging leads to a bimodal distribution of drop areas in the merge channel, with one distribution

overlapping with the pre-merge channel and another distribution of merged drops (Fig. 6(A)). One-to-one merging results in a prominent distribution of drop areas in the merge channel and a single distribution in the pre-merge channel with smaller drop areas, Figure 6(B). Two-to-one merging occurs when two pre-merge drops are merged with $Q_{aqueous}$ simultaneously, creating a single merge drop. Two-to-one merging results in a larger shift in drop area from pre-merge to merge compared to one-to-one merging, but still maintains a single distribution of merge drop areas (Fig. 6(C)). Multiple merging is unique in that there are multiple drop populations before merging. During multiple merging, the pre-merge drops are so closely spaced that some pairs of drops register as a single drop during DMV analysis, leading to a bimodal distribution of drop areas (Fig. 6(D)). Multiple merging also results in a bimodal distribution in the merge channel, with one population of unmerged drops and another population of merged drops (Fig. 6(D)). The merged drops population is skewed to the right due to the variety of pre-merge drops merged with $Q_{aqueous}$ (Fig. 6(D)).

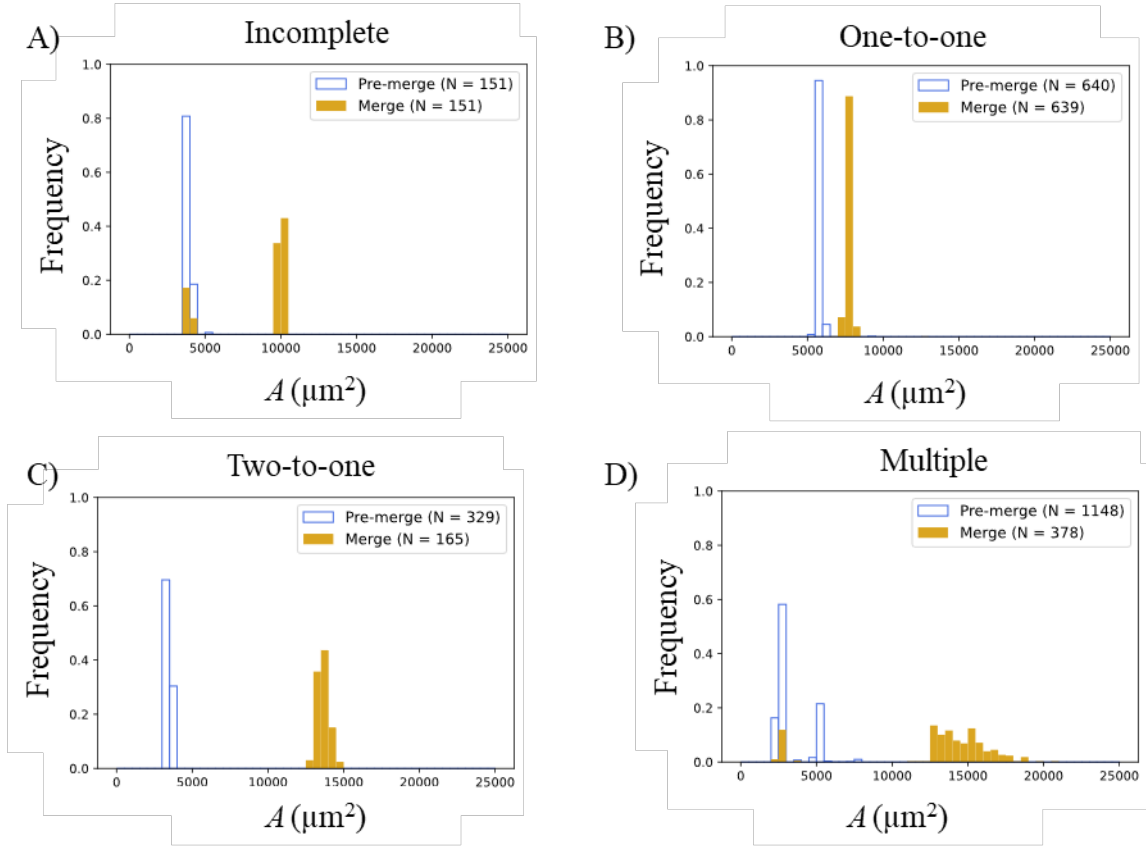


Figure 6. Merging regimes depicted by the distribution of drop areas before, outlined in blue, after, in yellow, merging. A) Distribution of drop areas resulting from incomplete merging. B) Distribution of drop areas resulting from one-to-one merging. C) Distribution of drop areas resulting from two-to-one merging. D) Distribution of drop areas resulting from multiple merging.

The merging efficiency of each SAM device (*Large, Medium, Small split*) with each drop size (*Large, Medium, Small drops*) is quantified using both the footage of the merging junction and the distribution of drop areas in the merge channel (Table 5). The merging efficiency, η_{merge} , is calculated using equation (14). Each drop in the merge channel is a result of a discrete number of pre-merge drops merged with $Q_{aqueous}$, denoted by j . For example, in Figure 5(A), the red drop has a j value of zero, while the green drop has a j value of one. Similarly, the orange drop in Figure 5(C) has a j value of two, and the salmon drop in Figure 5(D) has a j value of three. In equation (14), the number of drops with the same j value is represented as m_j . The merging efficiency, η_{merge} ,

is calculated as the sum of m_j multiplied by j , divided by the total number of drops in the merge channel, N_{merge} . It quantifies the average number of pre-merge drops merged with $Q_{aqueous}$ to form a single merge drop. Values of 1.00 for η_{merge} indicate that one-to-one merging was observed, values less than 1.00 indicate the presence of incomplete merging, and values greater than 1.00 indicate two-to-one or multiple merging. The footage of the merging junction and the A_{merge} distributions (Fig. 6) were used to determine the value of m_j for each drop in the merge channel and quantify the merging efficiency for each tested condition. The footage allowed us to observe the merging regimes, and the different populations in the A_{merge} distribution were binned to obtain values for m_j .

$$\eta_{merge} = \frac{1}{N_{merge}} \sum_{j=0}^3 j m_j \quad (14)$$

The Q_{drops} and $Q_{spacer-oil}$ values needed to achieve one-to-one merging were determined for each geometry and drop size. Drop merging was optimized by changing Q_{drops} and $Q_{spacer-oil}$ while keeping the other flow rates, Q_{oil} and $Q_{aqueous}$, constant (Table 5).

Initially, Q_{drops} was set to 500 $\mu\text{l hr}^{-1}$ to match the drop throughput of the SAM device in Tao *et. al.* [44]. To minimize the consumption of the fluorinated oil and surfactant, $Q_{spacer-oil}$ was also set to 500 $\mu\text{l hr}^{-1}$. Since Tao *et. al.* set their $Q_{spacer-oil}$ to 4,000 $\mu\text{l hr}^{-1}$, we also tested higher $Q_{spacer-oil}$ flow rates, 1,000 and 2,000 $\mu\text{l hr}^{-1}$. $Q_{spacer-oil}$ was limited to 2,000 $\mu\text{l hr}^{-1}$ as higher $Q_{spacer-oil}$ flow rates did not increase merging efficiencies. Instead of increasing $Q_{spacer-oil}$ beyond 2,000 $\mu\text{l hr}^{-1}$, larger drop spacing could be achieved more easily by decreasing Q_{drops} to 250 and 125 $\mu\text{l hr}^{-1}$ with the $Q_{spacer-oil}$ set to 500, 1,000, and 2,000 $\mu\text{l hr}^{-1}$.

When determining the Q_{drops} and $Q_{spacer-oil}$ values that lead to one-to-one merging, Q_{oil} was set to the same value as Q_{drops} to limit the combinations of solutions, and keeping them identical also helped achieve one-to-one merging. The ratio $Q_{aqueous} / Q_{oil}$ was kept constant within each device geometry; 0.4 for the *Large Split*, 0.2 for the *Medium Split*, and 0.1 for the *Small Split*. These $Q_{aqueous} / Q_{oil}$ ratios were chosen as starting points when optimizing the flow rates to once again reduce the number of flow rate combinations. If a base value of $500 \mu\text{l hr}^{-1}$ for Q_{drops} was sufficient for optimal one-to-one merging, then the lowest value of $Q_{spacer-oil}$ with that base value was used in subsequent experiments, and no further optimization was performed, as indicated by “--” in Table 5. The merging efficiencies (η_{merge}) for the three drop sizes and the three SAM device geometries are listed in Table 5, along with the flow rates used to generate those efficiencies.

Table 5. Flow rates needed to achieve optimal merging for each geometry and drop size

Geometry	Q_{drops} ($\mu\text{l hr}^{-1}$)	$Q_{spacer-oil}$ ($\mu\text{l hr}^{-1}$)	Q_{oil} ($\mu\text{l hr}^{-1}$)	$Q_{aqueous}$ ($\mu\text{l hr}^{-1}$)	η_{merge}		
					Drop Size		
					<i>Large Drops</i>	<i>Medium Drops</i>	<i>Small Drops</i>
<i>Large Split</i>	500	500	500	200	1.00 [§]	1.35 [*]	1.75
		1000			1.00	1.05 [*]	1.67 [*]
		2000			1.00	0.59	0.89
	250	500	250	100	--	1.84 [*]	2.00
		1000			--	1.73	1.58 [*]
		2000			--	0.68 ^{†§}	0.81
	125	500	125	50	--	--	0.53
		1000			--	--	0.92
		2000			--	--	0.76 ^{†§}
<i>Medium Split</i>	500	500	500	100	1.00 [§]	1.00 [§]	0.96 [*]
		1000			1.00	1.00	0.90
		2000			1.00	1.00	1.00 [§]
<i>Small Split</i>	500	500	500	50	1.00 [§]	1.00 [§]	1.00 [‡]
		1000			1.00	1.00	1.00 [§]
		2000			1.00	1.00	1.00

*Predominately two-to-one merging

†Was incomplete merging, and reached 1.00 after $Q_{aqueous}$ was increased

‡Conditions caused two-to-one merging at higher $Q_{aqueous}$ values

§ Q_{drops} and $Q_{spacer-oil}$ flow rates used in later experiments

We observed that the inlet drop length, L_{inlet} (Fig 3), was the primary factor determining the amount of tuning needed for optimal drop merging. *Large drops*, approximately 200 μm long (Table 3), achieved one-to-one merging with the $Q_{drops} = 500 \text{ ul hr}^{-1}$ and $Q_{spacer-oil} = 500 \mu\text{l hr}^{-1}$, and increasing their spacing with larger values of $Q_{spacer-oil}$ did not negatively impact merging efficiencies for all conditions tested. The consistent optimal drop merging for *Large Drops* in all three SAM devices can be seen with merging efficiencies of 1.00 for all tested experimental conditions in Table 5. As the L_{inlet} was decreased to 160 and 130 μm , *Medium Drops* and *Small Drops*, respectively (Table 3), the spacing between the drops had to be increased to achieve optimal merging. The most extreme example of this is observed in the *Large Split* device rows of Table 5.

Medium Drops in the *Large Split* device only achieved optimal merging after Q_{drops} was reduced to $250 \mu\text{l hr}^{-1}$, $Q_{spacer-oil}$ was increased to $2000 \mu\text{l hr}^{-1}$, and $Q_{aqueous}$ had to be increased beyond $50 \mu\text{l hr}^{-1}$ due to incomplete merging at lower flow rates. *Small Drops* in the *Large Split* device only achieved optimal merging after Q_{drops} was reduced to $125 \mu\text{l hr}^{-1}$ and required an increase in $Q_{aqueous}$ due to incomplete merging.

Drop Splitting

Earlier, we hypothesized using equation (11) that the ratio of the drop volumes in the inlet and shunt channels would be proportional to the ratio of flow rates in those channels, where Q_{inlet} and Q_{shunt} are predicted using the device model. To test this hypothesis, drop areas in the inlet and shunt channels (A_{inlet} and A_{shunt}) were measured since drop volumes cannot be directly observed and the DMV software measures drop areas. Rearranging equation (11) and using drop areas instead of drop volumes yields equation (15):

$$\frac{A_{shunt}}{A_{inlet}} \approx \frac{Q_{shunt}}{Q_{inlet}} \quad (15)$$

To examine the relationship in equation (15), the measured drop splitting ratio (A_{shunt} / A_{inlet}) was plotted against the estimated flow rate splitting ratio (Q_{shunt} / Q_{inlet}) (Fig. 7). Equation (15) can be considered empirically correct if there is an approximate one-to-one relationship between the drop and flow rate splitting ratios. Since this relationship is assumed to be approximate, we included a 15% margin of error in the plots of the splitting ratios (Fig. 7(B-D)).

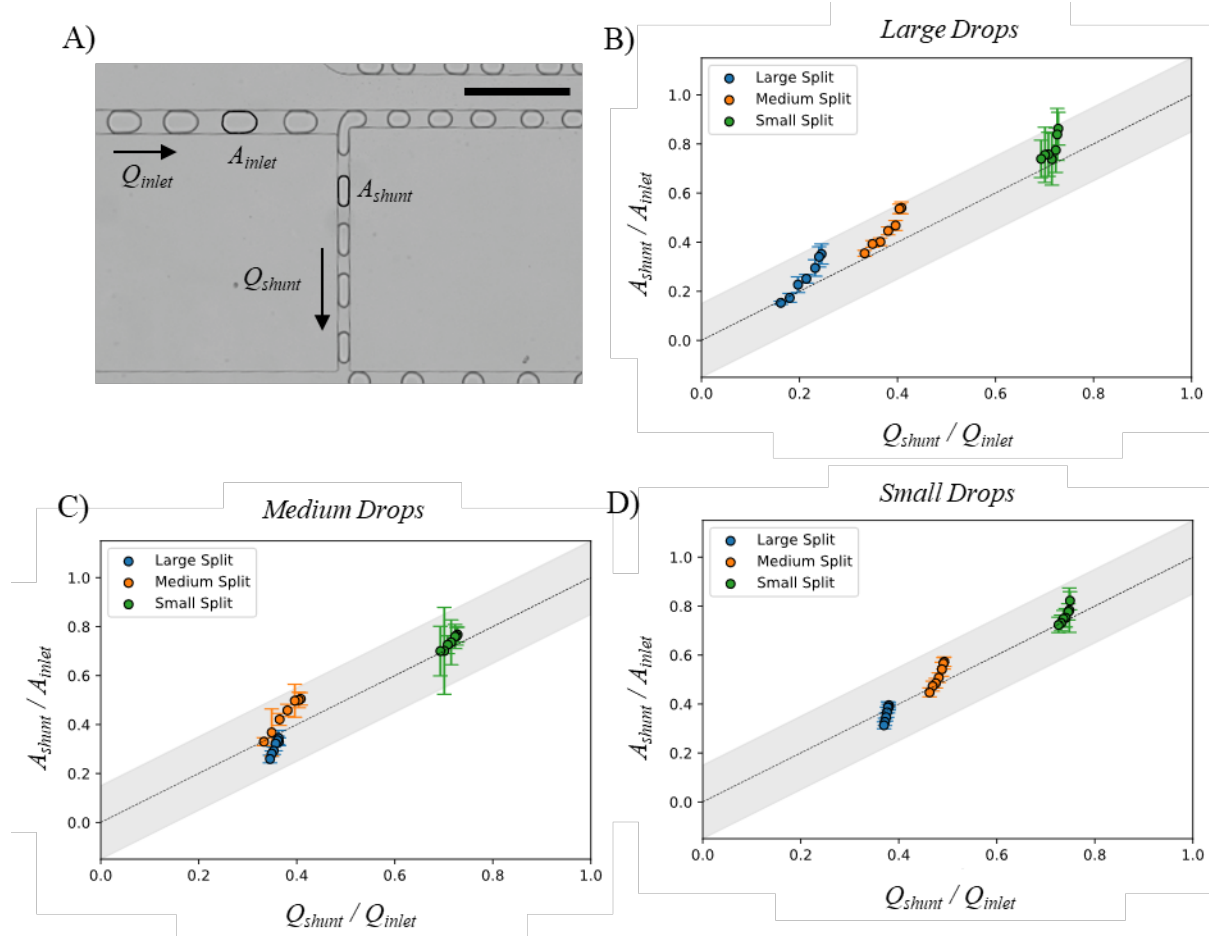


Figure 7. The relationship between drop splitting ratio and flow rate splitting ratio. A) Representative image of the splitting junction illustrating A_{shunt} , A_{inlet} , Q_{shunt} , and Q_{inlet} . Scale bar = 500 μm . B) Drop and flow rate splitting ratios for *Large Drops* in the three SAM devices. C) Drop and flow rate splitting ratios for *Medium Drops* in the three SAM devices. D) Drop and flow rate splitting ratios for the *Small Drops* in the three SAM devices. All plots include a one-to-one line represented by “--” and a 15% margin of error shown in grey.

The relationships between the drop splitting ratios and the flow rate splitting ratios were grouped by inlet drop size (Fig. 7). Within each device grouping, there are several points corresponding to different $Q_{aqueous}$ and Q_{oil} flow rates, while Q_{drops} and $Q_{spacer-oil}$ flow rates were held constant. The positioning of these groupings was influenced by the device geometry and the flow rates both upstream (Q_{inlet}) and downstream (Q_{oil} and $Q_{aqueous}$) of the shunt channel. The *Large Drops* served as a good control since the Q_{drops} and $Q_{spacer-oil}$ flow rates as well as the range of Q_{oil}

and $Q_{aqueous}$ flow rates, were consistent across the three devices (Table 6). This resulted in three distinct groupings of splitting ratios (Fig. 7(B)), and the splitting ratios aligned well with the Q_{shunt} / Q_{inlet} values predicted by the device model (Table 4).

For the *Medium Drops*, the positions of the splitting groupings slightly overlap (Fig. 7(C)). The *Medium* and *Small Split* groupings for the *Medium Drops* occupied the same positions as those devices for the *Large Drops* since the upstream and downstream flow rates were the same for both drop sizes (Table 6). However, there was a significant shift in the groupings in the *Large Split* devices between the *Medium* and *Large Drops*. This shift, indicating a larger split ratio between different drops in the same device, is most likely due to the smaller flow rates downstream of the shunt channel.

To examine how Q_{shunt} is affected by Q_{inlet} , $Q_{aqueous}$, and Q_{oil} equations (4-7) are rearranged, ignoring R_{tuning} for simplicity, to give equation (16). As Q_{inlet} is increases with a decrease in $Q_{aqueous}$ and Q_{oil} , the bracketed term in equation (16), Q_{shunt} , subsequently increases.

$$Q_{shunt} = \frac{Q_{inlet}R_{split} - [Q_{aqueous}R_{merge} + Q_{oil}(R_{merge} + R_{pre-merge})]}{R_{merge} + R_{pre-merge} + R_{shunt} + R_{split}} \quad (16)$$

The *Small Drops* splitting groupings were also distinct from each other (Fig. 7(D)). This distinction arises from the different flow rates upstream and downstream of the shunt channel for each device (Table 6). The utilization of different flow rates for the *Small Drops* leads to the *Large Split* grouping being more similar to the *Medium Drops* in the same device. Furthermore, there was an increase in the split ratio for the *Small Drops* in the *Medium Split* compared to the other two drop sizes, while no significant shift was observed in the *Small Split* between the three drop sizes.

Table 6. Q_{inlet} and range of Q_{oil} and $Q_{aqueous}$ flow rates used in splitting and merging experiments

Geometry	<i>Large</i>			<i>Medium</i>			<i>Small</i>		
Drops	<i>Large</i>	<i>Medium</i>	<i>Small</i>	<i>Large</i>	<i>Medium</i>	<i>Small</i>	<i>Large</i>	<i>Medium</i>	<i>Small</i>
Q_{inlet} ($\mu\text{l hr}^{-1}$)	1000	2250	2125	1000	1000	2500	1000	1000	1500
$[Q_{oil} + Q_{aqueous}]$ ($\mu\text{l hr}^{-1}$)	[525, 1000]	[263, 500]	[131, 250]	[525, 1000]	[525, 1000]	[525, 1000]	[525, 1000]	[525, 1000]	[525, 1000]

The plots of the splitting ratios (Fig. 7(A-D)) demonstrate that A_{shunt} can be approximated from A_{inlet} and the estimated ratio of Q_{shunt} and Q_{inlet} . However, there are still some errors associated with this approximation, as indicated by deviations from the one-to-one line and the data points. Two types of error can be observed: positive error, primarily seen in most of the *Large Drops* groupings, and negative error, observed in the *Large Split* groups for both the *Medium* and *Small Drops*.

The positive error, where the observed splitting ratio is greater than the predicted splitting ratio, is likely due to the added resistances of the drops. Previous studies have shown that slug drops travelling in rectangular channels increase the pressure drop in that section, which is dependent on the number of drops and their combined length [27, 40]. In this study, the *Large Drops* resulted in longer drops in the split, shunt, merge, and pre-merge channels compared to the two other drop sizes. Additionally, a larger number of *Large Drops* were present in all three devices due to the smaller spacing of drops at the inlet. To illustrate the effect of channel resistances on Q_{shunt} , equation (7) is rearranged, ignoring R_{tuning} for simplicity, yielding equation (17). Longer and more drops will increase the values of R_{split} , R_{shunt} , $R_{pre-merge}$, and R_{merge} . Since the split channel is much longer than the shunt channel, the impact of drop resistances is more

significant is the split channel. Consequently, if R_{split} increases more relative to the other resistance values in equation (17), Q_{shunt} should increase, resulting in positive error. This positive error, most likely due to drop resistances in the split channel, can be observed in the *Medium* and *Small Drops* for the *Medium Split*, and the *Small Drops* in the *Small Split*. The *Small Split* devices collectively exhibited positive error due to all drop sizes filling the split channel and consequently increasing R_{split} more relative to the other channel resistances.

$$Q_{shunt} = \frac{Q_{split}R_{split} - Q_{merge}R_{merge} - Q_{pre-merge}R_{pre-merge}}{R_{shunt}} \quad (17)$$

The negative error, where the observed splitting ratio is lower than the predicted splitting ratio, is likely due to drops not completely filling the entire channel. This type of error is only present for both the *Medium* and *Small Drops* in the *Large Split* device. When calculating the channel resistances (Eq. 1), we use the viscosity of water since we are interested in the splitting of the water drops. However, in the *Large Split* device, the *Small* and *Medium Drops* do not fully occupy the pre-merge and split channels, and there is at most one drop in the shunt channel. Therefore, in the split, pre-merge, and shunt channels, the resistance is most likely due to the oil phase, which would increase the values of R_{split} , $R_{pre-merge}$, and R_{shunt} . Referring back to equation (16), an increase in these resistances, all present in the denominator, would decrease the value of Q_{shunt} , resulting in a negative error.

Drop Merging

As described in equation (12), the volume of the drop formed at the merging junction is directly proportional to the ratio between the aqueous and oil flow rates, $Q_{aqueous} / Q_{oil}$. To quantify this generated drop volume, we measure the difference in drop areas before and after the merging

junction, $A_{pre-merge}$ and A_{merge} (Fig. 8(A)). Since the flow rate ratio is dimensionless and equation (15) is a function of the inlet drop area, we normalized the generated drop area by A_{inlet} . Subsequently, we plotted this normalized generated area against $Q_{aqueous} / Q_{oil}$ to determine the scalar multiplier, α , in equation (12).

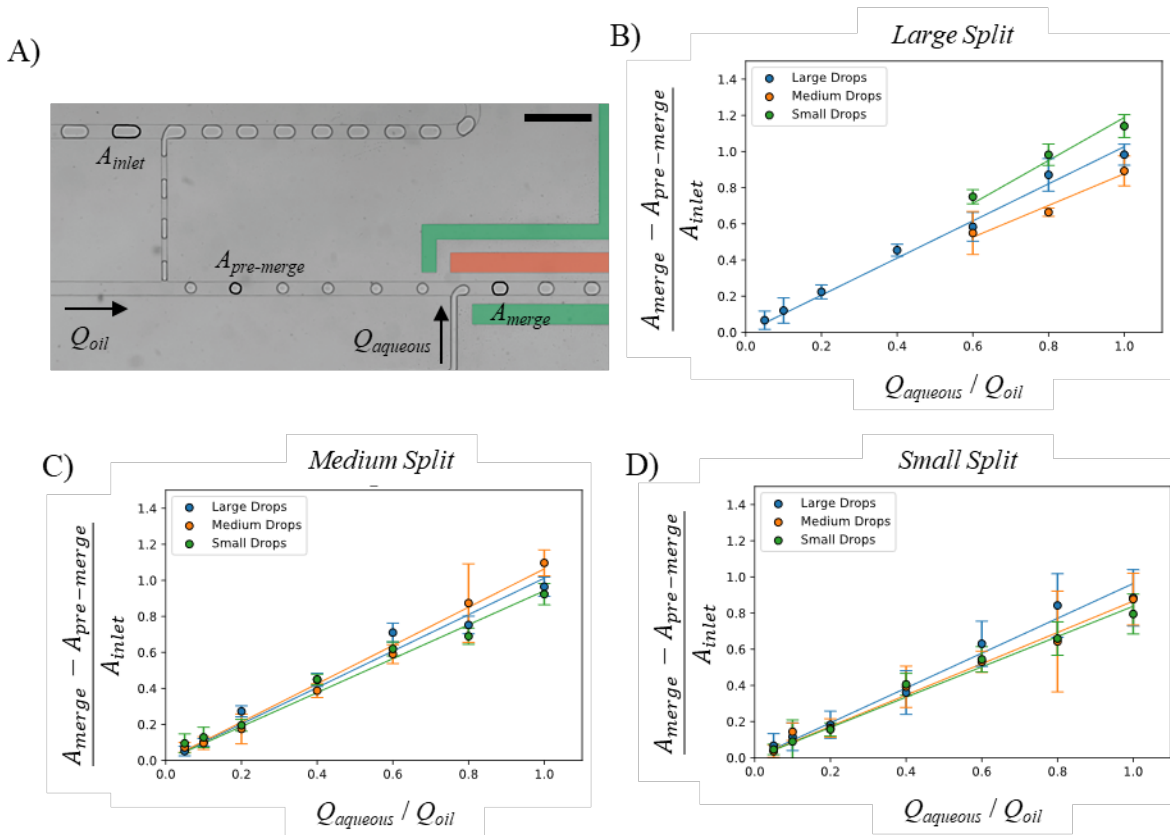


Figure 8. Drop area increases scale linearly with the aqueous and oil flow rates at the merging junction. A) Device image highlighting the drop areas at the inlet, pre-merge channels, along with the aqueous and oil flow rates. The false-colored electrodes are also shown. Scale bar = 500 μm . B) Drop area increases for the *Large Split* devices across the three drop tested sizes. C) Drop area increases for the *Medium Split* devices across the three drop tested sizes. D) Drop area increases for the *Small Split* devices for the three tested drop sizes.

We plotted the drop area increases at the merge junction with respect to the ratio of $Q_{aqueous}$ and Q_{oil} (Fig. 8). The inlet drop sizes were grouped by the device geometry (Fig. 8(B-D)). All device geometries and inlet drop sizes had clear linear relationships matching Equation (18). For

the *Large Split* devices, only the upper range of $Q_{aqueous}$ and Q_{oil} is shown for the *Medium* and *Small Drops*. This is due to incomplete merging and two-to-one merging occurring at lower $Q_{aqueous}$ values and therefore skewing the fit of equation (18).

After plotting the normalized increase in drop area at the merging junction as a function of the aqueous and oil flow rates, we observed a linear relationship with a zero intercept. This relationship is represented by equation (18) where C_0 is the scalar multiplier similar to α in equation (12) and is empirically determined for all T-junction geometries. The lack of an intercept for equation (18) is not surprising when rearranged to equation (19), where $Q_{aqueous}$ is set to zero, indicating no merging. In the absence of merging, A_{merge} is equal to $A_{pre-merge}$.

$$\frac{A_{merge} - A_{pre-merge}}{A_{inlet}} = C_0 \left(\frac{Q_{aqueous}}{Q_{oil}} \right) \quad (18)$$

$$A_{merge} - A_{pre-merge} = C_0 \left(\frac{Q_{aqueous}}{Q_{oil}} \right) A_{inlet} \quad (19)$$

After conducting linear regression on the plots of equation (18) for all three drop sizes in the three device geometries, we obtained values for C_0 (Table 7). The value for C_0 was found to be approximately 1 for all geometries and drop sizes (Table 7). It is believed that C_0 's value is dependent upon the geometry of the merging junction [21] and might differ if the width of both the aqueous and merge channels are changed.

TABLE 7. Values for the constant in equation (18)

Constant	Drop Size	Geometry		
		<i>Large Split</i>	<i>Medium Split</i>	<i>Small Split</i>
C_0	<i>Large Drops</i>	1.03	1.01	0.96
	<i>Medium Drops</i>	0.88	1.06	0.87
	<i>Small Drops</i>	1.19	0.94	0.84

Drop Splitting and Merging

For this next section, we aimed to determine if A_{merge} can be empirically predicted solely from A_{inlet} and the ratio of $Q_{aqueous}$ and Q_{oil} (Fig. 9(A)). To achieve this, we plotted the percent change of the drop before and after the merge junction, $[(A_{merge} - A_{inlet}) / A_{inlet}]$, as a linear function with respect to the ratio of $Q_{aqueous}$ and Q_{oil} (Eq. 20). This relationship is valuable for cases where users are unable to measure drop dimensions on the device or are primarily interested in confirming the shift in drop area during repeated SAM operations.

$$\frac{A_{merge} - A_{inlet}}{A_{inlet}} = C_1 \left(\frac{Q_{aqueous}}{Q_{oil}} \right) + D_0 \quad (20)$$

A plot of Equation (20) was generated for the three inlet drop sizes grouped by device geometry (Fig. 9(B-D)). Similar to Figure 8, a clear linear relationship was observed when equation (20) was plotted. Additionally, as seen in Figure 8, the *Medium* and *Small Drops* in the *Large Split* device were limited to the higher end of $Q_{aqueous} / Q_{oil}$ due to incomplete merging at those lower flow rates.

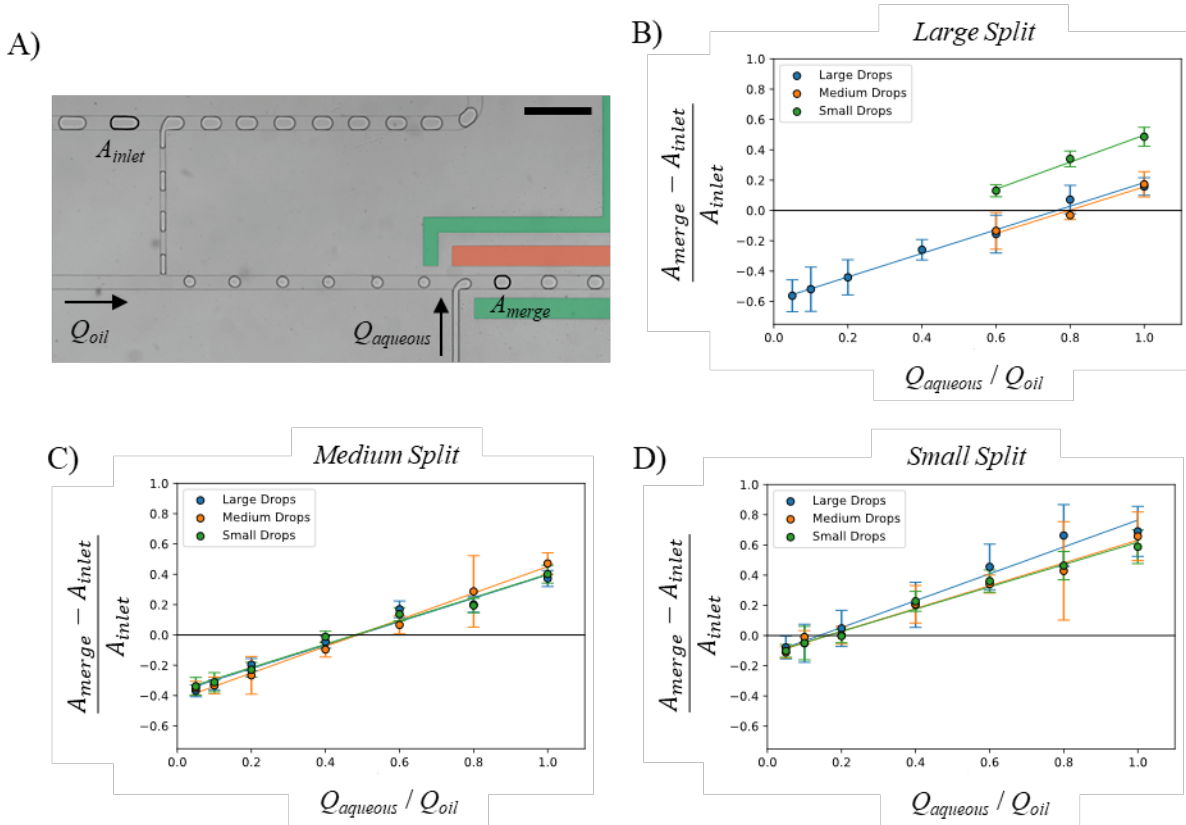


Figure 9. Percent change of drops entering the SAM devices and leaving the merge junction scales linearly with the aqueous and oil flow rates at the merging junction. A) Device image highlighting the drop areas at the inlet and merge channels, along with the aqueous and oil flow rates. The false-colored electrodes are also shown. Scale bar = 500 μm . B) Drop area increases for the *Large Split* devices across the three drop tested sizes. C) Drop area increases for the *Medium Split* devices across the three drop tested sizes. D) Drop area increases for the *Small Split* devices for the three tested drop sizes.

After performing linear regression on the plots of equation (20) for all three drop sizes in the three device geometries, we obtained the values for C_1 and D_0 (Table 8). Similar to C_0 in equation (19), the value of C_1 was found to be approximately the same across all drop sizes and device geometries, reflecting the geometry of the merge junction. In contrast to equation (19), equation (20) has a non-zero intercept that represents the droplet splitting ratio across the range of $Q_{aqueous} / Q_{oil}$ plotted (Table 8). The y-intercept of the plots in Figure 9(B-D) is also useful for future users as it provides the ratio of $Q_{aqueous}$ and Q_{oil} at which A_{merge} is equal to A_{inlet} based on the

values of C_1 and D_0 . To solve for the y-intercept, the left-hand side of equation (20) is set to zero and $Q_{aqueous} / Q_{oil}$ is solved for (Eq. 21). The values for the y-intercepts are also listed in Table 8.

$$\left(\frac{Q_{aqueous}}{Q_{oil}}\right)_{A_{merge}=A_{inlet}} = -D_0 / C_1 \quad (21)$$

TABLE 8. Values for the constants in equation (20)

Constant	Drop Size	Geometry		
		<i>Large Split</i>	<i>Medium Split</i>	<i>Small Split</i>
C_1	<i>Large Drops</i>	0.78	0.77	0.89
	<i>Medium Drops</i>	0.77	0.88	0.75
	<i>Small Drops</i>	0.89	0.77	0.74
D_0	<i>Large Drops</i>	-0.59	-0.38	-0.12
	<i>Medium Drops</i>	-0.61	-0.43	-0.12
	<i>Small Drops</i>	-0.39	-0.37	-0.12
$-D_0 / C_1$	<i>Large Drops</i>	0.76	0.49	0.13
	<i>Medium Drops</i>	0.79	0.49	0.16
	<i>Small Drops</i>	0.44	0.48	0.16

Empirical Drop Models of SAM Devices

The plots of the drop areas at the splitting and merging junction can be combined and compared to the drop model derived earlier (Eq. 13). Equation (19) is first re-written with A_{merge} on the left-hand side, giving equation (21). Similar to equation (10), $A_{pre-merge} = A_{shunt}$, and the expression for A_{shunt} can be found from equation (15), leading to equation (22). Substituting equation (22) into (21) gives equation (23) and changes the equal sign in equation in (21) to an approximate sign. Finally, A_{inlet} can be factored out of equation (23), resulting in equation (24).

$$A_{merge} = C_0 \left(\frac{Q_{aqueous}}{Q_{oil}}\right) A_{inlet} + A_{pre-merge} \quad (22)$$

$$A_{pre-merge} = A_{shunt} \approx A_{inlet} \left(\frac{Q_{shunt}}{Q_{inlet}}\right) \quad (23)$$

$$A_{merge} \approx C_0 \left(\frac{Q_{aqueous}}{Q_{oil}} \right) A_{inlet} + A_{inlet} \left(\frac{Q_{shunt}}{Q_{inlet}} \right) \quad (24)$$

$$A_{merge} \approx A_{inlet} \left[C_0 \left(\frac{Q_{aqueous}}{Q_{oil}} \right) + \left(\frac{Q_{shunt}}{Q_{inlet}} \right) \right] \quad (25)$$

Equation (25) exhibits a similar form when compared to the derived drop model in equation (13). However, in equation (25), since all drop changes were normalized to A_{inlet} , it appears outside of the brackets on the right-hand side. instead of being only present in the splitting term of equation (13). There is still a constant term next to the ratio of $Q_{aqueous}$ and Q_{oil} , which aligns with the scaling laws of drop production of T-junctions (Eq. 12). However, unlike equation (13), equation (25) includes a non-zero intercept when drops are produced.

Equation (25) can be combined with the device model, equations (3-9), to design future SAM devices. The device model serves as the foundation for the design and is used to ensure that the channels do not experience any backflow, which is particularly concerning in the shunt channel. Users can then use equation (25) to estimate the drop splitting ratio. The values C_0 still need to be determined empirically, but this can be easily accomplished through droplet experiments. Equipped with equations (13) and (25), SAM devices with different splitting ratios can be designed to produce merged drops of different sizes.

As mentioned earlier, there are cases where there is no need to measure drop dimensions on SAM devices, and the primary concern is that drops exiting the merge junction have a specific size. In such instances, we have developed a more empirical model (Eq. 20). To equation (20) more useful, it is rearranged so A_{merge} is expressed as a function of A_{inlet} , $Q_{aqueous}$, and Q_{oil} (Eq. 26). Equation (26) has the same structure as equation (25). except it lacks the splitting term. Instead, there is an intercept, $1 - D_0$. The only limitation of equation (26) is that the constants need

to be determined experimentally. Therefore, equation (26) can only be used if users have a SAM device that has been verified to work with specific flow rates.

$$A_{merge} = A_{inlet} \left[C_1 \left(\frac{Q_{aqueous}}{Q_{oil}} \right) + 1 - D_0 \right] \quad (26)$$

Conclusion

In summary, we presented a process to design drop-based split-and-merge (SAM) microfluidic devices and empirical models to predict drop volume changes within the devices. We used the electric circuit analogy to design three SAM devices with different splitting ratios and optimized the merging efficiencies of those three devices with three different input drop sizes. We found four different merging regimes and that the optimal regime for us, one-to-one merging, depends on the inlet drop spacing and inlet drop length. We derived a theoretical model to predict drop volume changes based on the mass balance of drops in SAM devices and found two empirical models that are in good agreement with the derived equation. One empirical model can be used in tandem with the device model to predict outlet drop sizes and only has one nondimensional constant that needs to be solved empirically. The other empirical model is easier to use as it does not require high-speed imaging to verify its validity, but it has two nondimensional constants to solve for, and is independent of the device model.

The SAM devices presented in this paper were able to split incoming mother drops into different daughter drop volumes and then generate drops of various sizes at the merge junctions. The observed drop split ratios agree well with the predicted flow rate split ratio. However, there were observed deviations from the predicted split ratios most likely due drop resistances in the channels downstream of the splitting junction. This drop resistance could be mitigated with wider

channels downstream of the split junction, this would increase the device footprint as wider channels would need to be longer to achieve the same splitting ratio. The drop resistances could also be accounted for on the modelling side with another linear solver that solves for the drop resistance and then using an iterative approach to solve for the device flow rates based on the channel and drop resistances. Accounting for drop resistance would require additional experiments to determine nondimensional parameters associated with drop resistance [40]. The SAM devices were also able to generate a wide range of drop volumes at the merge junction. Creating a wide variety of drop sizes at the merge gives these SAM devices great flexibility to control the volume of reagents added to the daughter drops.

The work presented here can be used to design future iterations of SAM devices. Firstly, we only tested a narrow range of splitting ratios, and this modelling process could be used to split drops across a wider range by altering both the width and length of the split and shunt channels. Secondly, this understanding could be used to create devices that merge both daughter drops with an additional aqueous stream or have two or more splits in the device. Additionally, since the large drops in the three SAM devices utilized the same flowrates for both oil inlets, future SAM devices could be designed with only one oil inlet to reduce operation complexity. Also, we found that two-to-one merging could be achieved with specific drop sizes and device geometries. Two-to-one merging could have unforeseen applications and future optimization could be designed around that merging regime. Finally, this work was limited to specific channel heights and widths to constrain relatively large drops at the inlet. These models and observations should be tested before using smaller incoming drops.

CHAPTER 5

CONCLUSIONS AND OUTLOOK

Conclusions

The research presented in this thesis contributes to the understanding of optimizing pump systems and microfluidic devices for the creation and manipulation of microfluidic drops. Chapter 3 of this thesis focused on the creation of an open-source pneumatic pressure pump which was then used to create drops. Chapter 4 of this thesis focused on the design, operation, and optimization of a split-and-merge (SAM) drop-based microfluidic device to determine an empirical model that can be used to predict drop volume changes in SAM devices.

In Chapter 3, an open-source pneumatic pressure pump was created that has a rapid response time and accurate pressure regulation. The pump utilizes a dual-valve regulator design with an Arduino microcontroller controlling four pressurized outlets. A guided user interface (GUI) was designed and implemented with Python to allow the user to control the pump via a computer and the control scheme was written in the Arduino integrated development environment (IDE). The pump was found to accurately control pressures with a resolution of less than 0.02 psig with a response time of less than one second, an overshoot of less than 30%, and a settling time of less than two seconds. The pump was then validated in its ability to produce drops in a microfluidic flow-focusing device where the resulting drop size scaled with the applied pressures of the phases. This pump improves upon existing open-source pneumatic pressure pump systems since it utilizes a custom dual-valve design and was used to drive fluid flow in microfluidic devices.

In Chapter 4, we developed a methodology to model and design drop-based SAM microfluidic devices. Our design process utilizes the electric circuit analogy to first create SAM devices with different splitting capabilities. Next, we derived a drop model to predict drop volume changes within SAM devices based on a mass balance of the drops and several scaling laws in literature. We then tested three of these SAM devices with different inlet drop volumes to determine if the derived drop model matches with empirical results. We found that the inlet drop volumes affected the merging efficiencies of all three SAM devices and therefore the inlet drop spacing to achieve one-to-one merging. All three inlet drop sizes and three SAM device geometries were then tested in their ability to form drops of different volumes at the merging junction. The splitting ratios and resulting drop volume changes at the splitting and merging junctions were then measured and two empirical models were found that describe the changes in drop volumes in SAM devices. These two empirical models were found to be in good agreement with the derived drop model. This work is the first to explore the design and implementation of SAM devices from a fundamental perspective, not an applied one, and can be used to design future SAM devices.

Outlook

The two projects presented in this thesis share a common goal of de-mystifying two aspects of drop-based microfluidics; the pump systems used to drive flow and the creation of drop manipulation devices. They achieve this by creating accessible methodologies to create an open-source pump system and an accessible modelling platform to predict drop volume change in drop-based SAM microfluidic devices. Although the overlap of these projects is not

demonstrated in this thesis, I will suggest future overlapping projects and future studies in this section.

The open-source pneumatic pressure pump was not utilized to drive fluid flow in SAM devices for one major reason; the pump drives fluid from the bottom of a sealed container and the drops float on the top of the oil reservoir. Our pump could be adapted to pressurize the oil below the floating drops by connecting the outlet of the sealed vessel to a column of oil and drops. We were utilizing additional silicone tubing to hold the drops and the pump could be used to flow the drops through the column. However, there were material compatibility issues as the silicone tubing, due to its electrostatic charge, would attract dust and coalesce drops in its interior. Future work would focus on optimizing the materials needed to drive drops with a pneumatic pressure pump. An alternative solution would be to adapt a syringe pump system to be controlled via pressure regulation. This would allow us to better model the pressure drop within a SAM device as we would be able to measure the inlet pressure for the pumps.

There are also several future studies that could be performed with the SAM devices with the splitting geometry, the merging junction, and the device model. The splitting junction in the SAM devices utilizes a geometry like the λ -junction discussed in Chapter 1 of this thesis and this geometry has been not been studied as extensively as the T-junction used for splitting drops. One major difference in our splitting junction and the λ -junction was that our splitting junction had a contraction in the main channel, that was used to achieve different splitting ratios. Future work would study different channel widths and lengths and how those channel dimensions effect drop splitting. Fully exploring the effects of channel geometry on drop splitting could provide more insight into the different breakup regimes in our geometry as well as whether the channel

geometry affects the drop splitting ratios. More studies could also be performed with the merging junction of the SAM devices. We were optimizing merging efficiency convoluted with drop splitting and a separate chip could be designed to only merge incoming drops. This merging chip could be used to further study the effects of drop size before the merge and the merging efficiency at our junction. Finally, our SAM model did not account for drop resistance.

Accounting for drop resistance would require us to determine the semiempirical parameters of drop resistance unique to our device dimensions and two-phase composition (Chapter 1). These measurements could be performed with a novel microfluidic device, enhanced with the droplet morphometry and velocimetry (DMV) software (Chapters 1-2), and would prove useful for other groups. Accounting for drop resistance in the device model would require an additional linear solver that predicts the average drop lengths and number of drops in each channel. This solver would then affect the electric circuit analogy model and therefore an iterative model would need to be implemented. Future work should implement a fluid circuit model that incorporates drop resistance.

APPENDIX
MICROFLUIDIC
GUT-ON-A
CHIP

Motivation

The motivation from this work comes from a National Institutes of Health (NIH) grant to further develop organ-on-a-chip platforms. Organs-on-a-chip are a branch of microfluidics that mimics the physical and cellular environment on microfluidic devices [76]. These chips can be used to study drug interactions [87] and pathogen interactions with host cells [88]. This work is centered around an intestinal organ-on-a-chip system or guts-on-a-chip. Guts-on-a-chip are important to develop because the intestinal system is an environment rich with immune, epithelial, and pathogen interactions [75].

The research presented in this appendix is motivated by the efforts to extend the capabilities of a milli-fluidic Gut Organoid Flow Chip (GOFlowChip), that controls the fluid environment surrounding human intestinal and human gastric organoids, HIOs and HGOs respectively [89]. Organoids are an important part of organs-on-a-chip technology as they are primary cells three dimensional structures that recreate the multicellularity of human tissues on a much smaller scale [90]. Organoids also self-organize into three dimensional structures with a similar shape as the tissues they are derived from [91, 92]. The GOFlowChip is used to study the interactions between dendritic cells due to the recruitment of immune cells to these gastric organoids [93]. Immune cells that act as intermediates between the gastric system and the lymph nodes [94]. Work has been done to improve the GOFlowChip's ability to study organoid-immune cell interactions which was focused on improving the hydrogel scaffold that separates the organoids from the immune cells [95, 96]. The author of this thesis has participated in this research as well.

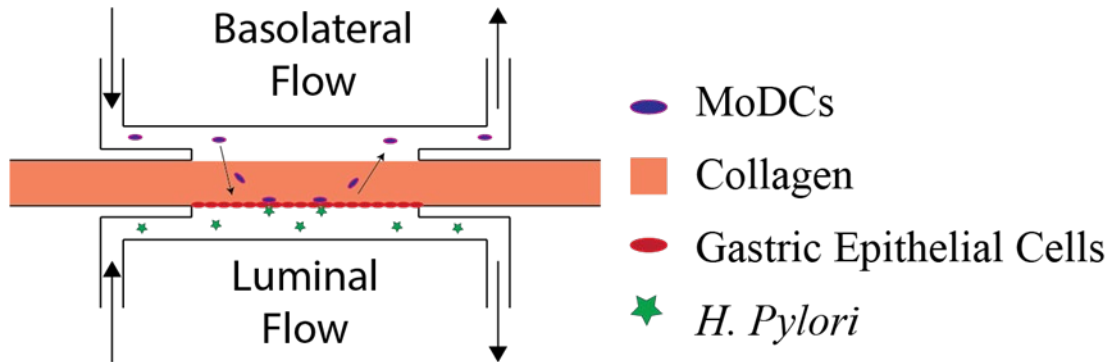


Figure 1. The proposed microfluidic gut-immune-system (μ GIS) chip would allow precise control over the basolateral and luminal compartments of a microfluidic gut-on-a-chip. Monocyte derived dendritic cells (MoDCs) would be cultured in the basolateral chamber, a collagen barrier would separate the two chambers, gastric epithelial cells would be cultured in the luminal chamber with the presence of *H. Pylori* bacterial cells.

The GOFlowChip has been successful in study organoid-immune cell interactions, however is lack the ability to robustly control fluid flow inside the organoid. In the past, flow inside of organoids was accomplished by “porting” the organoids with glass capillary needles. An alternative to this process was proposed by the author of this thesis and centers around developing an entirely different microfluidic system. Shown in figure 1, this new microfluidic device would satisfy the NIH grant’s aim of establishing control over the luminal and extraluminal fluid composition for a gut-on-a-chip system. This microfluidic gut-immune-system (μ GIS) chip is a microfluidic model of the gastric architecture. A wall of a collagen, a hydrogel present in the connective tissues of mammals, functions as a barrier and scaffold separating the basolateral and luminal chambers of the device. The basolateral chamber can contain monocyte-derived dendritic cells (MoDCs) which can be introduced to study their behavior in the device. In the luminal chamber, the collagen functions as a barrier and a scaffold that gastric epithelial cells can adhere to and form a function barrier. The luminal chamber barrier can also contain pathogenic bacteria, such as *H. Pylori*. This μ GIS chip would allow users to study gastric

epithelial physiology, such as barrier formation, immune-epithelial cell interactions across the collagen barrier, the interactions between bacteria and epithelial cells, and the how all three cell types interact.

Laminar Flow Patterning of a Hydrogel Scaffold

The first attempt at fabricating of a μ GIS chip relied on the laminar flow patterning to guide the formation of a collagen barrier. Laminar flow patterning is a technique in microfluidic devices that controls the location of reactive chemical species in a microfluidic device [97]. If the chemical species are pumped into a device fast enough to out compete their diffusive transport, then their location can be controlled [97]. Using laminar flow patterning to create a two-chamber microfluidic device, with a collagen barrier, was performed by Loessber-Zahl *et. al.* and served as the inspiration of this first method to create a μ GIS chip [98].

Method

The laminar flow patterning method relies on creating a hydrophilic path of dilute collagen in a microfluidic device so a concentrated solution can be added to the device and stays along that path. Surface treatment of the microfluidic channels is first performed to create this hydrophilic path. Polydimethylsiloxane (PDMS) channels are made via soft lithography and bonded to glass with oxygen plasma. After bonding, a 3% v/v solution of (3-Aminopropyl) triethoxysilane (APTES) is added to device and rinsed. This silane has a primary amine group that modifies the surface of the entire microfluidic device to mostly have exposed primary amine groups. After APTES is deposited, a 10% v/v solution of glutaraldehyde (GA) is added and rinsed. The two aldehyde groups on GA can react with any primary amine. GA reacts with the APTES amine groups and is still available to react with the amine groups on collagen. After the

surface of the microfluidic devices have been treated and left to dry overnight, a dilute solution of collagen is patterned. In the two side channels of the device, a solution of 1X phosphate-buffered saline (PBS) solution is pumped at $1000 \mu\text{l hr}^{-1}$ with syringe pumps. In the center channel, a $10 \mu\text{g ml}^{-1}$ solution is pumped at $500 \mu\text{l hr}^{-1}$ with syringe pumps. These flowrates were found to be able to create a laminar flow path of collagen based on the simulations below. Flow was maintained for ten minutes and the devices were immediately dried and then further dried overnight. Then the actual collagen barrier was pipetted into the device. A 4 mg ml^{-1} solution of collagen at pH 7 was added to the center device entrance and left to cure for two hours at 37°C . The center entrances of the device were then sealed with sealed pieces of polyethylene tubing. Cell media was added to the devices via the two side entrances and allowed to sit overnight. Human alveolar epithelial cells (A549) cells were then pipetted into the device at a concentration of $2 \times 10^6 \text{ Cells ml}^{-1}$. After the cells were added to the device, the devices were tilted to the side at 90° to allow the cells to adhere to the collagen. The devices were then perfused with media at $10 \mu\text{l hr}^{-1}$.

Simulations

To determine which flowrates would provide result in an even pattern of dilute collagen, COMSOL Multiphysics software was used to simulate the patterning process. The flowrates were first calculated using the Péclet number, which is ratio of advective and diffusive transport. These simulations reinforced the flowrates found using the Péclet number. The simulations were setup to mimic the patterning process described above. The same two-dimensional drawing used to fabricate the devices was used as the simulation geometry. The simulation environment was

setup to model both laminar fluid flow and dilute species diffusion. The diffusion coefficient of the collagen monomers was estimated using the molecular weight of native collagen fibers [99].

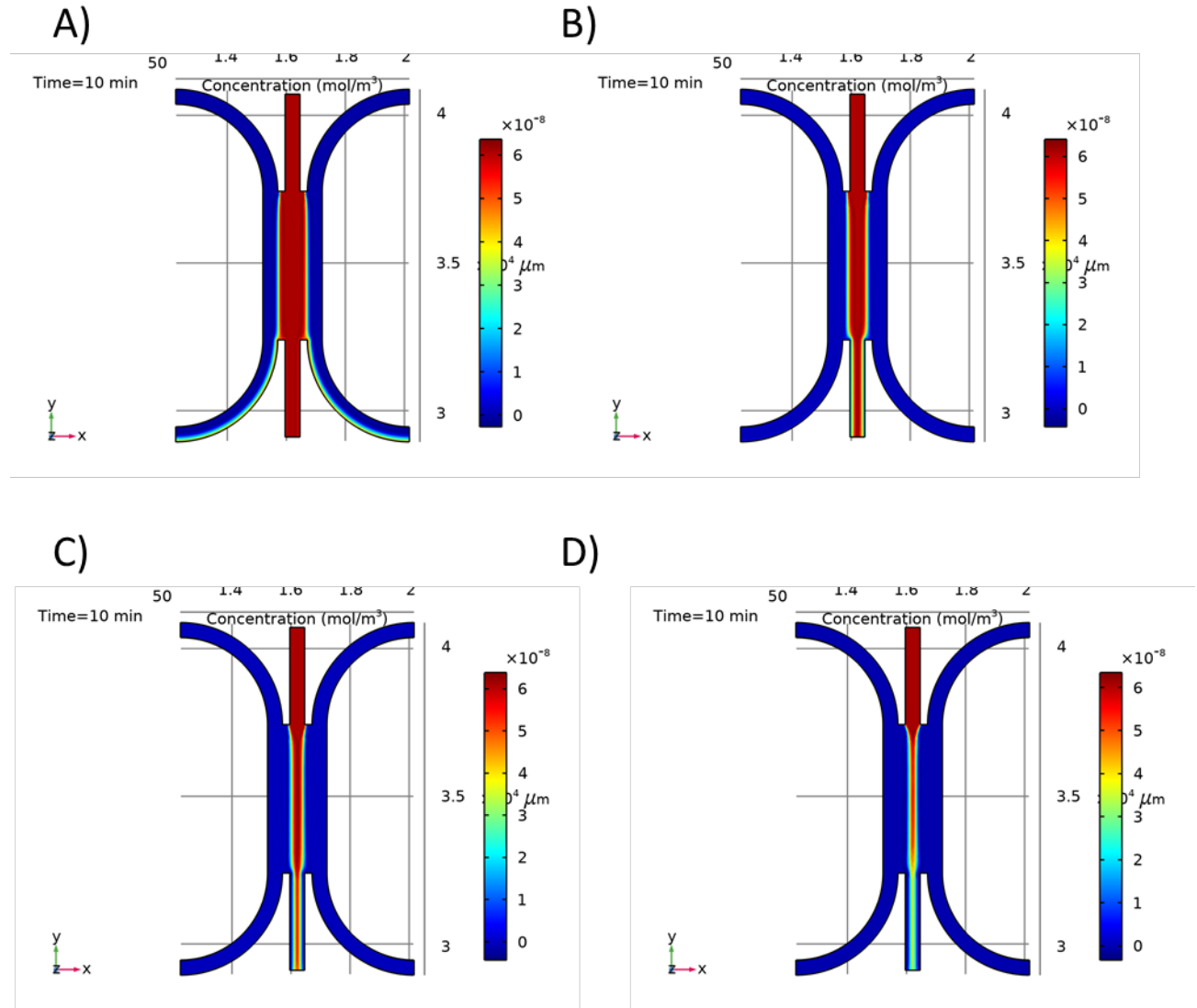


Figure 2. COMSOL Multiphysics simulations show which flowrates can be used to create patterned collagen paths with different widths. The heatmap shows the concentration of the dilute solution of collagen. The center channel had a constant flowrate of $500 \mu\text{l hr}^{-1}$. A) A patterned collagen path with the side channels flowing at $250 \mu\text{l hr}^{-1}$. B) A patterned collagen path with the side channels flowing at $500 \mu\text{l hr}^{-1}$. C) A patterned collagen path with the side channels flowing at $1000 \mu\text{l hr}^{-1}$. D) A patterned collagen path with the side channels flowing at $2000 \mu\text{l hr}^{-1}$.

The COMSOL Multiphysics simulations of the patterning process illustrated that the collagen thickness could be controlled via the flowrates used in the two side channels and a minimum of $500 \mu\text{l hr}^{-1}$ was necessary to keep the collagen confined in the center area of the device. Figure 2 shows the simulation results with a constant center flowrate of $500 \mu\text{l hr}^{-1}$ with the increasing side channel flowrates of 250, 500, 1000, and 2000 $\mu\text{l hr}^{-1}$ for 2A), 2B), 2C), and 2D) respectively. As the side channel flowrates were increased, the area that the dilute solution of collagen occupied decreased as expected.

Results

The μGIS chips fabricated with laminar flow patterning were then assessed in their ability to form a diffusional barrier as a function of the collagen density. A solution of 10 kDa FITC-Dextran was pumped onto the device on one side and then flow was shutoff. Then the FITC fluorescent intensity was imaged for the entire device over the course of 30 minutes. This was performed with collagen at 4 mg ml^{-1} and 2 mg ml^{-1} . Figure 3A) shows the results of this functional barrier test with a plot of FITC intensity over the lateral distance of the device at specific time points. The collagen and side channel areas highlighted in the device. At time zero, there is a small FITC signal in the collagen barrier which increased over time. Figure 3B) shows the device during the timepoints plotted in figure 3A). Figure 4A) shows the same barrier test with a collagen barrier at 2 mg ml^{-1} . Once again, at time zero there is a small FITC signal in barrier. However, after 10 minutes the FITC-Dextran has diffused across the barrier and after 30 minutes, the FITC-Dextran has the same signal across the entire device. It was decided that the 2 mg ml^{-1} was too porous to function as diffusional barrier and future cell studies were used with

collagen at a concentration at 4 mg ml^{-1} . It was also noted, that the collagen barrier was not uniform throughout the main area of the μGIS devices.

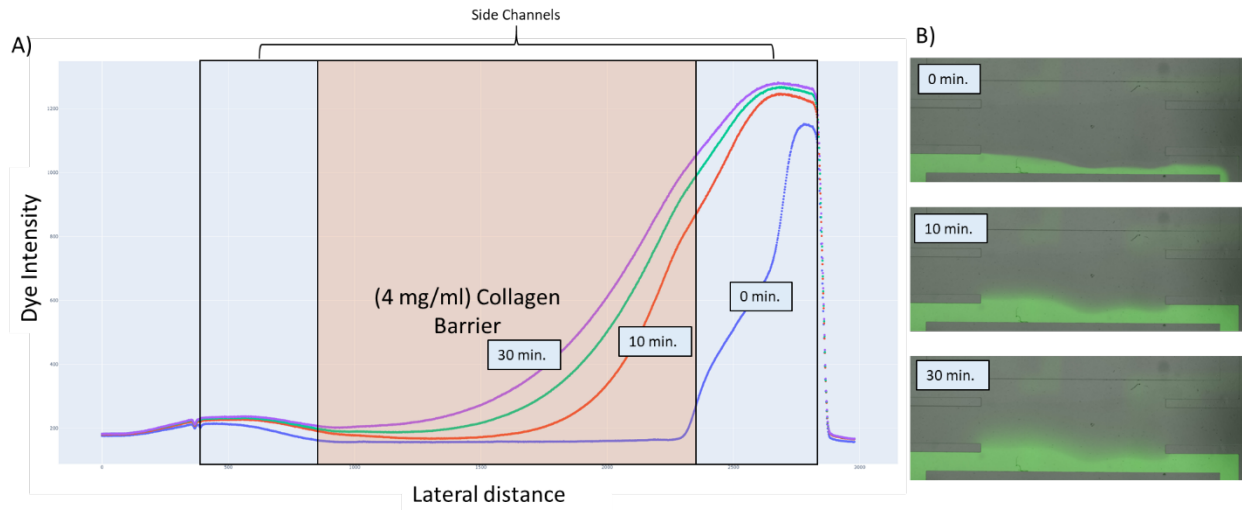


Figure 3. A 4 mg ml^{-1} collagen barrier serves as an adequate diffusional barrier for the μGIS chip. A) A plot of FITC intensity over lateral distance at different timepoints. The barrier area and side channels are highlighted in the plot area. B) Represent images of the device at the timepoints of interest.

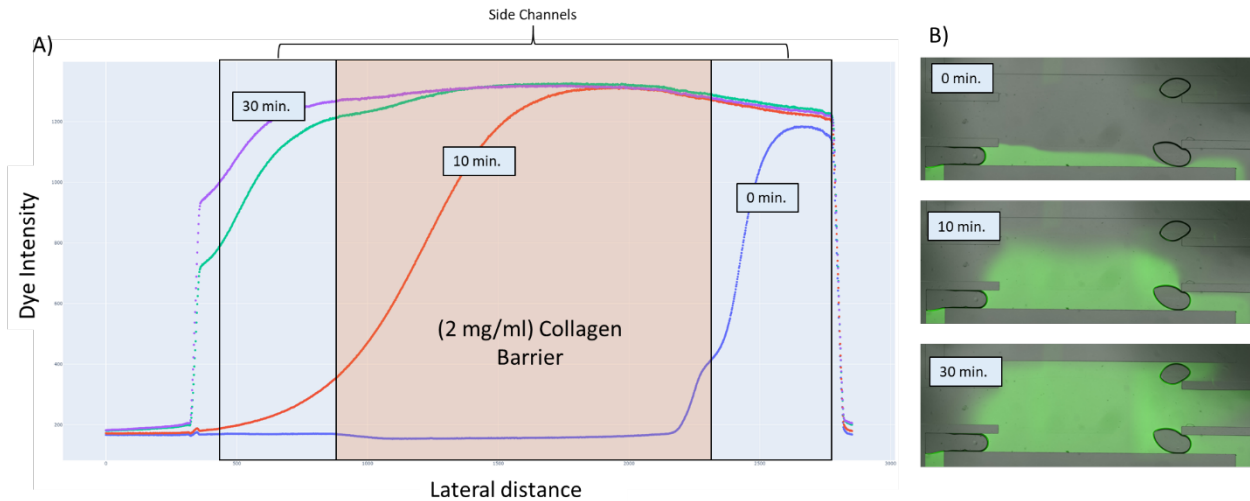
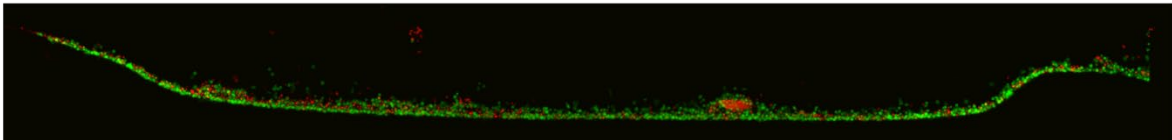


Figure 4. A 2 mg ml^{-1} collagen barrier serves as an adequate diffusional barrier for the μGIS chip. A) A plot of FITC intensity over lateral distance at different timepoints. The barrier area and side channels are highlighted in the plot area. B) Represent images of the device at the timepoints of interest.

Then the μ GIS chip fabricated with laminar flow patterning was tested in its ability to serve as an epithelial cell scaffold. A549 cells were used for studies, despite being human alveolar epithelial cells because they were already being cultured in the lab. After seeding the cells onto the device, they were perfused for 24 hours with media. Then live, dead, and DAPI stains were added to assess cell viability and distribution. After 24 hours, there were both dead and live cells found. However, the biggest find for these results was that the distribution of cells was uneven. This uneven cell seeding is most likely due to the uneven collagen barrier.

A) **Live/Dead Stain Overlay**



B) **Live/Dead and DAPI Stain Overlay**



Figure 5. Represent images of epithelial cells live, dead, and DAPI stained in the μ GIS device show that cell seeding was not uniform. A) A549 cells were live and dead stained in the μ GIS device. A) A549 cells were live, dead, and DAPI stained in the μ GIS device.

Conclusions

The μ GIS chip was switched to another type of microfluidic device after these were found for several reasons. The main reason was that a commercial and more user-friendly chip was found. The μ GIS chip made with PDMS was found to be extremely delicate and difficult to pipette into. The uneven collagen distribution was most likely due to slight changes in the devices height during fabrication via soft lithography and could be easily rectified if they were

fabricated at the Montana Microfabrication Facility (MMF) at Montana State University (MSU) (Montana, USA).

Utilizing a Pinned Hydrogel Scaffold

The next iteration of the μ GIS chip utilized a commercial microfluidic device. This next section uses the idenTx chip from AIM Biotech to create a gut-on-a-chip. The idenTx chip has the same general architecture shown in figure 1, with a center area to house a collagen barrier and two side channels. The main difference, is that the idenTx chip is fabricated from cyclic olefin copolymer (COC) and uses pillars made of COC to trap the collagen barrier. There are two rows of pillars separating the center channel from the two side channels. These pillars trap hydrogels that are added to the device if their surfaces are hydrophilic [100], which COC is. This device geometry has been used for several organ-on-a-chip applications where a barrier between cell types was needed, such as creating a microfluidic blood-brain barrier [101] and a tumor-endothelium barrier [102].

Method

The vendor of the idenTx chips, AIM Biotech, provided the protocols for loading the collagen barrier, seeding cells, and testing the barrier's permeability. Therefore, the author of this thesis will only briefly describe these processes. To load the collagen barrier, it is simply pipetted into the center chamber of the device and allowed to cure for 30 minutes at 37 °C. Then the side channels are coated with a 50 $\mu\text{g ml}^{-1}$ solution of fibronectin to promote cell adhesion to all COC surfaces of the device. The fibronectin solution can sit for 15 minutes and the device is rinsed with media.

Human colorectal adenocarcinoma (Caco2) cells are used to seed the idenTx chips and were cultured by the author of this thesis. To seed the cells, a solution of 2×10^6 C ml⁻¹ were added to both inlets of one side of the device, flipped 180°, and were undisturbed in an incubator for 30 minutes at 37 °C. The idenTx chip has built in media reservoirs above the device inlets designed to hold approximately 100 µl of liquid. After cell seeding, the media was exchanged in each reservoir every 24 hours.

To test the permeability of cell barrier, a procedure like the one described in the previous device was used. A solution of 10 kDa FITC-Dextran in media was added to the cell side of the device with the other side containing media. The solution was equilibrated for 2 minutes, and then the entire device was imaged using epi-fluorescent microscopy for 30 minutes every 5 minutes.

Optimizing the Collagen Formulation

The first task for optimizing the idenTx for the µGIS system was to optimize the collagen formulation used to create the barrier. The concentration of collagen fibers used to form the barrier affects the fiber density in the cured gel and therefore affects the ability of small molecules and cells to diffuse and travel inside it [103-105]. The more concentrated the collagen solution, the less permeable the gel becomes. The pH that the collagen solution is cured in also affects the porosity of the collagen barrier [104, 106] and has been shown to affect the ability of human cells to travel inside the gel [107, 108]. Between pH 5 and 11, the more acidic the collagen solution is, the less dense the fiber is and is more permeable.

First, the ability of DCs to travel through different collagen formulations was tested, figure 6. Different collagen solutions were created with concentrations of 0.75, 1.5, and 3.0 mg

ml⁻¹. Each of these concentrations was then crosslinked in solutions whose pH was 5, 7, and 9. Each collagen formulation was added to the bottom of a trans-well with DCs at the top and a chemoattractant in the bottom well. The DCs were incubated overnight and allowed to cross the collagen barrier. The cells were then stained to emit luminescence to measure the approximate number of cells that crossed the collagen barrier figure 6A. As was expected, as the pH increased the number of cells to cross the collagen barrier. It was also generally found that as the collagen concentration increased, the number of cells to cross the barrier decreased.

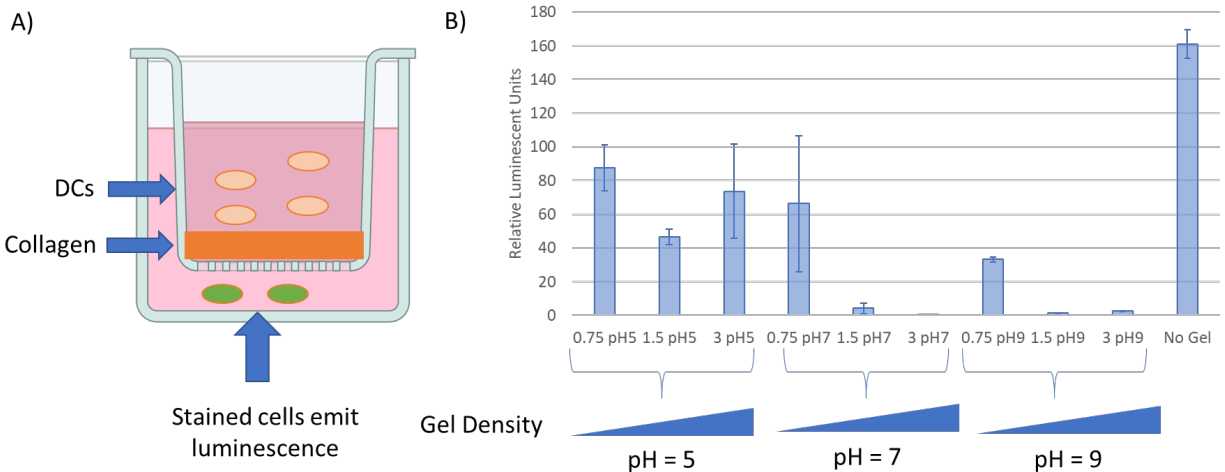


Figure 6. Collagen concentration and crosslinking pH affect the ability of dendritic cells (DCs) to cross the collagen barrier. A) An illustration of the trans-well assay with a collagen barrier at the bottom of the trans-well separating the DCs and a chemoattractant. The DCs that cross the barrier are stained to emit luminescence. B) The relative luminescence of the cells for each collagen formulation. The number of cells to cross the barrier generally increased as the collagen concentration decreased and as the pH was lowered. A no gel control was also tested to confirm that the DCs could travel through the mesh separating the two chambers of the trans-well.

Then the ability of certain collagen formulations to serve as a cell scaffold was tested. A successful epithelial cell scaffold allowed the Caco2 cells to adhere to the surface of the collagen and did not penetrate the barrier. Of the collagen formulations with a crosslinking pH of 5, the 1.5 mg ml⁻¹ and 3.0 mg ml⁻¹ were tested figure 7A and 7B. It was found that these formulations

were too porous and allowed the Caco2 cells, particles in the images, to cross the barrier after being seeded. The collagen formulation crosslinked at pH 7 and at 0.75 mg ml^{-1} was also too porous, figure 7C. Therefore, for future studies, collagen was crosslinked at pH 7 at a concentration of 1.5 mg ml^{-1} .

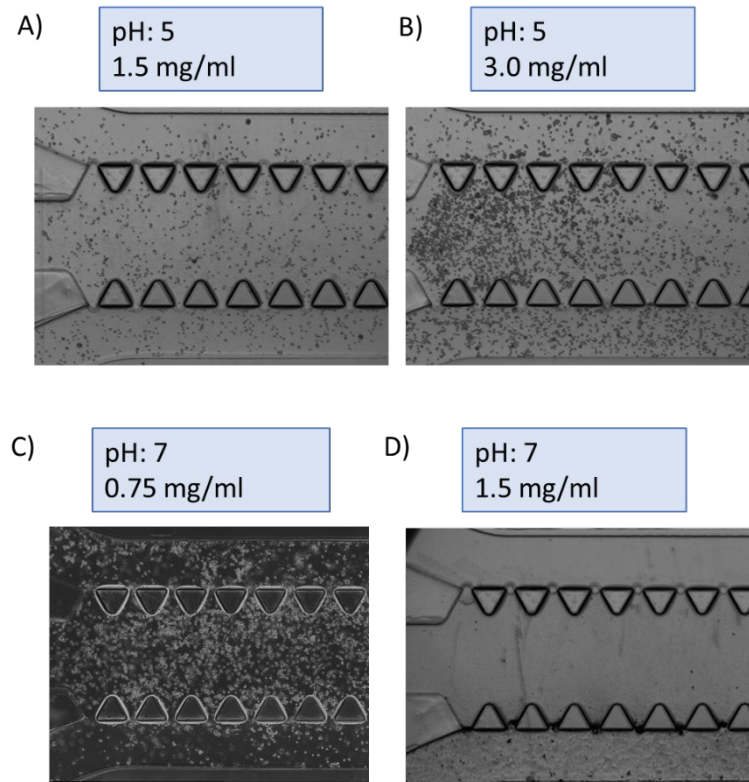


Figure 7. Most of the tested collagen formulations were too porous to serve as a scaffold for Caco2 cells, the cells are the particles in the images. A) At pH 5 and 1.5 mg ml^{-1} , cells were able to cross the barrier during seeding. B) At pH 5 and 3.0 mg ml^{-1} , cells were able to cross the barrier during seeding. C) At pH 7 and 0.75 mg ml^{-1} , cells were able to cross the barrier during seeding. D) At pH 7 and 1.5 mg ml^{-1} , cells were unable to cross the barrier during seeding.

Cell Barrier Formation

After the collagen formulation was optimized to serve as a cell barrier and scaffold, the ability of the Caco2 cells to form a functional barrier was tested in the idenTx chips. Caco2 cells were chosen for this work, because they form tight junctions as they are cultured which can be

used as an *in vitro* intestinal model [109-111]. Barrier formation was assessed with the same permeability assay described above. Barrier permeability was quantified using equation 1 to give P_{app} or apparent permeability.

$$P_{app}(cm/s) = \left(\frac{V_R}{AI_{D,0}} \right) \frac{\partial I}{\partial t} \quad (1)$$

V_R is the volume of the receiving chamber across the barrier from where the FITC-Dextran was added, A is the cross-sectional area of the barrier, $I_{D,0}$ is the initial dye intensity on the cell side, I is the dye intensity and t is time. P_{app} was measured every seven days after cell seeding, Figure 8. For each permeability experiment, the FITC intensity was measured across the lateral distance of the entire device for every time point measured, figure 8A. The rate of change for the dye intensity in the receiving chamber was used to calculate P_{app} . A higher value of P_{app} indicates a more permeable and less functional barrier. After 7 days, P_{app} increased slightly and appeared to remain constant after 15 days.

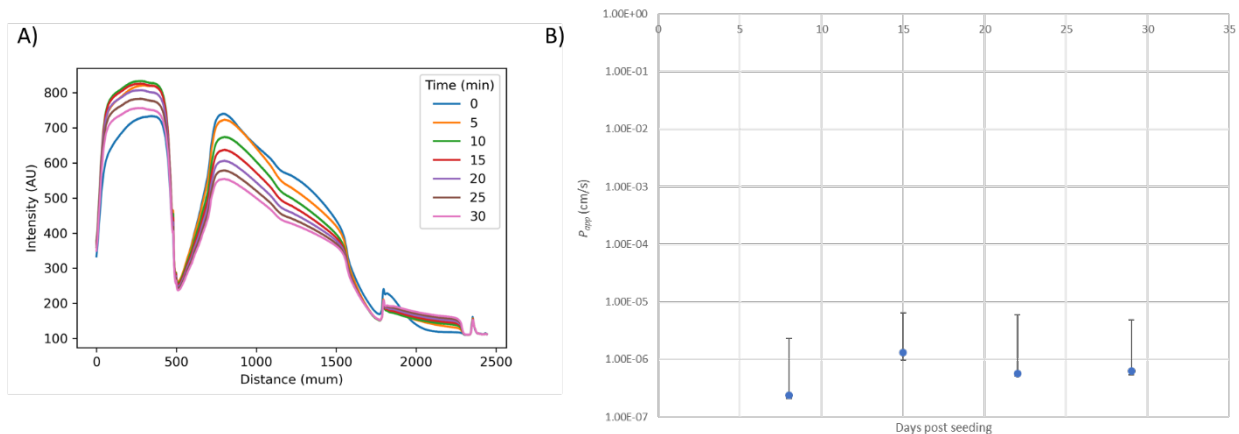


Figure 8. Caco2 barrier permeability increased after 7 days and appears to remain constant after 15 days. A) A represent plot of the permeability experiments used to calculate P_{app} . B) A plot of P_{app} over time after seeding Caco2 cells in the indent chips.

Future Directions

This μ GIS project has a lot of potential that unfortunately could not be fully explored over the course of this PhD. The most obvious first direction, was to determine the permeability of the Caco2 barrier at time points to find the optimal time that a functional barrier was formed. Another future direction would be trigger apoptosis or induce cellular stress on the Caco2 cells and determine the affects of that stress on the barrier permeability. This could be uniquely done with the idenTx chips because it is easily imaged with epi-fluorescent microscopy. Correlating cell stress to losses in permeability would elaborate on this systems ability to be a model intestinal barrier model. Another future study, would be study the response of DCs to Caco2 cells undergoing apoptosis to assess if the system would allow for DC recruitment across the collagen barrier. Instead of Caco2 cells, the idenTx chips could be seeded with cells derived from HIO spheroids, this was attempted by the author but culturing the organoids proved difficult. Finally, culturing all three types shown in figure 1 would prove to be a unique experiment system to explore the interplay between bacterial, epithelial, and immune cells.

REFERENCES CITED

1. Boeshaghi, A.S., et al., *Principles of open source bioinstrumentation applied to the poseidon syringe pump system*. Sci Rep, 2019. **9**(1): p. 12385.
2. Lake, J.R., K.C. Heyde, and W.C. Ruder, *Low-cost feedback-controlled syringe pressure pumps for microfluidics applications*. PLoS One, 2017. **12**(4): p. e0175089.
3. Zeng, W., et al., *Characterization of syringe-pump-driven induced pressure fluctuations in elastic microchannels*. Lab Chip, 2015. **15**(4): p. 1110-5.
4. Zeng, W., et al., *Variation in polydispersity in pump- and pressure-driven micro-droplet generators*. Journal of Micromechanics and Microengineering, 2015. **25**(11): p. 115015.
5. Sodergren, S., K. Svensson, and K. Hjort, *Microfluidic active pressure and flow stabiliser*. Sci Rep, 2021. **11**(1): p. 22504.
6. Kim, C., et al., *Water-head pumps provide precise and fast microfluidic pumping and switching versus syringe pumps*. Microfluidics and Nanofluidics, 2016. **20**(1): p. 1 - 8.
7. Komeya, M., et al., *Pumpless microfluidic system driven by hydrostatic pressure induces and maintains mouse spermatogenesis in vitro*. Sci Rep, 2017. **7**(1): p. 15459.
8. Wang, X., et al., *A hydrostatic pressure-driven passive micropump enhanced with siphon-based autofill function*. Lab Chip, 2018. **18**(15): p. 2167-2177.
9. Frank, P., et al., *Fully-Programmable, Low-Cost, "Do-It-Yourself" Pressure Source for General Purpose Use in the Microfluidic Laboratory*. Inventions, 2016. **1**(2).
10. Watson, C. and S.E. Senyo, *All-in-one automated microfluidics control system*. HardwareX, 2019. **5**: p. e00063.
11. Gao, R.Z., et al., *μ Pump: An open-source pressure pump for precision fluid handling in microfluidics*. HardwareX, 2020. **7**: p. e00096.
12. Holtze, C., et al., *Biocompatible surfactants for water-in-fluorocarbon emulsions*. Lab Chip, 2008. **8**(10): p. 1632-9.

13. Wagner, O., et al., *Biocompatible fluorinated polyglycerols for droplet microfluidics as an alternative to PEG-based copolymer surfactants*. *Lab Chip*, 2016. **16**(1): p. 65-9.
14. Stucki, A., et al., *Droplet Microfluidics and Directed Evolution of Enzymes: An Intertwined Journey*. *Angewandte Chemie (International ed. in English)*, 2021. **60**(46): p. 24368-24387.
15. Jing, W. and H.S. Han, *Droplet Microfluidics for High-Resolution Virology*. *Anal Chem*, 2022. **94**(23): p. 8085-8100.
16. Kaminski, T.S. and P. Garstecki, *Controlled droplet microfluidic systems for multistep chemical and biological assays*. *Chem Soc Rev*, 2017. **46**(20): p. 6210-6226.
17. Kaminski, T.S., O. Scheler, and P. Garstecki, *Droplet microfluidics for microbiology: techniques, applications and challenges*. *Lab Chip*, 2016. **16**(12): p. 2168-87.
18. Clausell-Tormos, J., et al., *Droplet-based microfluidic platforms for the encapsulation and screening of Mammalian cells and multicellular organisms*. *Chem Biol*, 2008. **15**(5): p. 427-37.
19. Thorsen, T., et al., *Dynamic pattern formation in a vesicle-generating microfluidic device*. *Phys Rev Lett*, 2001. **86**(18): p. 4163-6.
20. Garstecki, P., et al., *Formation of droplets and bubbles in a microfluidic T-junction-scaling and mechanism of break-up*. *Lab Chip*, 2006. **6**(3): p. 437-46.
21. Anna, S.L., *Droplets and Bubbles in Microfluidic Devices*. *Annual Review of Fluid Mechanics*, 2016. **48**(1): p. 285-309.
22. Abate, A.R., et al., *Impact of inlet channel geometry on microfluidic drop formation*. *Phys Rev E Stat Nonlin Soft Matter Phys*, 2009. **80**(2 Pt 2): p. 026310.
23. Anna, S.L., N. Bontoux, and H.A. Stone, *Formation of dispersions using "flow focusing" in microchannels*. *Applied Physics Letters*, 2003. **82**(3): p. 364-366.

24. Romero, P.A. and A.R. Abate, *Flow focusing geometry generates droplets through a plug and squeeze mechanism*. Lab Chip, 2012. **12**(24): p. 5130-2.
25. Loveday, E.K., et al., *Single-Cell Infection of Influenza A Virus Using Drop-Based Microfluidics*. Microbiology spectrum, 2022. **10**(5): p. e0099322-e0099322.
26. Lee, W., L.M. Walker, and S.L. Anna, *Role of geometry and fluid properties in droplet and thread formation processes in planar flow focusing*. Physics of Fluids, 2009. **21**(3).
27. Baroud, C.N., F. Gallaire, and R.J.L.o.a.C. Dangla, *Dynamics of microfluidic droplets*. 2010. **10**(16): p. 2032-2045.
28. Lashkaripour, A., et al., *Machine learning enables design automation of microfluidic flow-focusing droplet generation*. Nat Commun, 2021. **12**(1): p. 25.
29. A.S. Utada, L.-Y.C., A. Fernandez-Nieves, D.R. Link, C. Holtze, and D.A. Weitz, *Dripping, Jetting, Drops, and Wetting: The Magic of Microfluidics*. MRS Bulletin, 2007. **32**: p. 702-708.
30. Utada, A.S., et al., *Dripping to Jetting Transitions in Coflowing Liquid Streams*. Physical Review Letters, 2007. **99**(9): p. 094502.
31. Fuerstman, M.J., P. Garstecki, and G.M. Whitesides, *Coding/Decoding and Reversibility of Droplet Trains in Microfluidic Networks*. Science, 2007. **315**(5813): p. 828-832.
32. Sessoms, D.A., et al., *Droplet motion in microfluidic networks: Hydrodynamic interactions and pressure-drop measurements*. Phys Rev E Stat Nonlin Soft Matter Phys, 2009. **80**(1 Pt 2): p. 016317.
33. Prakash, M. and N. Gershenfeld, *Microfluidic Bubble Logic*. Science, 2007. **315**(5813): p. 832-835.
34. Ahn, B., et al., *Parallel synchronization of two trains of droplets using a railroad-like channel network*. Lab Chip, 2011. **11**(23): p. 3956-62.

35. Cristobal, G., et al., *Microfluidic bypass for efficient passive regulation of droplet traffic at a junction*. Applied Physics Letters, 2006. **89**(3).
36. Jousse, F., et al., *Compact model for multi-phase liquid-liquid flows in micro-fluidic devices*. Lab Chip, 2005. **5**(6): p. 646-56.
37. Schindler, M. and A. Ajdari, *Droplet traffic in microfluidic networks: a simple model for understanding and designing*. Phys Rev Lett, 2008. **100**(4): p. 044501.
38. Oh, K.W., et al., *Design of pressure-driven microfluidic networks using electric circuit analogy*. Lab Chip, 2012. **12**(3): p. 515-45.
39. Musterd, M., et al., *Calculating the volume of elongated bubbles and droplets in microchannels from a top view image*. RSC Advances, 2015. **5**(21): p. 16042-16049.
40. Fuerstman, M.J., et al., *The pressure drop along rectangular microchannels containing bubbles*. Lab Chip, 2007. **7**(11): p. 1479-89.
41. Abate, A.R. and D.A. Weitz, *Faster multiple emulsification with drop splitting*. Lab Chip, 2011. **11**(11): p. 1911-5.
42. Mary, P., et al., *On-chip background noise reduction for cell-based assays in droplets*. Lab Chip, 2011. **11**(12): p. 2066-70.
43. Eastburn, D.J., A. Sciambi, and A.R. Abate, *Ultrahigh-throughput Mammalian single-cell reverse-transcriptase polymerase chain reaction in microfluidic drops*. Anal Chem, 2013. **85**(16): p. 8016-21.
44. Tao, Y., et al., *Rapid, targeted and culture-free viral infectivity assay in drop-based microfluidics*. Lab Chip, 2015. **15**(19): p. 3934-40.
45. Link, D.R., et al., *Geometrically mediated breakup of drops in microfluidic devices*. Phys Rev Lett, 2004. **92**(5): p. 054503.
46. Samie, M., A. Salari, and M.B. Shafii, *Breakup of microdroplets in asymmetric T junctions*. Phys Rev E Stat Nonlin Soft Matter Phys, 2013. **87**(5): p. 053003.

47. Jullien, M.C., et al., *Droplet breakup in microfluidic T-junctions at small capillary numbers*. *Physics of Fluids*, 2009. **21**(7).
48. Leshansky, A.M., et al., *Obstructed breakup of slender drops in a microfluidic T junction*. *Phys Rev Lett*, 2012. **108**(26): p. 264502.
49. Menetrier-Deremble, L. and P. Tabeling, *Droplet breakup in microfluidic junctions of arbitrary angles*. *Phys Rev E Stat Nonlin Soft Matter Phys*, 2006. **74**(3 Pt 2): p. 035303.
50. Agnihotri, S.N., et al., *Droplet Breakup at the Entrance to a Bypass Channel in a Microfluidic System*. *Physical Review Applied*, 2019. **11**(3).
51. El Debs, B., et al., *Functional single-cell hybridoma screening using droplet-based microfluidics*. *Proc Natl Acad Sci U S A*, 2012. **109**(29): p. 11570-5.
52. Rotem, A., et al., *Evolution on the Biophysical Fitness Landscape of an RNA Virus*. *Mol Biol Evol*, 2018. **35**(10): p. 2390-2400.
53. Herminghaus, S., *Dynamical Instability of Thin Liquid Films Between Conducting Media*. *Physical Review Letters*, 1999. **83**(12): p. 2359-2361.
54. Priest, C., S. Herminghaus, and R. Seemann, *Controlled electrocoalescence in microfluidics: Targeting a single lamella*. *Applied Physics Letters*, 2006. **89**(13): p. 134101.
55. Ahn, K., et al., *Electrocoalescence of drops synchronized by size-dependent flow in microfluidic channels*. *Applied Physics Letters*, 2006. **88**(26).
56. Sciambi, A. and A.R. Abate, *Generating electric fields in PDMS microfluidic devices with salt water electrodes*. *Lab Chip*, 2014. **14**(15): p. 2605-9.
57. Mazutis, L., et al., *Droplet-Based Microfluidic Systems for High-Throughput Single DNA Molecule Isothermal Amplification and Analysis*. *Analytical Chemistry*, 2009. **81**(12): p. 4813-4821.

58. Abate, A.R., et al., *High-throughput injection with microfluidics using picoinjectors*. Proc Natl Acad Sci U S A, 2010. **107**(45): p. 19163-6.
59. Xu, L., et al., *Fusion and sorting of two parallel trains of droplets using a railroad-like channel network and guiding tracks*. Lab Chip, 2012. **12**(20): p. 3936-42.
60. Abbyad, P., et al., *Rails and anchors: guiding and trapping droplet microreactors in two dimensions*. Lab Chip, 2011. **11**(5): p. 813-21.
61. Volpatti, L.R. and A.K. Yetisen, *Commercialization of microfluidic devices*. Trends Biotechnol, 2014. **32**(7): p. 347-50.
62. Scheler, O., W. Postek, and P. Garstecki, *Recent developments of microfluidics as a tool for biotechnology and microbiology*. Curr Opin Biotechnol, 2019. **55**: p. 60-67.
63. Lee, M., et al., *Synchronized reinjection and coalescence of droplets in microfluidics*. Lab Chip, 2014. **14**(3): p. 509-13.
64. Moon, B.U., et al., *Water-in-Water Droplets by Passive Microfluidic Flow Focusing*. Anal Chem, 2016. **88**(7): p. 3982-9.
65. Mavrogiannis, N., et al., *Microfluidics made easy: A robust low-cost constant pressure flow controller for engineers and cell biologists*. Biomicrofluidics, 2016. **10**(3): p. 034107.
66. Zath, G.K., et al., *Rapid parallel generation of a fluorescently barcoded drop library from a microtiter plate using the plate-interfacing parallel encapsulation (PIPE) chip*. Lab Chip, 2022. **22**(23): p. 4735-4745.
67. Van Rossum, G., *The Python Library Reference, release 3.8.2*. 2020: Python Software Foundation.
68. Horowitz, P. and W. Hill, *The Art of Electronics*. 1980: Cambridge University Press.
69. Seaborg, D.E., et al., *Process Dynamics and Control*. 2014: John Wiley & Sons, Inc.

70. Johnston, K.P., et al., *Water-in-Carbon Dioxide Microemulsions: An Environment for Hydrophiles Including Proteins*. Science, 1996. **271**(5249): p. 624-626.
71. Duffy, D.C., et al., *Rapid Prototyping of Microfluidic Systems in Poly(dimethylsiloxane)*. Analytical Chemistry, 1998. **70**(23): p. 4974-4984.
72. Ward, T., et al., *Microfluidic flow focusing: drop size and scaling in pressure versus flow-rate-driven pumping*. Electrophoresis, 2005. **26**(19): p. 3716-24.
73. Basu, A.S., *Droplet morphometry and velocimetry (DMV): a video processing software for time-resolved, label-free tracking of droplet parameters*. Lab Chip, 2013. **13**(10): p. 1892-901.
74. Ronaldson-Bouchard, K. and G. Vunjak-Novakovic, *Organs-on-a-Chip: A Fast Track for Engineered Human Tissues in Drug Development*. Cell Stem Cell, 2018. **22**(3): p. 310-324.
75. Pimenta, J., et al., *Organ-on-Chip Approaches for Intestinal 3D In Vitro Modeling*. Cell Mol Gastroenterol Hepatol, 2022. **13**(2): p. 351-367.
76. Low, L.A., et al., *Organs-on-chips: into the next decade*. Nat Rev Drug Discov, 2020.
77. Tao, Y., et al., *Artifact-Free Quantification and Sequencing of Rare Recombinant Viruses by Using Drop-Based Microfluidics*. Chembiochem, 2015. **16**(15): p. 2167-71.
78. Zhang, H., et al., *Isolation and Analysis of Rare Norovirus Recombinants from Coinfected Mice Using Drop-Based Microfluidics*. J Virol, 2015. **89**(15): p. 7722-34.
79. Guo, M.T., et al., *Droplet microfluidics for high-throughput biological assays*. Lab Chip, 2012. **12**(12): p. 2146-55.
80. Mazutis, L., et al., *Multi-step microfluidic droplet processing: kinetic analysis of an in vitro translated enzyme*. Lab Chip, 2009. **9**(20): p. 2902-8.
81. Brouzes, E., et al., *Droplet microfluidic technology for single-cell high-throughput screening*. PNAS, 2009. **106**(34): p. 14195-14200.

82. Kim, H.S., et al., *A droplet microfluidics platform for rapid microalgal growth and oil production analysis*. *Biotechnol Bioeng*, 2016. **113**(8): p. 1691-701.
83. Holland-Moritz, D.A., et al., *Mass Activated Droplet Sorting (MADS) Enables High-Throughput Screening of Enzymatic Reactions at Nanoliter Scale*. *Angew Chem Int Ed Engl*, 2020. **59**(11): p. 4470-4477.
84. Cornish, R.J. and E.A. Milne, *Flow in a pipe of rectangular cross-section*. *Proceedings of the Royal Society of London. Series A, Containing Papers of a Mathematical and Physical Character*, 1928. **120**(786): p. 691-700.
85. Mortensen, N.A., F. Okkels, and H. Bruus, *Reexamination of Hagen-Poiseuille flow: shape dependence of the hydraulic resistance in microchannels*. *Phys Rev E Stat Nonlin Soft Matter Phys*, 2005. **71**(5 Pt 2): p. 057301.
86. Christopher, G.F., et al., *Experimental observations of the squeezing-to-dripping transition in T-shaped microfluidic junctions*. *Phys Rev E Stat Nonlin Soft Matter Phys*, 2008. **78**(3 Pt 2): p. 036317.
87. Ma, C., et al., *Organ-on-a-Chip: A New Paradigm for Drug Development*. *Trends Pharmacol Sci*, 2021. **42**(2): p. 119-133.
88. Tang, H., et al., *Human Organs-on-Chips for Virology*. *Trends Microbiol*, 2020. **28**(11): p. 934-946.
89. Sidar, B., et al., *Long-term flow through human intestinal organoids with the gut organoid flow chip (GOFlowChip)*. *Lab Chip*, 2019. **19**(20): p. 3552-3562.
90. Rossi, G., A. Manfrin, and M.P. Lutolf, *Progress and potential in organoid research*. *Nat Rev Genet*, 2018. **19**(11): p. 671-687.
91. McCracken, K.W., et al., *Generating human intestinal tissue from pluripotent stem cells in vitro*. *Nat Protoc*, 2011. **6**(12): p. 1920-8.
92. Spence, J.R., et al., *Directed differentiation of human pluripotent stem cells into intestinal tissue in vitro*. *Nature*, 2011. **470**(7332): p. 105-9.

93. Sebrell, T.A., et al., *A Novel Gastric Spheroid Co-culture Model Reveals Chemokine-Dependent Recruitment of Human Dendritic Cells to the Gastric Epithelium*. *Cell Mol Gastroenterol Hepatol*, 2019. **8**(1): p. 157-171 e3.
94. Bekiaris, V., E.K. Persson, and W.W. Agace, *Intestinal dendritic cells in the regulation of mucosal immunity*. *Immunological Reviews*, 2014. **260**(1): p. 86-101.
95. Cherne, M.D., et al., *A Synthetic Hydrogel, VitroGel((R)) ORGANOID-3, Improves Immune Cell-Epithelial Interactions in a Tissue Chip Co-Culture Model of Human Gastric Organoids and Dendritic Cells*. *Front Pharmacol*, 2021. **12**: p. 707891.
96. Mahdieh, Z., et al., *Granular Matrigel: restructuring a trusted extracellular matrix material for improved permeability*. *Biomed Mater*, 2022. **17**(4).
97. Ismagilov, R.F., et al., *Experimental and theoretical scaling laws for transverse diffusive broadening in two-phase laminar flows in microchannels*. *Applied Physics Letters*, 2000. **76**(17): p. 2376-2378.
98. Loessberg-Zahl, J., et al., *Patterning Biological Gels for 3D Cell Culture inside Microfluidic Devices by Local Surface Modification through Laminar Flow Patterning*. *Micromachines (Basel)*, 2020. **11**(12).
99. Leon-Lopez, A., et al., *Hydrolyzed Collagen-Sources and Applications*. *Molecules*, 2019. **24**(22).
100. Vickerman, V., et al., *Design, fabrication and implementation of a novel multi-parameter control microfluidic platform for three-dimensional cell culture and real-time imaging*. *Lab Chip*, 2008. **8**(9): p. 1468-77.
101. Campisi, M., et al., *3D self-organized microvascular model of the human blood-brain barrier with endothelial cells, pericytes and astrocytes*. *Biomaterials*, 2018. **180**: p. 117-129.
102. Zervantonakis, I.K., et al., *Three-dimensional microfluidic model for tumor cell intravasation and endothelial barrier function*. *Proc Natl Acad Sci U S A*, 2012. **109**(34): p. 13515-20.

103. Ramanujan, S., et al., *Diffusion and convection in collagen gels: implications for transport in the tumor interstitium*. Biophys J, 2002. **83**(3): p. 1650-60.
104. Sapudom, J. and T. Pompe, *Biomimetic tumor microenvironments based on collagen matrices*. Biomater Sci, 2018. **6**(8): p. 2009-2024.
105. Cross, V.L., et al., *Dense type I collagen matrices that support cellular remodeling and microfabrication for studies of tumor angiogenesis and vasculogenesis in vitro*. Biomaterials, 2010. **31**(33): p. 8596-607.
106. Raub, C.B., et al., *Image correlation spectroscopy of multiphoton images correlates with collagen mechanical properties*. Biophys J, 2008. **94**(6): p. 2361-73.
107. Miron-Mendoza, M., J. Seemann, and F. Grinnell, *The differential regulation of cell motile activity through matrix stiffness and porosity in three dimensional collagen matrices*. Biomaterials, 2010. **31**(25): p. 6425-35.
108. Han, S., et al., *A versatile assay for monitoring in vivo-like transendothelial migration of neutrophils*. Lab Chip, 2012. **12**(20): p. 3861-5.
109. Natoli, M., et al., *Good Caco-2 cell culture practices*. Toxicol In Vitro, 2012. **26**(8): p. 1243-6.
110. Ma'ayeh, S.Y., et al., *Responses of the Differentiated Intestinal Epithelial Cell Line Caco-2 to Infection With the Giardia intestinalis GS Isolate*. Front Cell Infect Microbiol, 2018. **8**: p. 244.
111. Darling, N.J., et al., *Bioengineering Novel in vitro Co-culture Models That Represent the Human Intestinal Mucosa With Improved Caco-2 Structure and Barrier Function*. Front Bioeng Biotechnol, 2020. **8**: p. 992.